

HIGH-RESOLUTION INTERFEROMETRIC STUDY OF CIRCUMNUCLEAR GAS IN RADIO-ACTIVE GALAXIES

YOSHIAKI HAGIWARA

Dept. of Astronomical Science
The Graduate University for Advanced Studies
Mitaka, Tokyo

In Partial Fulfillment of the Requirements
for the Degree of
Doctor of Science

1998
(Submitted 1999 January 8)

Abstract

In this thesis, I will present the development of the Rainbow Array system. Then, I will describe detailed kinematical studies in circumnuclear regions of radio-active galaxy, NGC 1275 with the Rainbow Array. I also present the parsec-scale observations of NGC 5793 with VLBA.

Prior to the Rainbow Array observations, I had been devoted to the construction of the extended NMA (Rainbow Array) system. The Rainbow Array consists of the six 10 m telescopes and the 45 m telescope. The use of the 45 m telescope with NMA would result in great improvement in the sensitivity and spatial resolution. In order to realize the Rainbow Array project, I have contributed to construction and installation of the 3 mm and 2 mm SIS receiver system and design of their optics for the 45 m telescope. After accomplishment of Rainbow system design, I conducted the verification of the whole array system. In order to verify the Rainbow front-end system, both single-dish and interferometric test observations were carried out. The Rainbow Array system was confirmed to work almost nearly as I estimated in advance. Finally, I carried out mapping observations for both continuum and spectral line emission (CO ($J = 1 \rightarrow 0$)) with the Rainbow Array.

The CO ($J = 1 \rightarrow 0$) line observations of NGC 1275 were, then, carried out at an angular resolution of \sim one arcsecond with the Rainbow Array. The method of observations made use of self-calibration technique in order to minimize baseline calibration errors which mainly arise from uncertainties of 45 m – 10 m baselines.

The CO line emission of NGC 1275 was found to concentrate in the central $r = 400$ pc region from the nucleus. The total molecular mass estimated from the line intensity is $\sim 10^9 M_{\odot}$. This value is only 4.5% of the molecular mass estimated from the previous observations at the central 10 kpc region. Although there are some discrepancies in the obtained results with those in published images, the follow-up NMA observations confirmed that the image obtained with the Rainbow is reliable.

The CO *twin peaks* structure with a radius of 1.2 kpc from the nucleus reported by Inoue *et al.* (1996) and the newly detected CO central concentration seem to imply that the detected central CO emission could be the results of gas fueling from the outer molecular gas ring structure, by analogy with a case of the Seyfert galaxy, NGC 1068. The central unresolved CO peak emission could form the molecular torus which obscures the central engine from our direct view. It is very interesting that the circumnuclear gas surrounding the radio-loud nucleus has a very similar morphology with that around the radio-quiet nuclei. In conclusion, I suggest that the radio activity in the radio galaxy is *not* determined from the properties of circumnuclear gas, but it might be related to the nature of the central engine.

The studies of NGC 5793 began with the detection of water maser emission toward the center using the 45 m telescope. The maser emission symmetrically offset from the systemic velocity could be inferred to arise in a rotating molecular disk by analogy with NGC 4258. VLBA observations were, then, conducted to search for the parsec-scale maser disk. The maser spots were found to be offset from the continuum

peak by ~ 3 pc with an alignment between position angles of nuclear continuum jet. It is likely that maser emission could originate in a molecular cloud foreground to the jet, and be amplifying the radio jet in the background. In addition to maser studies, our VLBA L-band observations to search for the OH absorption revealed that there exists compact OH gas distribution on about 5 pc from the radio nucleus, showing the velocity gradient along the axis of the galactic disk on larger scale. The sense of the OH velocity gradient differs from that of the kiloparsec-scale CO disk which is detected by the NMA. This suggests that the compact and parsec scale OH absorbing gas might trace the circumnuclear molecular gas kinematically independent from the galactic disk.

Thus, a series of parsec-scale mappings in NGC 5793 revealed a variety of molecular gas distribution in the circumnuclear region of AGN.

Contents

1	INTRODUCTION	2
	Introduction to AGN	2
	A Brief Historical Review of AGN Family	3
	Unification of AGN; Basic Concept of Unification Models	4
	Search for Circumnuclear Disk/Torus	5
	Energy Transport Mechanism in the Circumnuclear Region of AGN	5
	Kinematics of Molecular Torus/Disk	6
	VLBI and the Water Maser Disk	6
	Absorption Line	7
	The Rainbow Array	7
	What is the Rainbow Array ?	7
	Scientific Capabilities of the Rainbow Array	9
	Motivation of this Thesis	10
	Search for Circumnuclear Molecular Gas with the Rainbow Array	10
	Rainbow Array Observations of Radio-loud AGN, NGC 1275	10
	VLBA Observations of Radio-active Galaxy, NGC 5793	11
	Structure of this Thesis	12
2	INSTRUMENTATION — 45 M TELESCOPE RECEIVING SYSTEM	14
	Rainbow Array	14
	Overview	14
	A Brief Historical Review	14
	The Rainbow System Design	15

Overview	15
SIS Receiver System	15
Beam Waveguide (Optics) Design	16
Rainbow Observing System	17
Array Performance (Expected)	17
Measurements for the Rainbow Array System	20
Receiver Noise, System Temperature, and Beam Pattern	20
Test Observations	21
Summary	22
3 NUCLEAR MOLECULAR GAS IN NGC1275 – CO OBSERVATION WITH THE RAINBOW ARRAY	30
Introduction	30
Observations and Data Analysis	32
Observations	32
Data Reduction for the Rainbow	36
Data Reduction for the NMA-D	37
Results	37
The Rainbow	37
NMA-D	39
Discussion	40
Compact CO Emission at the Nucleus: Comparison with Inoue et al.	40
H ₂ Emission at the Nucleus	41
Interpretation of the central CO peak	42
Origin of Molecular Gas	42
Comparison with NGC 1068	43
Summary	44
4 WATER-VAPOUR MEGAMASER IN RADIO-ACTIVE GALAXY NGC 5793	56
The Host Galaxy	56
Summary of Observations	56
Detection of a Water-Vapor Megamaser	57

Introduction	57
NRO 45 m Observations	57
Results of 45-m OBSERVATIONS	58
Discussion	58
CO (1–0) Distribution in NGC 5793	59
NMA Results	59
High-Resolution Study of Water-Vapor Maser	66
VLA Observations	66
VLBA Observations	66
5 HIGH-RESOLUTION OH ABSORPTION STUDY OF NGC 5793	71
Introduction	71
Observations	72
Results	73
Continuum	73
The OH Absorptions	75
Discussions	75
The Continuum Structures	75
Properties of the OH Absorption	81
Distributions and Kinematics of Molecular Gas	82
Relation to H ₂ O Maser Emission and HI Absorption	83
Summary	83
6 SUMMARY	85
ACKNOWLEDGEMENTS	87
BIBLIOGRAPHY	88
Appendix. Parameters in the Optics	94
Parameters at 3 mm	94
Parameters at 2 mm	98
Parameters at 1.3 mm	101
Parameters at 1.3 mm (half illumination mode)	104

Chapter 1

INTRODUCTION

Introduction to AGN

Active Galactic Nuclei (AGN) represent the energetic phenomenon observed in the central region of galaxies. The energy released from AGNs exhibit huge luminosity, more than 10^{43} erg s⁻¹, in central regions, although the basic mechanism of such a huge energy production has not yet been identified in detail. In addition to it, the mechanism sustaining its energy over its life time of at least 10^8 years has been also problematic. Models for energy transport mechanism via gravitational accretion into the central engine are widely supported, however description of these models are very ambiguous in order to understand physical process occurring in the nucleus of AGN (Gunn 1979). There is a widely accepted consensus based on observational facts that the energetic properties of AGN are related to its environment (e.g., Toomre and Toomre 1972). Another major problem is that the collimation mechanism of jets that are commonly observed in central regions.

There is another important area of study in relating to the AGN: A scenario linking the existence of AGN to starburst occurring in the merging galaxy system. In this model, the energy source fueling the central engine is supposed to be starburst activity that is induced by galaxy-to-galaxy interaction or merging (e.g., Sanders *et al.* 1988, Norman and Scoville 1988).

Despite these unsolved problems, our understanding of AGN has dramatically advanced in the last two decades. This is mainly due to the development of new observing techniques that improved sensitivity and resolution of both the ground-based and space-borne telescopes. In particular, the technical progress in radio interferometer with high angular resolution has been greatly contributing to the imaging study of AGN.

The typical model (what we call “Unification model”) of an AGN nucleus and circumnuclear region surrounding it is shown in Figure 1. It is generally believed that the ‘central engine’, an ultimate energy source of AGN, consists of a super massive black hole and an accretion disk surrounding it. Material that is gravitationally infalling towards the black hole is heated to high temperature by friction or radiation (ultra-violet(UV) to X-ray) in the accretion disk. This heated material is ionised in the dense gas clouds to form the ‘Broad Line Region’ (BLR), producing the highly ionised emission lines. Outside this innermost emission line region, the ‘Narrow Line Region’ (NLR) lies at 10 – 100 pc from the nucleus. Further out these emission line regions, narrow line emission extending up to 20 kpc from the nucleus are observed in 1980s. This physically distinct region from NLR are named as the ‘Extended Narrow Line Region’ (ENLR). The BLR and NLR are briefly described in later sections. Relativistic plasma outflows emanating through the dense gas region are often seen up to several kpc scales from the nucleus particularly when the host

galaxy is elliptical.

These observational properties of AGN seem to depend so strongly on the orientation of dense material (e.g., Antonucci 1993), so that we have intensely researched especially in radio-quiet spirals. This thesis makes use of high-angular resolution observations to study the molecular disk/torus in radio-loud AGN in order to investigate its circumnuclear region.

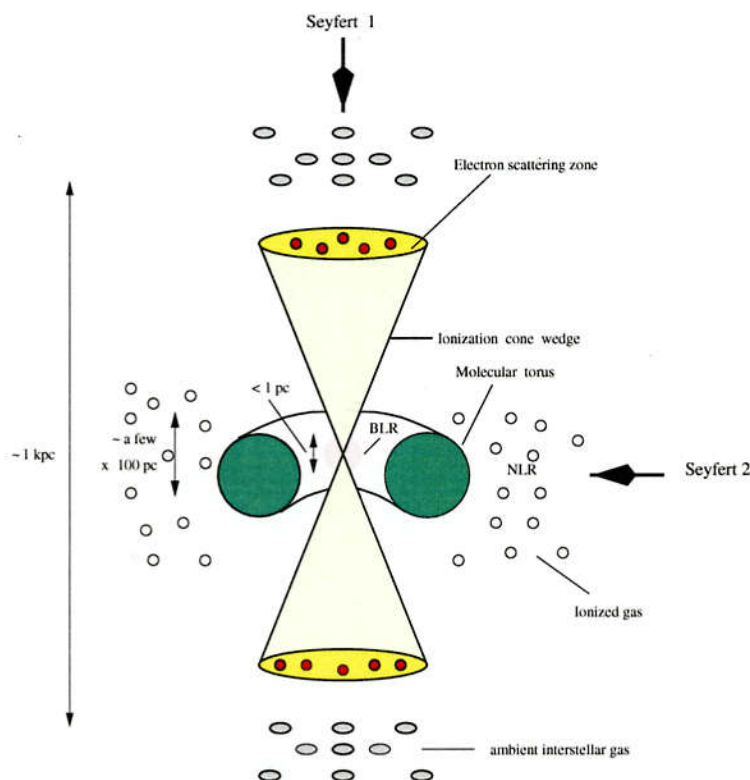


Fig. 1.— A schematic model of a Seyfert Nucleus and its nuclear region

A Brief Historical Review of AGN Family

When we talk about the beginning of AGN research, we have to date back to 1909, when the first optical spectrum of an active galaxy was obtained by E.A. Fath (1911) in NGC 1068, although he was not aware of this spectrum to arise from an extragalactic object. Carl Seyfert optically identified six galaxies (NGC 1068, NGC 1275, NGC 3516, NGC 4051, NGC 4151 and NGC 7469) in 1943, which showed broad emission lines towards the extremely bright and starlike nuclei (Seyfert 1943). This is the first discovery of a class of Seyferts. (Except for NGC 1275 they all are spiral galaxies, however NGC 1275 exhibit the same emission line properties as like others.) These characteristics have become to the basis of the classification for Seyfert galaxies, which can be found 2 ~ 3 % of field spiral galaxies.

With improvement of spectroscopic techniques in early 1970s, the picture of Seyfert galaxies became more complicated. In 1974, Khachikian and Weedman subdivided Seyferts into two categories, Seyfert 1s and Seyfert 2s. Seyfert 1s have broad permitted lines originating with equivalent velocity widths of as high as $10,000 \text{ km s}^{-1}$ and narrow forbidden lines. On the other hand, Seyfert 2s are characterised by narrow

forbidden and broad permitted lines with velocity widths ranging up to $1,000 \text{ km s}^{-1}$.

The radio surveys with high angular resolution began in 1950s and some strong radio sources were identified with optical counterparts. Those were often galaxies but sometimes stellar objects. The first strong radio source identified was 3C 48, a star-like optical source, although it was not recognized as an active galaxy. Another strong radio source was 3C 273 found at the uncommonly large redshift of 0.158. The luminosity of these objects are 100 times as large as that of Seyferts. These objects are termed as 'quasi-stellar radio source', what we call, 'quasar' in nowadays. The hosting galaxies of these extremely luminous AGN at high redshift could not be identified. There was substantial population of quasar-like objects which were optically selected, showing radio-quiet properties. These were termed as 'quasi-stellar objects', or QSOs. While the term of 'quasar' are referred to the radio-loud quasar (RLQ), the term of 'QSO' are used for radio-quiet quasar (RQQ). While Seyfert galaxies have radio-quiet property, some of the powerful radio-loud galaxies were found in 1950s having the similar emission line spectra to the Seyfert nuclei. Those are, what we call now, radio galaxies. They are discriminated from quasars in that they often show extended radio structures with the luminous compact cores in their centers. According to the morphology of the extended radio structure and radio luminosity, they can be subdivided into two classes; Fanaroff-Riley type I (FR I) and type II (Fanaroff and Riley 1974).

In the 1970s, the radio-loud quasars with strong variable continuum emission and flat spectrum had been identified; they are 'Optically Violently Variable quasars' or OVV's and 'BL Lac' objects and they were grouped into a single category under the name of 'Blazars'. They have common properties in that they are extremely variable in optical for OVV's and radio for BL Lacs and show high degree of polarisation and lack emission lines. It is generally assumed that the strong variability is due to the relativistic jet pointing to our line of sight, resulting the rapid variability and superluminal movement to the line of sight.

Unification of AGN; Basic Concept of Unification Models

There is no doubt that several different types of AGN exist in AGN family and those were attempted to be categorised according to their apparent luminosities or spectral properties to minimize the diversity of the class. Most of unification models were suggested under an assumption that there is not so much intrinsic differences in subgroups of AGN family and observational diversity of their classes depend on the orientation effect (e.g. Urry *et al.* 1991, Antonucci 1993, Urry *et al.* 1995); whether or not viewing angle lies within an ionization cone. The widely accepted model for a Seyfert nucleus, one of the commonest type of AGN, is shown in Fig. 5. As shown in Fig. 5, when our line of sight is aligned within the opening angle of the ionization cone, we can foresee the NLR, BLR and continuum emission region through the disk/torus surrounding an active nucleus. In such a case the objects are termed as Type 1 AGN, in case of radio-quiet spirals or radio galaxies we call them a Type 1 Seyfert or a Broad Line Radio Galaxies (BLRG), etc. When the optically thick disk/torus lies in our line of sight, inside disk/torus - BLR and continuum region- are obscured. This is a Type 2 AGN, including a Type 2 Seyfert, a Low Ionization Nuclear Line Emission(LINER), a Narrow Line Radio Galaxy (NLRG), etc. Type 2 objects are those which lack the spectra from BLR in direct view, and only NRL spectra are seen. Another evidence for classification among AGN is radio-luminosity of the central source. The radio-loud objects are distinguished from the radio-quiet by the radio power at 21 cm, $P_{21\text{cm}} = 10^{23.3} \text{ W Hz}^{-1}$. Table 1 lists the basic unification models based on the radio properties and optical line spectra.

Search for Circumnuclear Disk/Torus

Energy Transport Mechanism in the Circumnuclear Region of AGN

As described in previous sections, it is believed in general that the anisotropic structure in AGN around the active nucleus which harbours the central engine produces the variety of 'apparent' classes of the AGN family. What determines this 'apparent' phenomenon is thought to be a thick disk or torus surrounding the BLR and collimating the nuclear continuum radiation. The scale of the obscuring disk/torus is roughly considered to be large enough to obscure the BLR and small enough not to prevent our direct view of the NLR, that is, a few ~ 300 pc. The obscuring interstellar material, molecular torus/disk, in the circumnuclear region of AGN plays another important role in the fuelling of central activity, but the actual mechanisms involved are unclear; the study of molecular gas distribution and dynamics would appear to be a good method to address this matter.

On scales up to 1 kpc, the most recent millimeter-wave interferometric observations revealed the existence of a bar-like structure surrounded by the molecular ring in Seyfert galaxy NGC 1068 (Planesas *et al.* 1991, Tacconi *et al.* 1994, Helfer and Blitz 1995, Tacconi *et al.* 1997). The bars in starburst galaxies could be thought to be one of the most desirable candidates which provide circumnuclear molecular gas to the inner region of the galaxy (e.g., Kenney *et al.* 1992). Simulations study resolution that the gas must lose its angular momentum to reach the innermost part, an accretion disk, in order to feed AGN. From the recent statistical studies, however, barred galaxies do not preferentially harbour AGN in their centers, suggesting that bars do *not always* play as an important role in energy transport process in AGN, although they are related to central starburst activity (e.g., Ho *et al.* 1995, Sakamoto 1997). The interaction between galaxies is alternative possibility to induce the gravitational instabilities in the disk of the galaxy leading the gas into the nuclear region. In a number of nearby Seyferts, large concentrations of molecular gas within a few hundred parsecs from the center have been detected by imaging of molecular lines, implying the existence of molecular disk/torus in circumnuclear region (e.g., Meixner *et al.* 1990, Young *et al.* 1988).

Tacconi *et al.* (1997) observed molecular gas structure and physical condition in the nuclear region of NGC 1068 (see Figure 2). Jackson *et al.* (1993) observed the rotating dense molecular gas structure in NGC 1068 and found that its rotation axis nearly aligns with the radio continuum jet (see Figure 3). Kohno *et al.* (1996) revealed that 50 - 100 pc scale molecular torus obscures a hidden nucleus of the Seyfert/LINER galaxy M 51. They discussed the kinematics and physical conditions of the molecular torus.

These observational studies have been conducted using millimeter-wave interferometer with a typical angular resolution of several arcseconds, corresponding to 100 pc - 1 kpc for nearby ($D < 30$ Mpc) objects. The resolutions at these wavelengths are still insufficient to resolve the molecular disk/torus structure.

On smaller scales, interferometric observations with VLA (Very Large Array) or MERLIN (Multi-Element Radio-Linked Radio Interferometer Network) allow us to make a high-resolution mapping of nuclear regions of AGN on $\lesssim 100$ pc scales for nearby Seyferts or normal galaxies. In particular, the neutral hydrogen (HI) line might be an effective tool to trace the dusty molecular disk/torus, although it is spatially extended in a galaxy's disk. The inner fronts of molecular disk/torus might be dissociated to some extent by intense UV radiation originated from the central continuum source, so that neutral gas must be present in the disk/torus (Pedlar and Kukula 1994). Also, neutral gas could be a tracer of barred potentials. Using HI to probe circumnuclear regions of AGN can cover a wide range of size-scales and physical processes (e.g., Pedlar *et al.* 1992, Mundell *et al.* 1995).

Kinematics of Molecular Torus/Disk

What is the driving mechanism of interstellar material into the active nucleus ? This is the major and still unresolved problem. The studies of individual sources in their nuclear region will provide a key to answer to this question in establishing of the molecular gas fuelling mechanism (e.g., Kohno 1998).

Several attempts have been made to approach the kinematics and physical conditions of molecular gas in NGC 1068; Jackson *et al.* (1993) discovered the kinematical motion of dense molecular gas ($n_{\text{H}_2} > 10^5 \text{ cm}^{-3}$) traced by HCN(1-0) emission, as shown in Figure 3. They also found that the kinematical (rotation) axis of the HCN structure nearly aligns with that of the radio continuum structure and the biconical jet-like structures (Ulvestad *et al.* 1986) appear to be collimated at the position of the dense molecular gas concentration. Apart from these observations, the CO(2-1) map imaged with the $1''.6$ synthesized beam resolved into the CO *twin peaks* at $r = 100 \text{ pc}$ (Tacconi *et al.* 1997) from the nucleus, where the Inner Lindblad Resonance (ILR) points must be located as much as like in the some barred galaxies (e.g, Kenney *et al.* 1992). These observational facts suggest that the observed dense gas structure is the molecular torus, a reservoir for feeding the interstellar medium deep into the nucleus.

VLBI and the Water Maser Disk

The water vapour masers associated with external galaxies are called a 'megamaser' to distinguish them from those found in stars or galactic star-forming regions. Most of them are known to be extremely luminous ($\gtrsim 100 L_{\odot}$) and exclusively prefer the nuclei of active galaxies (e.g, dos Santos and Lepine 1979, Claussen *et al.* 1984). There is a well-known water maser transition of between the 6_{16} and 5_{23} energy level, which emits at a frequency of 22.235 GHz ($\lambda 1.35 \text{ cm}$). The transition at this wavelength is not so significantly affected by atmospheric effects that we can make the sub-milliarcsecond resolution imaging by means of VLBI, or particularly meant VLBA (Very Long Baseline Array). For the nearby galaxies, the resolution of a sub-milliarcsecond will be on scales as small as $\sim 0.01 \text{ parsec}$, suggesting that it would be a powerful tool for the mapping of nuclear region of AGN. The number of water megamasers that have been detected so far is about twenty, however only six out of twenties have been successfully imaged with VLBA (see Table 2); NGC 4258 (Greenhill *et al.* 1995, Miyoshi *et al.* 1995), NGC 1068 (Greenhill *et al.* 1996), NGC 3079 (Trotter *et al.* 1998, Satoh *et al.* 1998), NGC 4945 (Greenhill *et al.* 1997), NGC 1052 (Claussen *et al.* 1998), and IC 2560 (Nakai *et al.* 1998b). The most prominent result was derived from the nearby AGN, NGC 4258. Nakai *et al.* (1993) discovered the water maser spectrum showing 'high-velocity' features, offset from the systemic velocity of the galaxy to both red and blue-shifted by $\sim 900 \text{ km s}^{-1}$. VLBA observations have shown that the water masers arise in a thin, edge-on torus at a radius of $0.13 - 0.26 \text{ pc}$. As well as being suggestive of a molecular torus on sub-parsec scales, the velocity information gives a strong support for a black hole. The velocities of the masers show a perfect Keplerian rotation curve, which allows to calculate a black hole mass ($\sim 3.6 \times 10^7 M_{\odot}$) confined within a masing torus (Greenhill *et al.* 1995, Miyoshi *et al.* 1995). The 22 GHz continuum emission orientated along the rotation axis of the maser disk is imaged by Herrnstein *et al.* (1998). A sub-parsec scale structure of the water masers and continuum jet surrounding the 'central engine' is shown in Figure 4. This is the finest scale map at a moment in circumnuclear region of AGN.

As in Table 2, the high resolution imaging of megamasers revealed that the water masers lie in a disk in four galaxies (Wilson 1997), but only NGC 4258 is known to trace the Keplerian rotation picture. On the other hand, the three elliptical galaxies are known to contain water masers showing broad features ($\text{FWHM} \simeq 70 \text{ km s}^{-1}$), unlike other disk galaxies (Braatz *et al.* 1995, Koekemoer *et al.* 1995, Nakai *et*

et al. 1998a). The water masers in an elliptical galaxy, NGC 1052 do not lie in a disk surrounding a central engine of the galaxy (Claussen *et al.* 1998), but lie along the radio jet emanating from the nucleus. The masers could be result of amplification of the radio continuum radiation from the jet in the background rather than originated from the dense molecular gas in a disk. In the near future, we might expect that further observations of VLBI would help in finding more perfect evidence for the molecular torus/disk in AGN, as well as black holes.

Absorption Line

In the unified model of AGN, the BLR and continuum emission region are blocked by the optically thick disk/torus that prevent us from direct view of inside obscuring objects, therefore, we might be able to detect emission from the opaque disk/torus. In nearby AGN, a number of species of molecular lines and their isotopes (e.g. CO, NH₃, HCN) have been detected so far on scales of ~ 100 pc. For instance, Planesas *et al.* (1991) found a molecular ring with a radius of 130 pc in NGC 1068 and in Centaurus A, a molecular ring was also detected with a radius of 100 pc by Rydbwck *et al.* (1993). The disadvantage of such molecular thermal emission line studies is that VLBI observations are insensitive to them except for the extremely strong and compact maser lines, so that our research is restricted on scales of 50 pc for nearby Seyferts. Molecular absorption at lines millimeter wavelength have not been clearly detected (Drinkwater *et al.* 1996, Wiklind *et al.* 1996). This could be attributed to the low beam filling factor of molecular disk/torus, compared to the beam size of millimeter-wave telescopes.

The results of survey of the megamaser indicate that a high hydrogen column density ($\gtrsim 10^{22.5}$ atoms cm⁻²) to the line of sight is required to detectable water maser emission (Awaki 1997, Braatz *et al.* 1997). This trend of high HI column density might be correlated with distribution of nuclear absorption to the line of sight. As seen in the earlier section, HI absorption could trace a compact neutral gas, dissociated by radiative excitation from the central continuum source, in the molecular disk/torus (Conway *et al.* 1995). As well as the atomic hydrogen absorption at 21 cm, OH absorption might be a probe of molecular gas in the disk/torus (e.g., van Langevelde 1995). There are several satellite lines at L-band ($\lambda 18$ cm). Both the absorption lines can be observed using ground-based VLBI at a high resolution up to \sim a few mas at $\lambda 18 - 21$ cm at present. We must keep in our mind that information obtained from the absorption is restricted by structure of the background continuum source, however, molecular or atomic hydrogen absorption lines could be a probe of infall or outflow from the nucleus in the circumnuclear region of AGN.

The Rainbow Array

What is the Rainbow Array ?

The Rainbow Array is an imaging telescope located in Nobeyama Radio Observatory (NRO), Nagano, Japan and optimised so as to provide the spectral line images at the wavelength of 2.6, 2, and 1.3 mm. The expected sensitivity resulting from a total combining area of 2000 m² is obtained with *seven* telescopes consisting of the six 10 m NMA antennas and the single 45 m radio telescope. Imaging resolution at $\lambda 1.3$ mm will be about $0''.1$, assuming the maximum baseline length of 400 m for the conventional NMA largest array configuration. The antenna field of view will be $5.5''\lambda$ (mm). The sensitivity of less than 1 mJy per 2 hour integration for continuum emission and 25 mJy per 2 hour and per one spectral line channel

Table 1. Classification of AGNs

Radio Properties	Optical Properties		
	Type 1	Type 2	Peculiar Type
Radio-Loud	BLRG	NLRG	BL Lac
	BLAZAR	FR I	
Radio-Quiet	Quasar(RLQ)	FR II	ULFIRG ^a
	Seyfert 1	Seyfert 2	
	QSO(RQQ)	LINER	

^aUltra Luminous Far-Infrared Galaxies

Table 2. Megamasers imaged with VLBA

Galaxy name	V_{sys} (LSR km s ⁻¹)	Type	$S_{1.35cm}$ (Jy)	Luminosity (L _⊙)	Maser Disk	Velocity gradient	Keplerian rotation
NGC 4258 ^a	472	Sbc	7	110	Yes	Yes	Yes
NGC 1068 ^b	1150	SAb	0.7	180	Yes	Yes	No
NGC 3079 ^c	1116	SBc	3.6	500	Yes	No	No
NGC 4945 ^d	557	SB	9	60	Yes	Yes	No
IC 2560 ^e	2900	SBb	0.3	130	?	Yes	?
NGC 1052 ^f	1618	E4	0.27	200	No	?	No

^aGreenhill *et al.* 1995, Miyoshi *et al.* 1995

^bGreenhill *et al.* 1996

^cTrotter *et al.* 1998

^dGreenhill *et al.* 1997

^eNakai *et al.* 1998b

^fBraatz *et al.* 1995, Claussen *et al.* 1998, van Gorkom *et al.* 1986

for line emission can be observed. The sensitivity and angular resolution attained by the Rainbow Array will provide astronomers with the proper tool for pioneering investigation in millimeter wavelengths. The precise specification of the whole array system will be described in Chapter 2.

Scientific Capabilities of the Rainbow Array

Galactic objects

The measurement of the motions associated with gravitational infall leading to star formation is one of the fundamental subjects in the field of star formation. Infall velocities and spatial structure up to ~ 100 AU are key to our understanding of how stars form. Molecular gas or dust disks around protostars and the properties of these disks resemble those of the early Solar System. These disks might play a central role in the formation of stars. Protoplanetary disks are considered to be responsible to collimation of the molecular outflows, and they regulate the angular momentum evolution of protostars. The Rainbow Array would be able to approach to these sorts of subjects with angular resolution, corresponding to 10 AU ($\lambda 1.3$ mm) at a distance of 100 pc.

Extragalactic objects

The millimeter array, described above, will acquire fundamentally new information on the structures of galaxies. It enables us to investigate the fine scale structures of the objects at a resolution of 0.1 arcsecond: It reveals the kinematics of the optically obscured nuclei of AGN with a resolution of HST – by no other instruments observing at other than radio wavelengths. We can compare the astronomical images obtained by the Rainbow Array with the best optical images. On the other hand, VLA has been the most powerful instrument in the world for studying the neutral gas content of galaxies in the 21 cm line of neutral atomic hydrogen, while the Rainbow Array will be leading the study of carbon monoxide at the better spatial resolutions in the molecular gas. The Rainbow Array will make it possible to understand energy transport processes. The Rainbow Array will allow studies of AGN in two ways: First, CO and dust emission allow us to image the processes responsible for the AGN activity at the millimeter wavelengths. The resolution of 0.1 arcsecond will resolve the kiloparsec-scale galactic disks on the scale of a few hundred parsecs, which is comparable to the nearby extragalactic objects. The interactions and merging between galaxies which might be related to the AGN activity can be studied using CO and other molecules. Second, the observations at $\lambda 1.3$ mm will enable studies of CO $J = 1 - 0$ and $J = 2 - 1$ transitions. Images of two CO transitions will establish the temperature and density in the interstellar medium of the galaxies under the assumed physical conditions.

CO line mapping

Although VLBI can achieve the angular resolution of $0''.001$, it can detect only the high-brightness compact objects ($T_b > 10^5$ K) because of its poor sensitivity. The Rainbow Array, highly sensitive connected array, can observe both the thermal and extended radio emission. The Rainbow Array will cover the observing frequency range typically from 86 GHz to 230 GHz. In this frequency range, two different transitions of CO lines are observable. The CO lines provide us important methods for a wide range of

kinematic and morphological studies. The CO lines are to the study of molecular gas as the 21 cm line is to the astrophysics of the atomic gas, however, observations of multiple CO rotational transitions ($J = 1 - 0$ and $2 - 1$) will enable us to separate abundance effects from those resulting from excitation and optical depth.

Motivation of this Thesis

Search for Circumnuclear Molecular Gas with the Rainbow Array

To date, intensive studies on circumnuclear molecular torus/disk in Seyfert galaxies have been conducted to study kinematics and physical conditions of circumnuclear regions of AGN using millimeter arrays with a few arcsecond resolutions (~ 100 pc in linear scale at the distance of < 30 Mpc). These studies have been successful only in the nearby Seyfert galaxies M 51 and NGC 1068, as stated above. The detailed structures and kinematics of the circumnuclear region, however, are not still clear even in these galaxies at present. Further statistical investigations will be essential to search how typical the molecular torus/disk might be in the circumnuclear region of AGN. In addition, we need to know how the molecular gas is fuelled into the nucleus in relation to the outer galactic disk. The Rainbow Array will be able to image the molecular emission in the extragalactic objects at the resolution of Hubble Space Telescope (HST) and it can probe the molecular gas distribution and properties deep in the active nuclear region of disk galaxies such as Seyferts. Recently, molecular gas has been detected in several radio galaxies (Mazzarella *et al.* 1993), and some of them are known to host the elliptical galaxy (Lees *et al.* 1991). There is increasing indications that the optical imagings of powerful radio galaxies show the morphological peculiarities, suggesting those arising from the collision or merger between galaxies (e.g., Heckman *et al.* 1986). We need for the highly sensitive radio interferometers equipped with the larger collecting area to carry out those researches. The Rainbow Array which consists of the 45 m telescope and NMA is one of the most promising existing facilities that allows us to upgrade the sensitivity and spatial resolution at the same time.

The Rainbow project actually began in 1991 and it has been continuing since then. Meanwhile, some scientific outputs were derived from the experimental runs. In 1997, the NMA back-end system was upgraded into the wide-band and high spectral resolution FX correlator (Chikada *et al.* 1987), and then we were required to design the new SIS receiver system on the NRO 45 m telescope. For the achievement of this upgrading, I performed the development for the receiver and its optics in the 45 m telescope. The receiver system for the Rainbow Array must have been matched to that for NMA to obtain coherent correlations between the 45 m and 10 m telescopes. After construction of the Rainbow system, I carried out the spectral line-mapping observations of radio galaxy, NGC 1275 to study the molecular gas distribution in the circumnuclear region of radio-loud AGN, as well as a final check for the array performance.

Rainbow Array Observations of Radio-loud AGN, NGC 1275

The peculiar type galaxy, NGC 1275 is located in the center of Perseus cluster with a bright radio source 3C 84 in its nucleus and it is known to abound with cold interstellar medium (Lazareff *et al.* 1989, Mirabel *et al.* 1989a, Reuter *et al.* 1993, Braine *et al.* 1995, Inoue *et al.* 1996, Bridges and Irwin 1998) and is, therefore, the one of the most desirable sources to study the relation of circumnuclear gas to the radio-loud property in comparison with that to the radio-quiet's in Seyfert galaxies. The detailed

motivations for NGC 1275 studies will be described below.

- NGC 1275 is too distant ($D = 70$ Mpc) to be resolved in less than 1 kpc scale so far with the existing millimeter interferometers. The nuclear region is expected to be resolved in several hundred parsec scales with the high spatial resolution of Rainbow Array. We can approach to the nuclear region in the comparable scale in which nearby spiral galaxies have ever been intensely searched.
- NGC 1275 enables us to study the energy transport mechanism which sustains the powerful radio activity in relation to the circumnuclear molecular gas. Combining the obtained results with those in Seyfert galaxies, it will be possible to address the origin of activity in radio galaxies.
- The single-dish observation of the radio-loud nucleus of NGC 1275 causes the difficulty in determination of the continuum baselines over the wide passband, because the continuum fluxes tend to produce the bad baseline at millimeter wavelengths. Interferometric Rainbow observations can eliminate this effect.
- The spectrum of NGC 1275 shows the equivalent line velocity width of $\sim 600 \text{ km s}^{-1}$ (FWZI), corresponding to ~ 240 MHz at $\lambda 2.6$ mm. In order to detect the line emission, whose peak flux is only a few % that of continuum flux, the wide reception bandwidth is required for the precise determination of the continuum baseline. Therefore, observations using the wide-band (1024 MHz bandwidth) digital correlator which is involved with the Rainbow system will be crucial for this purpose.

If we can successfully image the inner arcsecond of NGC 1275 and other radio galaxies, there will arise the possibility of establishing the role of the molecular gas in channelling the hot plasma observed in the centimeter wavelengths. There is no other facilities which can reveal the kinematics of the optically-obscured nuclei at a resolution less than $1''$ at present. The Rainbow Array enables these radio galaxies including NGC 1275 to be studied in linear scales of < 1 kpc, which are comparable in nearby Seyfert galaxies.

VLBA Observations of Radio-active Galaxy, NGC 5793

On the other hand, in order that we understand the fine scale structure of circircumnuclear gas, I propose to search for the nuclear region of radio-active galaxy, NGC 5793 mainly using VLBA by use of the water maser spot. It seems reasonable that I should approach one of this major problem – relationship between circumnuclear disk/torus and central activity in AGN – from studying radio-active nuclei in AGN on different scales. In addition to the water maser mapping on sub-parsec scales, I have carried out the VLBI observations of OH molecular absorption with $\sim 0''.01$ resolution, corresponding to ~ 2.5 pc in linear dimension ($D = 50$ Mpc). The VLBI mapping of OH absorption towards AGN has not ever been conducted in such a high-resolution so far. When combined OH, water maser, and CO data in NGC 5793, it will be possible to obtain a fairly complete picture of physical conditions and kinematics of circumnuclear molecular gas, and the effects of central activity to the environments.

Thus, I will present the observational studies of the distribution and kinematics of molecular gas in the circumnuclear region of radio-active galaxy NGC 1275 and NGC 5793 using radio interferometers with different angular resolutions. I believe that there must be the classes of the circumnuclear molecular gas structure which cause apparent anisotropy in AGN family on $0.1 \text{ pc} - 1 \text{ kpc}$ scale. Although the molecular lines provide the principle tools for kinematical and morphological studies, we have no imaging facilities at

millimeter wavelengths with the angular resolution that is competitive with that of VLBI ($\theta_{\text{syn}} \sim 0''.001$ with VLBA at 22 GHz). In order to fill in the spatial resolution gap, I have performed the Rainbow project which attains the maximum angular resolution on scales of the order of $1''$ at millimeter wavelengths. Some of the investigations will require the resolution on scales of the order $1''$ and this will be achieved by the Large Millimeter and Sub-millimeter Array (LMSA) project.

Structure of this Thesis

In Chapter 2, I begin with the summary of technical developments regarding to the newly developed millimeter interferometry system; Rainbow Array, extended NMA mode which is combined with the 45 m radio telescope in NRO. In addition, some measurements and data acquisition processes are briefly described.

Chapter 3 deals with the CO ($J = 1 \rightarrow 0$) observations and detailed data-reduction processes of well-known peculiar galaxy, NGC 1275 (3C 84, Perseus A) using the NMA in Rainbow-mode with the resolution of ~ 1.7 arcsecond at 113 GHz (λ 2.6 mm). The detected CO emission concentrated within ~ 400 pc from the center of the nucleus will be discussed together with the published data at various wavelengths. The NMA observations in D configuration will be presented to follow up the Rainbow results. The Rainbow observation has an implication as a test run to check the array system performance.

The detailed studies of the active galaxy NGC 5793 are also presented in chapter 4 and 5. In Chapter 4, I begin with the study of water maser emission at the transition of 22.235 GHz (1.35 cm) detected in the galaxy and then high-resolution maser mapping using the VLA-A configuration (with an angular resolution of 100 mas) is shown in order to reveal the large scale distribution of the water maser at the nucleus. I conducted VLBA observations at the resolution of 3 mas down in scales towards the active nucleus. The maser distribution within a few pc from a central engine is examined in relation to the continuum emission. Chapter 5 also deals with VLBA observations of NGC 5793. The OH absorption structure against the background continuum source is researched by VLBA at the resolution of ~ 17 mas and its morphologically unusual continuum structure will be discussed with VLBA continuum observations at both L and C-band.

Fig. 2.— An integrated intensity map of CO ($J = 1 \rightarrow 0$) in NGC 1068, observed by Helfer and Blitz (1995). The synthesized beam ($4''.1 \times 3''.7$) is plotted at the bottom left corner. The contours are shown 4, 6, 7, 8, 10, 12 and 14 σ levels, where 1 σ is $5.7 \text{ Jy beam}^{-1} \text{ km s}^{-1}$. In the map, northern and southern spiral arms are connected by a bar-like molecular structure. This nuclear molecular bar whose extent is $25''$ is seen at P.A. $\sim 63^\circ$.

Fig. 3.— The HCN structure in NGC 1068 superposed with the 6 cm continuum image (Jackson *et al.* 1993). The blue-shifted (thick) and red-shifted (dash) contours could trace the rotating molecular gas disk. The rotation axis aligns the direction of the continuum jet-like structure.

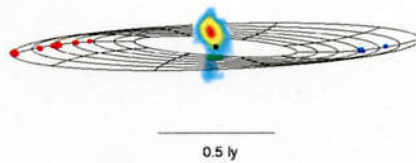


Fig. 4.— The maser disk discovered in NGC 4258. The 22 GHz continuum structure superposed on the maser distribution on the warped disk in sub-parsec scales, presented by Herrnstein *et al.* (1998). The locations of masers are shown by filled circles. The filled square in black expresses the disk center.

Chapter 2

INSTRUMENTATION — 45 M TELESCOPE RECEIVING SYSTEM

Rainbow Array

Overview

The term of 'Rainbow Array' refers to the millimeter wave interferometer with seven elements, that consists of six element Nobeyama Millimeter Array (NMA) and the 45 m telescope in Nobeyama Radio Observatory (NRO) in Japan. The expected sensitivity of Rainbow Array results in a combined collecting area of nearly 1200 m². The achieved baseline sensitivity will be improved by a factor of four better than that of NMA in conventional six array mode. Imaging resolution at 230 GHz (λ 1.3 mm) is expected to be $\sim 0''.7$, for the maximum baseline length of ~ 400 m in the largest configuration.

Since 1980s, the Berkeley-Illinois-Maryland-Association interferometer (BIMA) at Hat Creek, the California Institute of Technology interferometer at Owens Valley (OVRO), Institute of Radio Astronomy Millimeter (IRAM) at Plateau de Bure and NMA have provided a plenty of scientific achievements in every field of Astronomy and all of these millimeter arrays have been currently upgrading to improve mapping speed, sensitivity, resolution, receivers for shorter wavelengths, and correlators for wider bandwidths. Consequently, NMA has no longer superiority over other interferometers both in sensitivity and resolution as shown in Table 1. We have, however, the 45 m radio telescope, known as a millimeter telescope with the largest dish at present, and NMA in our site at Nobeyama. The addition of the 45 m telescope to existing NMA can increase the number of sources observable at λ 1 – 3 mm as a result of improved sensitivity of this extended array. Thus, the Rainbow Array will serve the anchor for the Millimeter Array (MMA) or Large Millimeter and Sub-millimeter Array (LMSA) which are being considered as next generation Sub-millimeter arrays. Here are listed properties of the existing millimeter arrays in Table 1.

A Brief Historical Review

The Rainbow Array project was originally proposed by N.Ukita and R.Kawabe (NRO) in 1991. The array was first tested in 1993 and resulted in successful fringe detection between the 45 m and NMA 10 m

telescopes. Then astronomical observations were conducted for bright galactic objects. The high-resolution maps of Ori-KL and L1551 were obtained with the array. From 1994 to 1996, a number of technical developments have been made both in the 45m telescope and NMA, including the underground optical fibers carrying IF and reference signals. Meanwhile, the test observations had been made every year. In 1997, the FX correlator in NMA back-ends was replaced by the new-FX correlator and UWBC (Ultra Wide Band Correlator) equipped with the higher spectral resolution and wider 2 GHz reception band (DSB), respectively. As a result, intermediate frequency (IF) was also updated ranging from 5.0 – 7.0 GHz. These were conducted to increase array (NMA) sensitivity. (Once the the number and aperture of antennas are fixed, the broad continuum band and spectral resolution are the most important parameters for array sensitivity.) However, the 45 m receiving system has the IF centered on 1.4 GHz. Then, it was necessary to develop the new receiving system with the IF centered on 6.0 GHz and 2 GHz total bandwidth in the 45 m for the Rainbow observation. This is the motivation for describing this Chapter.

The Rainbow System Design

Overview

The performance of NMA by adding the 45m telescope to it would be enhanced mainly to increase array sensitivity and to improve (u,v) coverage. However, design of some systems, especially receiving system in the 45 m, should be made to make it as easy as possible to observe with existing NMA system. To provide compatibility with NMA receiving systems in both RF and IF bands, the 45 m receiver system for the whole Rainbow observation was newly developed. I will present technical aspects of the Rainbow Array system, including an optical feeding system, receivers, astronomical objectives and some measurements in which I had been mainly engaged, with particular emphasis on the development of the new heterodyne receiving system mounted on the 45 m telescope. The detailed description on test observations will be discussed in the next Chapter.

SIS Receiver System

The primary aim of the receiver design is to achieve as low a system temperature as possible. To fulfill this requirement, SIS receivers, the most efficient receivers in millimeter and sub-millimeter astronomy, are being adopted as much as like other receivers, mounted on the 45 m telescope and NMA (e.g., Phillips and Woody 1982).

Major design concept of the receiver is as following.

- Three SIS mixers operating at 100 GHz ($\lambda 3.0$ mm), 150 GHz ($\lambda 2.0$ mm), and 230 GHz ($\lambda 1.3$ mm) are installed in a dewar.
- The dual-frequency reception in two of three bands is required for single-dish observations.
- The first intermediate frequency (IF) bands should cover from 5.0 to 7.0 GHz to match the NMA IF. (By contrast, the 45 m front-end adopts the 1st IF of 1.4 GHz at present.)

The front-end consists of feed-horns, mixer blocks, cross-guide couplers, and cooled HEMT amplifiers for each frequency band, and all of them are installed in the cryogenic dewar. Most of the front-end system

is to be cooled by the closed-cycle cryogenic refrigerators to liquid helium temperatures. The signals at each frequency are fed into the dewar passing through the windows, shielded by the Teflon. The RF signals at each frequency received by a feed-horn, then, are guided in SIS mixers through directional couplers mounted on mixer blocks. The mixers are cooled to ~ 4 K to keep SIS junction inside mixer blocks into the state of superconductivity. The LO power injection is made using this coupler by means of waveguide running from out of the dewar. The LO power generated from the Gunn Oscillator module is applied to a mixer block, where the RF signal accepts heterodyne mixing. In the LO units, oscillators and frequency doubler or tripler provide an output that is tunable over ranges of 86 – 115, 150 – 165, and 210 – 230 GHz, respectively. The mixer has no filter to select one sideband, resulting a double-sideband receiving system.

The first frequency conversion to 5.0 – 7.0 GHz is made at this stage. Then, the converted signal is amplified by the low-noise HEMT amplifier (LNA) with the typical gain of 35 dB over nearly 2 GHz and will be fed to outside of the dewar by way of waveguides. LNA is cooled to ~ 20 K and fixed to the 20 K platform. At the output point of the dewar, the output signal of LNA is amplified by the second IF amplifier with the gain of 30 dB over a range of 4–8 GHz and selectively guided to two paths; one of which goes to the 'band selection board' in the 45m telescope cabin and the other goes to the Interferometer control Building (IB) on the optical fibers via underground.

Block diagrams of front-end and signal path at RF and IF are shown in Figure 1. The summary of these receivers is given in Table 2. The laboratory measurements of a mixer performance are also given in Table 5.

Beam Waveguide (Optics) Design

The main purpose of this section is to give an overview of the quasi-optical feed systems that have been developed for use of the Rainbow Array. To provide the maximum frequency flexibility the 45 m telescope uses the beam wave guide feed. This feeding system allows us to locate a number of feeds and receivers at ground level, with the advantage of more space and easier access to the receiving systems. An optical system designed for the Rainbow is placed under the 45 m reflector shown in Figure 2.

The optics for feeding the signal into the dewar consists of one set of reflectors, one curved and the others plane. The configurations of these mirrors are shown in Figure 3. The incident signal first passes vertically through a circular polarizer converting linearly polarized wave to circular polarization to match the polarization between the 45 m telescope and 10 m antennas. This beam is then reflected horizontally at the plane mirror (#1) and reflected again by the ellipsoidal mirror (#2) to the vertical output. In the case of 100 GHz wave reception the output is initially reflected by the plane mirror (#3) and then reflected by the mirror (#5) to the 100 GHz horn. When 150 GHz wave is received, the reflected output by the plane mirror (#3) is then reflected by the mirror, which is inserted at the location of #4. On the other, 230 GHz reception is realized by removal of the #3 mirror out of the wave path. Finally, the wave at each frequency is transmitted through Teflon lens, placed before the feed horn.

Although the Rainbow Array can receive only a single frequency band at a time, there is a requirement for dual-frequency observations with the 45 m single dish. The requirement for simultaneous observations with a pair of 100 GHz and 150 GHz or 100 GHz and 230 GHz is satisfied with using a plane dichroic reflector (made of wire grids) in the optical system. This is selectively mounted over the 230 GHz feed at the location of #3 in Figure 3. The flat dichroic reflector is transmissible at 230 GHz and reflective at 100 GHz and 150 GHz. When the single frequency receiving mode (Rainbow mode) observation is carried out, it is either replaced by the plane reflector at 100 GHz or 150 GHz, or moved out at 230 GHz.

By insertion of another additional Teflon lens and re-location of the mounted lens before the feed horn

for 230 GHz (see Figure 2), aperture illumination is transformed into the aperture with the radius of 35 m. This is designed for the dual-reception at 100 GHz and 230 GHz in the single dish observation mode to match the beam size of 230 GHz with that of 100 GHz. The adopted parameters (distances between mirrors and etc.) in the optics are summarised in Appendix.

Rainbow Observing System

a. Reference signal

A simplified block diagram of the reference signal distribution system for the local oscillators are shown in Figure 4. We must keep it in our mind that the Rainbow Array is a connected array, therefore, all LO oscillators and timing signals used in the receiving system at each antenna site, including 45 m telescope must be provided common reference signals. The reference signals are originally derived from 5 MHz signal made by the hydrogen maser, a widely-used frequency standard in astronomy.

The 5 MHz reference output of the maser in the equipment room inside 45 m Building (45 B) is transmitted to the NMA IB on a coaxial cable and used to provide reference frequencies for a synthesizer module generating 16 MHz reference. Then, it is multiplied 1696 MHz at NMA IB. This reference is distributed to the 10 m and 45 m antenna sites on optical fibers after being modulated to a digital signal. A frequency multiplier at the IB generates 10 MHz from 5 MHz. Another reference frequency of 25 MHz is derived from the fringe rotator regulating the delay tracking at the IB and these two reference signals are transmitted to the 10 m and 45 m on separate coaxial cables.

In each antenna, LO units consisting of local oscillators (Gunn Oscillators) and Phase Locked Loop (PLL) circuits are equipped. The three reference frequencies are used to drive PLL and local oscillators providing LO power to the SIS mixer.

b. IF and correlator

The design takes advantage of the existing instrumentation at observatory. The NMA back-end at IB, including the correlators that are configured to obtain cross correlations, is used. Optical fibers buried below ground were installed between the 45 m telescope and IB.

The IF signal amplified by LNA in the dewar is digitized by E/O modulator and then transmitted to IB on optical fibers. After A/D conversion, the signals from each site are split into two different components at IB. One of them goes to Ultra Wide Band Correlator (UWBC), in which the sampling frequency of 1024 or 512 MHz with 128 and 512 independent spectral channels, respectively, is used and the other goes to FX correlator using the sampling frequency of 32 MHz with 1024 spectral channels. The digitizing uses 2 bit, 4 level sampling. Thus, signals from 2 telescopes are multiplied followed by integration within a coherent time in the correlator. Details of the NMA correlator system beyond those are described in Okumura (1998).

Array Performance (Expected)

The Rainbow Array consists of seven elements, including the 45 m telescope with the largest radius among the millimeter wave antennas. The resulting baseline sensitivity due to the collection area will be

Table 1. List of millimeter interferometers

Institute	Dish Diameter (m)	Number of Antenna	Total collecting area (m ²)	Observing Frequency Bands (GHz)	Altitude (m)
NMA	10	6	470	86 - 230 155 - 165 (210 - 230)	1400
Rainbow Array	10, 45	7	1225 (2060)	86 - 230	1400
IRAM	15	5	880	86 - 115, 210 - 230 (330 - 360)	2560
OVRO	10.4	6	510	86 - 115 210 - 230	1220
BIMA	6	9	255	86 - 115 210 - 230	1040

Table 2. Characteristics of the receiving system

Nominal frequency (GHz)	Frequency band (GHz)	First IF band (GHz)
100	86 – 116	5.0 – 7.0
150	135 – 160	5.0 – 7.0
230	210 – 230	5.0 – 7.0

¹Double Side Band (DSB) receiving

LO; Local Oscillator
Amp; Amplifier

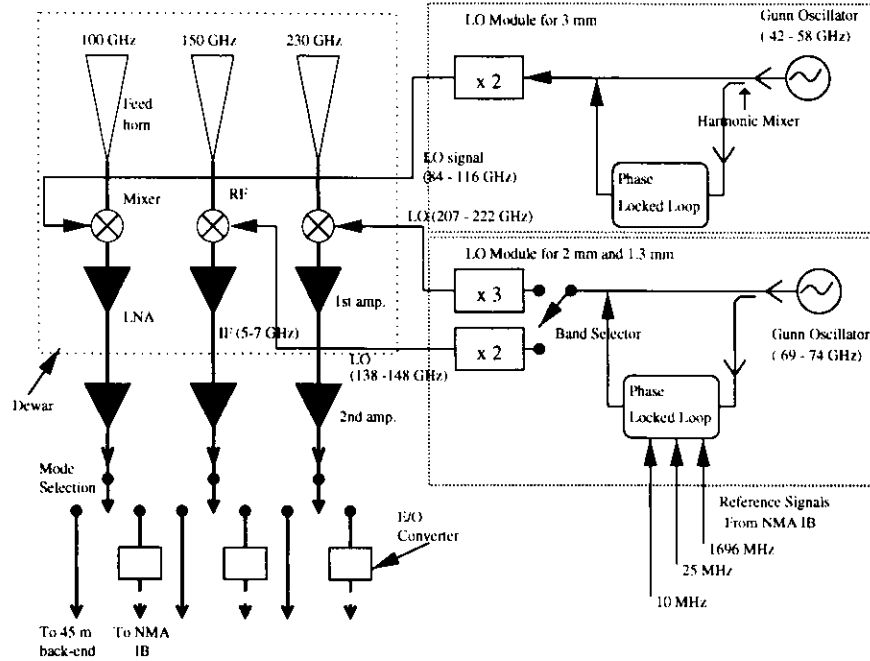


Fig. 1.— Schematic diagram of the Rainbow SIS receiver. The feed horn , mixer block, and HEMT amplifier are cooled to 4 K.

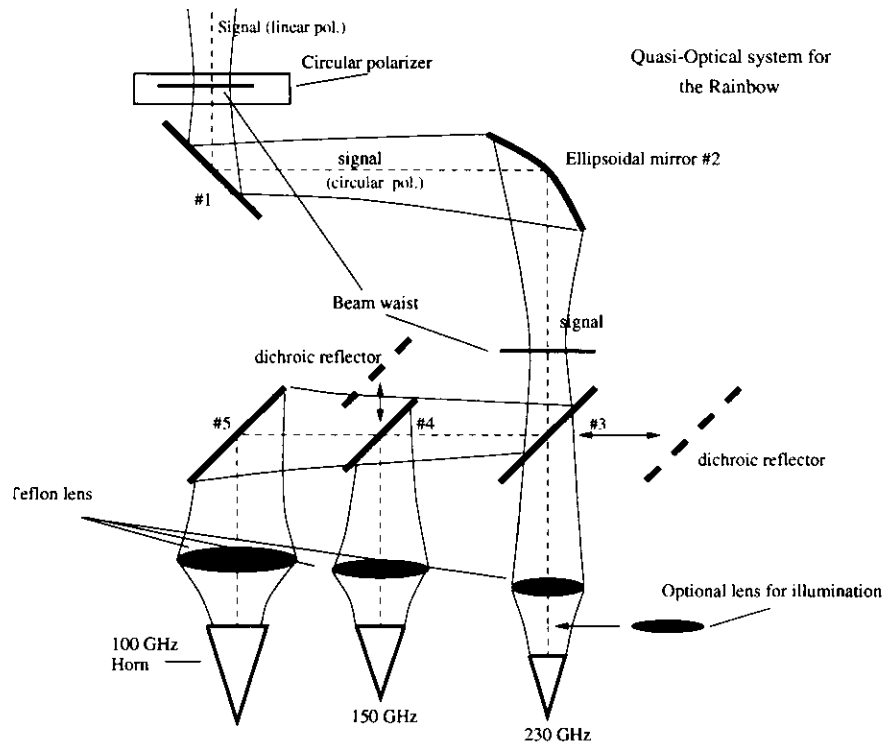


Fig. 2.— Quasi-optical feed system for use of the Rainbow Array

four times as good as that of NMA. The 45m – 10m fringe sensitivity (1σ) is derived from the following estimation,

$$\Delta S_{rms} = 47 \left(\frac{T_{sys}}{500\text{ K}} \right) \left(\frac{\Delta\nu}{1\text{ GHz}} \right)^{-0.5} \left(\frac{t_{int}}{10\text{ min.}} \right)^{-0.5} \quad (\text{mJy beam}^{-1}) \quad (2.1)$$

, where I assumed that the aperture efficiencies of 45m and 10m are 43 % and 78%, respectively. The angular resolutions, shown in Table 3 are limited by baseline length (nearly north – south) of about 400 m. Although a lower spatial resolution is possible due to foreshortening of the baseline, actually this will not be appreciable because of the fixed Rainbow array configuration. The expecting performance (assuming 7 elements) is shown in Table 3. Here we give estimates of the brightness sensitivity and 1σ rms sensitivity in the highest resolution element at 2.6 mm (115 GHz) under good weather conditions.

For continuum observations using UWBC correlator,

$$\Delta T_B = 27 \left(\frac{T_{sys}}{500\text{ K}} \right) \left(\frac{\Delta\nu}{1024\text{ MHz}} \right)^{-0.5} \left(\frac{t_{int}}{4\text{ hrs}} \right)^{-0.5} \left(\frac{\theta_a \times \theta_b}{1'' \times 1''} \right)^{-1} \quad (\text{mK}) \quad (2.2)$$

$$\Delta S_{rms} = 0.76 \left(\frac{T_{sys}}{500\text{ K}} \right) \left(\frac{\Delta\nu}{1024\text{ MHz}} \right)^{-0.5} \left(\frac{t_{int}}{4\text{ hrs.}} \right)^{-0.5} \quad (\text{mJy beam}^{-1}) \quad (2.3)$$

and for spectral line observations using the new-FX correlator,

$$\Delta T_B = 4.8 \left(\frac{T_{sys}}{500\text{ K}} \right) \left(\frac{\Delta\nu}{32\text{ kHz}} \right)^{-0.5} \left(\frac{t_{int}}{4\text{ hrs}} \right)^{-0.5} \left(\frac{\theta_a \times \theta_b}{1'' \times 1''} \right)^{-1} \quad (\text{K}) \quad (2.4)$$

$$\Delta S_{rms} = 0.14 \left(\frac{T_{sys}}{500\text{ K}} \right) \left(\frac{\Delta\nu}{32\text{ kHz}} \right)^{-0.5} \left(\frac{t_{int}}{4\text{ hrs.}} \right)^{-0.5} \quad (\text{Jy beam}^{-1}) \quad (2.5)$$

, where 500 K DSB system temperatures and 50 % aperture efficiencies are assumed. θ is defined as a synthesized beam size.

The expecting sensitivities of other interferometers are listed in Table 4. It is clear from the list that the expecting sensitivities of the Rainbow Array system are superior to those of other interferometers all over the world at present.

Measurements for the Rainbow Array System

Receiver Noise, System Temperature, and Beam Pattern

The examples of the best performance of SIS mixers at 100 GHz ($\lambda 3\text{ mm}$) and 150 GHz ($\lambda 2\text{ mm}$) are shown in Fig 5 and Fig 6, respectively. These data were recorded from mixers installed in the laboratory dewar used for general measurements. The receiver noise temperatures (DSB) are shown as a function of LO frequency, measured at the IF frequency centered on 6.0 GHz. The bandwidths were limited to 500 MHz, determined by the bandpass filter. The noise temperatures for the 100 GHz mixer are between 45 K and 85 K in the range of 86 – 115 GHz. Values down to 70 K (DSB) is attained over the frequency range of 125 – 155 GHz regarding to the 150 GHz mixer, that is the best performance obtained so far. Measurements for a 230 GHz mixer are underway.

The system temperatures of the Rainbow receiver in the 45 m, including the effects of the atmosphere are shown in Table 5. The values were all measured at the frequency of 86.243 GHz, tuned for the SiO

($J = 2 - 1, V = 1$) maser frequency, for the 100 GHz receiver. The system temperature (T_{sys}) is defined as below, where T_{atm} , T_{ant} , and T_{rx} are, atmosphere, antenna and receiver temperature.

$$T_{\text{sys}} = T_{\text{atm}} + T_{\text{ant}} + T_{\text{rx}} \quad (2.6)$$

Beam patterns at 100 GHz and 150 GHz were measured from observations of quasars. The beam pattern of the 3 mm receiver at 86.243 GHz is shown in Figure 7. The FWHP (Full width half power) beam widths were about $16''.5 \pm 3''.3$ at 86 GHz and $12''.5 \pm 2''.5$ at 149 GHz.

The rms sensitivities of the Rainbow receiver are shown in Table 5. The values are estimated as follows,

$$\Delta T = \frac{\sqrt{2} T_{\text{sys}}}{\sqrt{t_{\text{int}} \Delta \nu}} \quad (K) \quad (2.7)$$

where, t_{int} and $\Delta \nu$ is defined as total integration time (sec.) and bandwidths (kHz), respectively. For an integration time of 600 sec. at 2.6 mm (115 GHz), the 1σ noise level will be achieved \sim a few K per 1 spectral channel (37 kHz) for a spatially unresolved objects.

After the receiver performance being verified, I proceeded the measurement of optical feeding systems. First, the beam-squint offsets of the 45m telescope were determined within about 20 % referred to the S100/80 receiver. Then, the beam pattern measurements were carried out to check the calculation of optics. As an example, the beam pattern of the 3 mm feeding system is shown in Figure 7. The measured values of the beam size are listed in Table 5.

Test Observations

a. Single-dish observations

After installation of the receiver in the 45 m telescope receiver room, the single-dish test observations were conducted at both 3 and 2 mm for the galactic SiO maser source VX-sgr and CS($J = 3 \rightarrow 2$) toward Sgr B2 in Galaxy center. The obtained spectral profiles are shown in Figure 8. The result is shown in Table 6.

b. Interferometric test observations

The Rainbow Array equipped with the new front-end system was first tested on 1997 June 8 – 15. After I verified that the instrumentation worked by observing the bright continuum source, I tuned the frequency of SiO ($J = 2 \rightarrow 1, v = 1$) maser at 86.243 GHz and detected the maser line toward Orion KL (see Figure 9). The Figure 9 shows that the peak value ratio between the 45m - 10m and 10m-10m baseline is ≈ 3.5 . This is nearly the expected value of 4, derived from the baseline sensitivities.

Poor weather typical for the rainy season in Nobeyama and short allocation time period did not permit us further progress.

The second period for the test observations was over 1998 January 28 – February 6. The weather was relatively good, and this time we observed at the 150 GHz. This experimental observations pursued two directions as follows;

- intense baseline calibration, so as to determine the baseline error between the 45 m and 10 m telescope with an accuracy of $\simeq 0.1 \lambda$. The problem of errors are considered as follows: 1) Focal

point of sub-reflector of the 45 m varies as a function of the telescope elevation due to homologous deformations of the telescope structure. 2) The cable expansion and contraction. 3) The uneven surface of the AZ rail of the 45 m. Apart from these, there found the error which causes gradual time-dependent variation.

- to check the capability of imaging of the array, by observing astronomical objects with both continuum and line emission.

We tracked the phases of compact continuum sources, such as 3C 273 over two nights for baseline calibration. All the data were used to make a rough estimation of the baseline. The intense determination of the baseline is still underway.

c. Mapping test observations

The astronomical observations consist of three sessions, the hydrogen recombination line emission from the galactic HII region of MWC 349 at $\lambda 2$ mm, CO ($J = 1 \rightarrow 0$) molecular line from the radio galaxy, NGC 1275 (3C 84), and thermal continuum emission from the proto star candidate, L 1551. In the next Chapter, I will show the data reduction and scientific results of NGC 1275 in detail.

Here we show the continuum image of L 1551 at 2 mm in Fig 10. The rms noise of this map is ~ 7 mJy, obtained with the 1024 MHz passband. The noise level in this map is almost consistent with the derived sensitivity of ~ 3 mJy (see Table 6). The peak flux density of the image is about 60 mJy beam^{-1} with a synthesized beam of 2.0×0.8 arcsec.. The continuum source is known to contain thermal emission from the dust around the proto star. The source size, intensity and structure are consistent with the previous obtained image at $\lambda 2.6$ mm.

Summary

I broke down the summary of this chapter as follows:

- Due to the replacement of the NMA correlator system in 1997, development for new receiving system in the 45m telescope was required in order to carry out the Rainbow observations connecting NMA to the 45 m. I was involved in the beam waveguide and SIS receiver design.
- The new Rainbow SIS receivers enable observations at the frequency of 100 GHz, 150 GHz and 230 GHz with the wide reception bandwidth (1 GHz) or the high spectral resolutions. To fulfill requirements for single-dish observations, the receivers were designed available for the dual-frequency (100 – 230 GHz, 100 – 150 GHz) reception. The circular-polarizer which was newly developed is used to match the polarizations between the 45 m and 10 m telescopes.
- After installation of the receiving system in the 45 m telescope, the whole system that I designed was examined by measurements on the 45 m telescope.
- After successful fringe detection between the 45 m and 10 m, the several test runs were carried out to check the imaging capabilities of the Rainbow Array in both the continuum and spectral line, and finally the high performance of the Rainbow was verified.

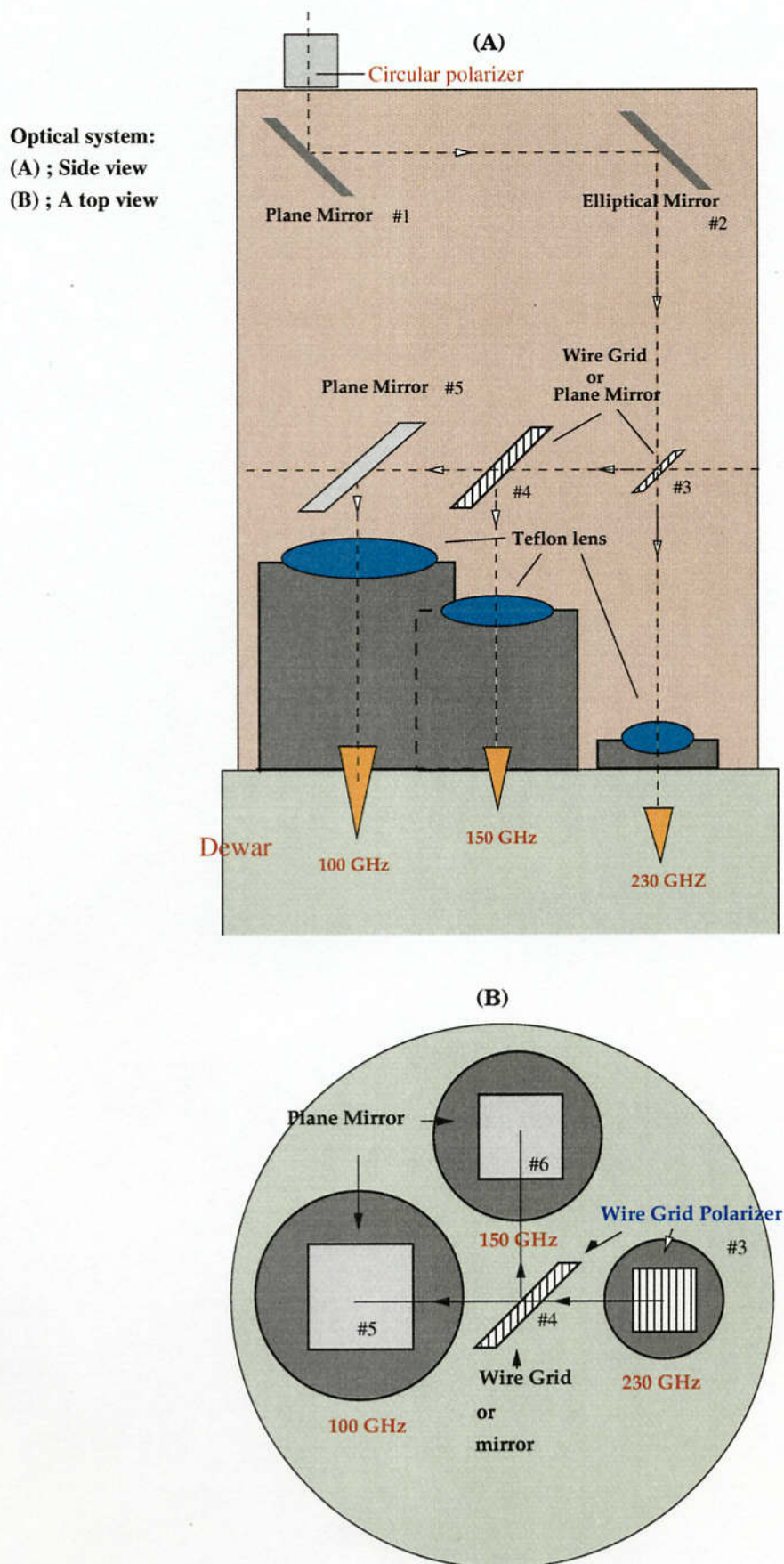


Fig. 3.— The schematic view of optical elements in the Rainbow feeding system

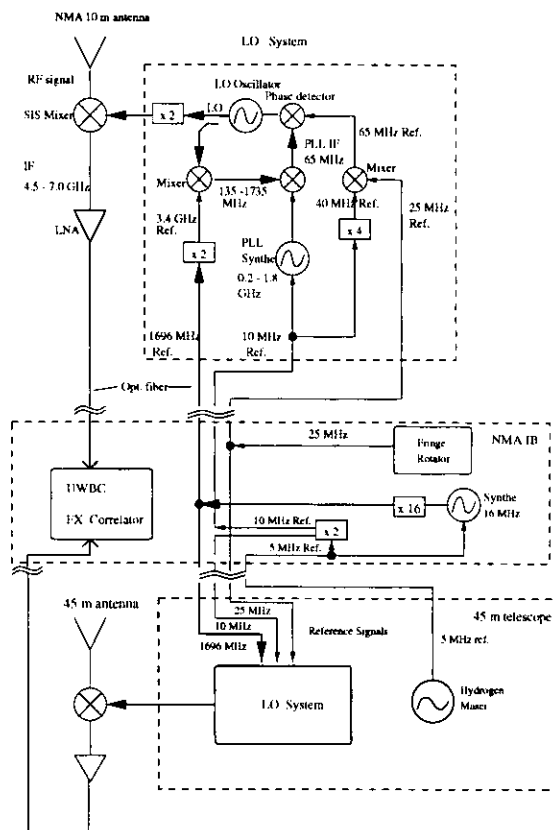


Fig. 4.— Distribution of local oscillator reference frequencies
3mm SIS

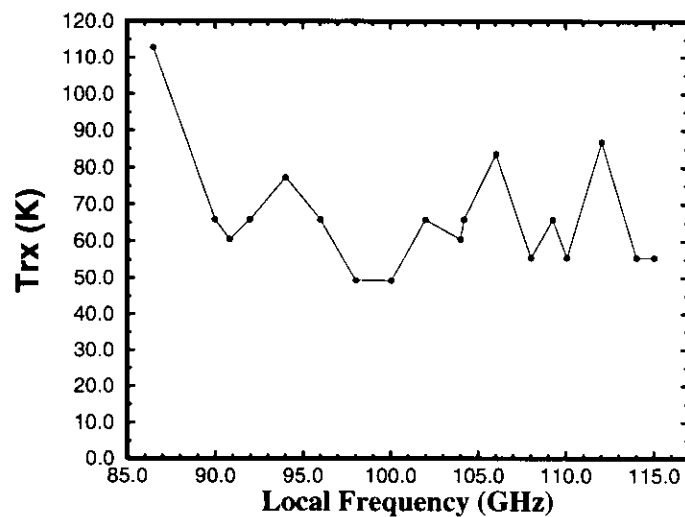


Fig. 5.— A plot of receiver noise temperatures for 100 GHz mixers, operating at 85 - 115 GHz, as a function of Local (LO) frequency.

Table 3. Expecting performance of the Rainbow Array

Nominal frequency	100 GHz	150 GHz	230 GHz
Number of correlations	21		
Maximum bandwidths (UWBC)	1024 MHz		
Synthesized beam (AB configuration)	1.0 arcsec.	0.8 arcsec.	0.5 arcsec.
Minimum Velocity resolution (FX)	0.10 km s ⁻¹	0.075 km s ⁻¹	0.050 km s ⁻¹
Continuum sensitivity (4 hrs) ($\Delta\nu = 1024$ MHz)	27 mK	30 mK	45 mK
Line sensitivity (4 hrs) ($\Delta\nu = 32$ kHz)	4.8 K	5.3 K	8.0 K

Aperture efficiencies are assumed to be 0.5 ($\lambda 2.6$ mm), 0.4 ($\lambda 2$ mm), and 0.3 ($\lambda 1.3$ mm).

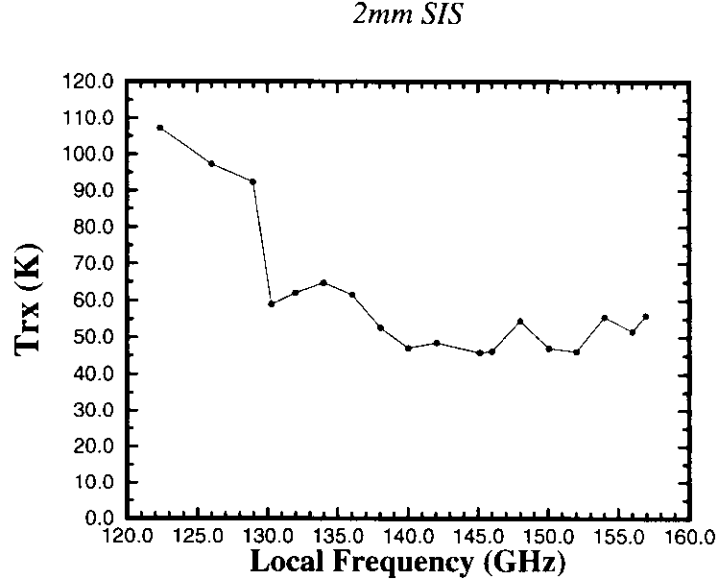


Fig. 6.— A plot of receiver noise temperatures for 150 GHz mixers, operating at 135 – 155 GHz, as a function of Local (LO) frequency.

Table 4. Sensitivities of millimeter-wave arrays at 3 mm

	Rainbow	IRAM	OVRO
Number of correlations	21	10	15
Maximum bandwidths (GHz)	1	0.5	1
Minimum frequency resolution (MHz)	0.03	0.04	0.04
Continuum sensitivity ^{a b}			
ΔS (mJy beam ⁻¹)	0.76	1.1	1.2
ΔT (K)	0.027	0.10	0.11
Line sensitivity ^{a c}			
ΔS (mJy beam ⁻¹)	24	25	40
ΔT (K)	0.86	2.2	4.0

^a 1.0×1.0 arcsec² beam, 4 hours integration, Tsys = 500 K (SSB)

^b Assuming the maximum bandwidth

^c Assuming $\Delta\nu = 1$ MHz

Table 5. Measured performance of the receiving system

Wavelength	3 mm	2 mm
Bands (GHz)	86 – 115	135 – 160
Primary beam size (FWHM) (arcsec.)	16±3	12±3
Trx (K) ¹	50 – 75	45 – 70
Tsys (K)	310	350
Line sensitivity (single-dish) ²	0.2 K ³	0.06 K

¹Receiver noise temperature

²The spectral resolution is 0.25 MHz and on-source time is 20 minutes.

³Due to the poor weather condition and the high Tsys value

Table 6. Sensitivities derived from test observations

Test mode	1σ	1σ
	Estimated Value	Measured Value
45m single-dish ¹ (20 min. integ.)	0.11 K	0.12 K
Fringe sensitivity ² (10 min. integ.)	7.5 mJy	12 mJy
Mapping sensitivity ³ (4 hrs integ.)	3 mJy	7 mJy

¹ CS ($J = 3 \rightarrow 2$), 146.96 GHz., $T_{\text{sys}} = 1000$ K(DSB), $\Delta B = 0.25$ MHz

² 3C 84 observations, $T_{\text{sys}} = 500$ K, $\Delta B = 300$ MHz

³ From the continuum map of L1551 in Figure 10, $T_{\text{sys}} = 500$ K, $\Delta B = 1024$ MHz

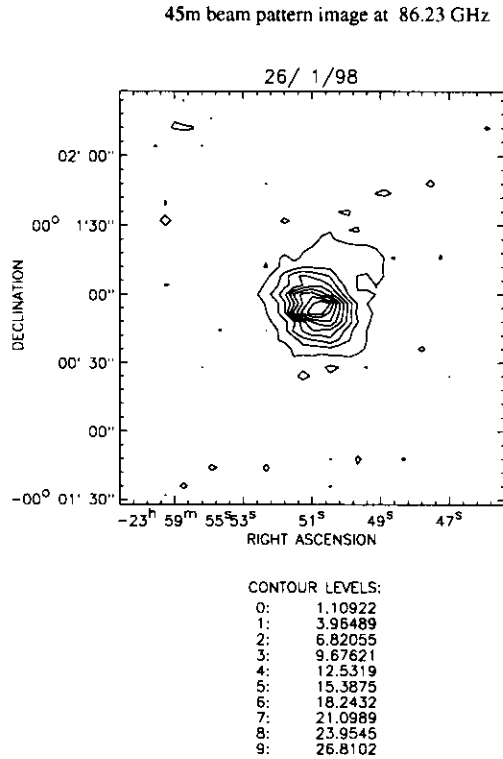


Fig. 7.— The beam pattern of the 3 mm receiver, mounted on the telescope. The measurement was done at 86.24 GHz.

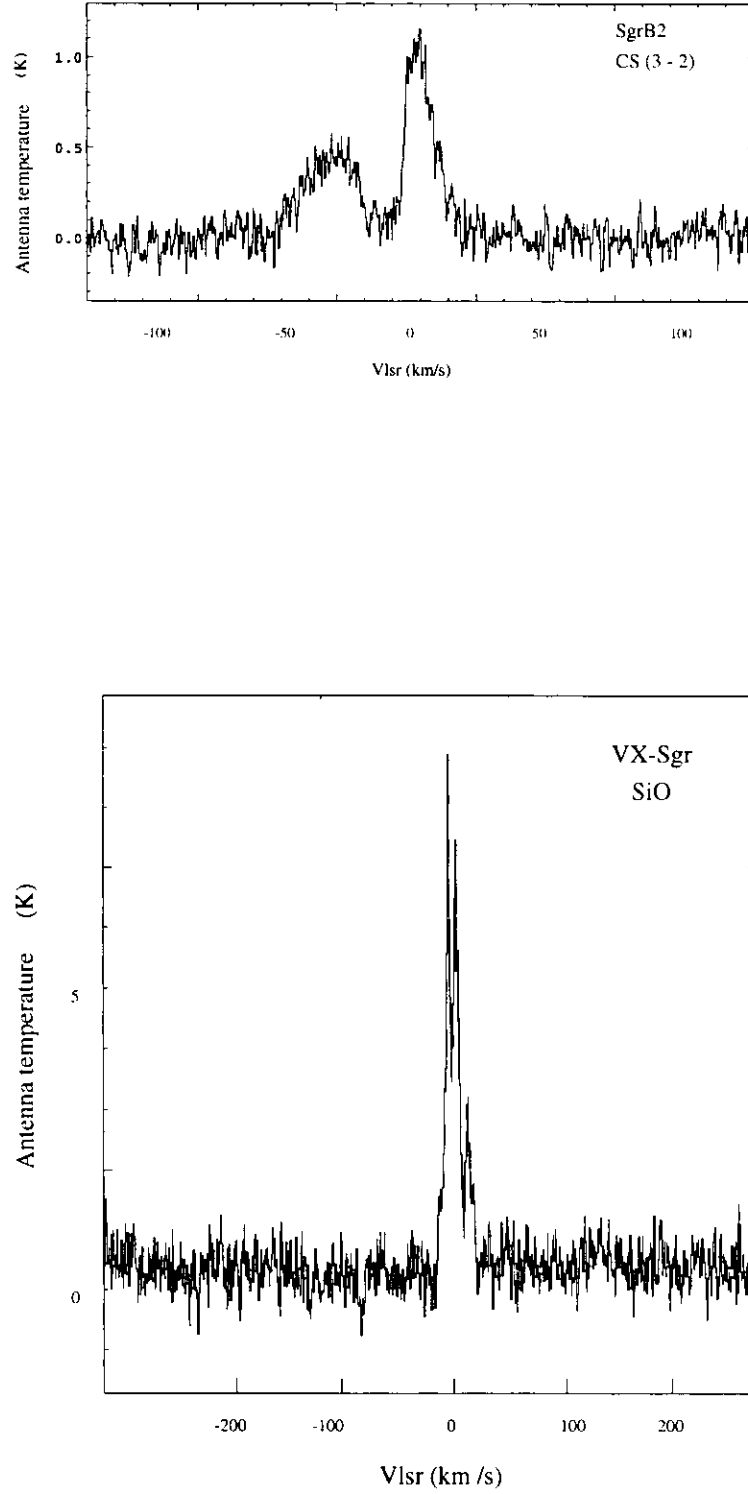


Fig. 8.— *Upper*: A profile of SgrB2 with the 2 mm receiver, tuned CS ($J = 3 \rightarrow 2$). *Lower*: A profile of the SiO ($J = 2 \rightarrow 1, v = 1$) VX-Sgr with the 3 mm receiver.

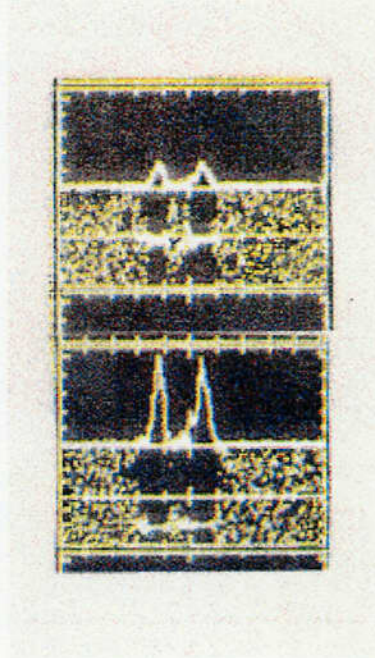


Fig. 9.— The fringe detection of 10m –10m (upper panel) and 45m – 10m baselines (lower panel). The profiles shows SiO ($J = 2 \rightarrow 1, v = 1$) maser emission in Ori-KL.

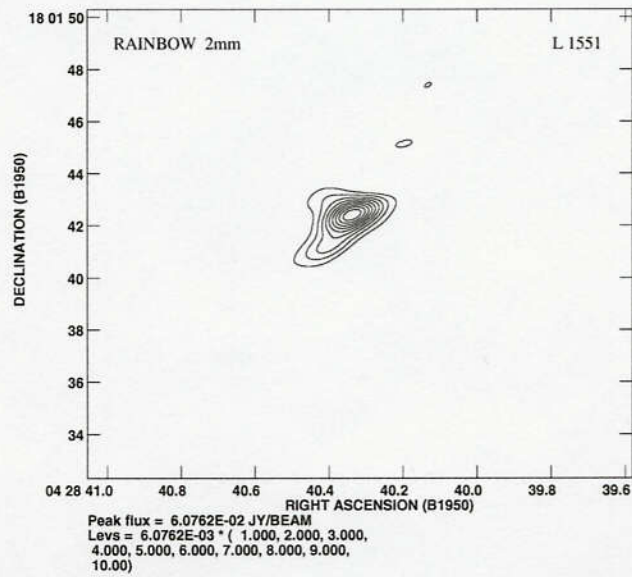


Fig. 10.— The $\lambda = 2$ mm dust emission in L 1551 observed with the Rainbow Array. The rms noise level in this map is about 7 mJy beam⁻¹.

Chapter 3

NUCLEAR MOLECULAR GAS IN NGC 1275 – CO OBSERVATION WITH THE RAINBOW ARRAY

Introduction

NGC 1275 (Perseus A) is one of the best studied galaxies. The galaxy and its nucleus have been studied extensively at various wavelengths. NGC 1275 was considered one of the Seyfert galaxies, discovered in 1943 (Seyfert 1943) with an unusually bright and starlike nucleus showing broad emission lines. Among the first six Seyferts only NGC 1275 was not spiral, showing a peculiar morphology in many respects. Since then, over eight hundred papers have been published on this galaxy to date.

NGC 1275 is a cD galaxy identified with Perseus A at the center of Perseus cluster (Figure 1) and known to have Seyfert-like nucleus in its center and a powerful radio source (3C 84) with a jet-like structure (Figure 1) in various scales (e.g., Pedlar *et al.* 1990). The 21 cm lines of atomic hydrogen had been detected in absorption at two widely separated velocities (Minkowski *et al.* 1957, Burbidge and Burbidge 1965). One of the two velocity components was detected at the velocity of $\sim 5200 \text{ km s}^{-1}$, and is referred to be the systemic velocity of NGC 1275. This feature was considered to be the line emission associated with the optical filamentary structure (Lynds 1970). Another component, at $\sim 8120 \text{ km s}^{-1}$, is red-shifted by nearly 3000 km s^{-1} to the systemic velocity and is consistent with the velocity of the gas filament system, which is at $40''$ off the nucleus (de Young *et al.* 1973). Ekers *et al.* (1976) showed that HI absorbing region is smaller than a few arcsecond in extent and centered within $1''$ on the nuclear continuum source. These authors considered an interpretation involving absorption from a superposition of galaxies in the cluster, as well as the ejection hypothesis, in which the absorbing gas is ejected from NGC 1275 at a constant velocity. The presence of the foreground high-velocity system might imply that NGC 1275 has experienced a previous merger. Thus, the origin of the highly red-shifted HI absorption has not been well understood.

X-ray observations with EINSTEIN detected the significant X-ray emission from the Perseus cluster involving NGC 1275, indicating the existence of thermal hot gas. Its origin was interpreted as an emission from a cooling flow with a mass accretion rate of $200 - 300 M_{\odot} \text{ yr}^{-1}$ (Mushotzky *et al.* 1981, Fabian *et al.* 1984, Fabian 1994), however, the fate of this cooling flow gas has been controversial. The most recent ROSAT data show the excess X-ray absorption in the central $30''$ in the cluster and the total mass of

$\sim 10^8 M_{\odot}$ is estimated (Allen and Fabian 1997). It has been argued that such a large concentration of cooling flow gas or absorption gas in the foreground galaxy has a relation to the existence of interstellar cold gas and dense molecular clouds. The radio core in NGC 1275 might heat the latter gas to the detectable temperatures, while the former gas remains cold in Perseus cluster.

Several observations demonstrate the presence of a young stellar population in NGC 1275. Shields and Filippenko (1990) first detected the blue stellar clusters at the systemic velocity both in the nucleus and an H II like region $\sim 20''$ from the nucleus, which they conclude is a young blue cluster. The broad-band HST observations revealed the luminous, blue, and unresolved objects in the 5 kpc region from the nucleus (Holtzman *et al.* 1992). The CFHT (3.6 m CFH Telescope) photometric observations to follow up these HST results confirmed that young and luminous star clusters were formed continuously at least over the past 10^8 years in the central 8 kpc region (Richer *et al.* 1993). The processes of the star-formation were interpreted as the results of massive cooling flow and masses up to $10^7 M_{\odot}$ are estimated for the most massive clusters. The H α emission lines associated with the some clusters detected by them were observed (Ferruit and Pecontal 1994). Those argument support the presence of star-forming activity in the center of NGC 1275.

On the other hand, radio observations of HI absorption and CO emission could trace the cold interstellar matter in powerful radio galaxies, while HI emission at 21 cm is extremely difficult to observe because of the strong radio continuum emission. Molecular line emission at millimeter wave proved to be an alternative method to lead physical and kinematical studies in the circumnuclear region of the powerful radio galaxies (Mirabel *et al.* 1989a, Mirabel 1989b).

A detection of CO ($J = 1 \rightarrow 0$) in the galaxy was reported with the NRAO 12 m and IRAM 30 m by Mirabel *et al.* 1989a and Lazareff *et al.* 1989, respectively. According to their results, nearly $\sim 10^{10} M_{\odot}$ of cold molecular exists in the central region. The amount of total calculated molecular mass is consistent with the estimation from IRAS 100 μm flux. The presence of such large amounts of molecular gas in the central a few kpc of the galaxy can be explained by; central starburst activity induced by galaxy-to-galaxy merger/interaction or the cooling flow gas in the center of NGC 1275. Thus, NGC 1275 is the promising candidate to investigate gas kinematics in the circumnuclear region of radio-active galaxies.

Inoue *et al.* 1996 have observed CO ($1-0$) at high-resolution ($\sim 5''$) with NMA in the center of NGC 1275 (Figure 2). Their results indicate that the asymmetric CO distribution within $r \sim 10$ kpc from the nucleus is similar to that of H α extending westward up to 40 kpc (e.g., Heckman *et al.* 1989) and CO emission arises mainly from the *twin peaks* constituting the parts of ring-like structure surrounding the nucleus. The fact that these *twin peaks* are located near the edge of the dust lane detected by HST (Holtzman *et al.* 1992) is similar to the crowding of gas near the inner Lindblad resonances (ILR) seen in some barred galaxies (e.g., Kenney *et al.* 1992). In addition, they observed the hydrogen molecule at 2.1 μm in emission concentrated at the nucleus and unresolved by the beam size of $2''$ (~ 700 pc). Their interpretation is that a turbulent motion of molecular clumps triggered by shocks with a velocity of 100 km s^{-1} is expected in this small region. Apart from Inoue *et al.* (1996), Braine *et al.* (1995) also carried out synthesis mapping observations of NGC 1275 using the IRAM interferometer with an angular resolution of $\sim 2''$. Their study was intended to search for the molecular absorption system toward the radio nucleus of this galaxy, but failed to detect it at the central continuum source. Empirically, dynamical structures traced by molecular gas have been found in 100 pc scales from the galaxy center, suggesting that we should study the innermost region also in NGC 1275 with the finest spatial resolution.

In this Chapter, I will present the high spatial resolution imaging of NGC 1275 to search for the molecular gas disk/torus in its circumnuclear region in hoping that I will find the particular gas fueling mechanism in the radio galaxy in comparison to that in radio-quiet objects. The structure inner 1 kpc region from the nucleus will be revealed by use of Rainbow Array system with higher angular resolution

and sensitivity. The results of observations will be discussed together with those of NMA-D (the compact array).

Observations and Data Analysis

Observations

a. Rainbow observations

The Rainbow observations of NGC 1275 were made at 113.14 GHz (CO $J = 1 \rightarrow 0$) on January 28, 29 1998. The array consists of the existing Nobeyama Millimeter Array (NMA) in its highest resolution (AB) configuration and the 45 m telescope of Nobeyama Radio Observatory (NRO). (The array consists of five 10 m telescopes and the 45 m telescope with a total of 15 simultaneous baselines.) The system temperatures are typically 500 – 800 K in the double side band, corrected for antenna and atmospheric losses. Spectral resolution was provided by a digital correlator (UWBC) configured with 128×8 MHz channels. The velocity resolution is 20.8 km s^{-1} at 113.13 GHz. A full-track of ten hours was used to synthesize a uniformly weighted $1''.7 \times 0''.8$ beam. The total usable integration time on NGC 1275 is 7 hr. The amplitude response of the bandpass was calibrated through observations of the compact bright continuum source of 3C 454.3, 0923+392, and 3C 273. Instrumental phase calibration is based on observations of 3C 84 itself. The absolute flux value was determined from the observations of Jupiter, and is good to $\approx 10\%$.

The array involved the 45 m telescope with a large main reflector, therefore the pointing was checked frequently on nearby SiO maser sources at Q-band every 1.5 hrs to minimize the pointing errors. Due to the uncertainty of baseline between the 45 m – 10 m telescope baselines, we required to do additional baseline corrections. This will be discussed in the following section. The array configuration and resulting (u,v) track are presented in Figure 3 and Figure 4, respectively. Observing parameters are listed in Table 2. The data reduction process is briefly summarized in Fig. 6.

b. NMA-D observations

NMA was also used in its compact spatial-resolution configuration (D) on December 29 1997 at 113.14 GHz (CO ($J = 1 \rightarrow 0$)) to image the extended CO emission within $r = 20''$ in NGC 1275 and estimate reliability of the Rainbow maps. The system temperatures are typically 500 – 800 K in the double side band, corrected for antenna and atmospheric losses. Spectral resolution was provided by a digital correlator (UWBC) configured with 128×8 MHz channels. The velocity resolution corresponds to 20.8 km s^{-1} at 113.13 GHz. The data were obtained from about a 8 hr observation. The total usable integration time on NGC 1275 is 4.5 hr. The resulting synthesized beam size is $8''.9 \times 5''.9$ (natural weight) in P.A. = -20° . The observing parameters are almost the same as those used in the Rainbow observations (see Table 3). The bandpass calibration was conducted through observations of the compact, bright continuum source of 3C 273. Phases were calibrated using 3C 84 (NGC 1275) itself. The absolute flux density of 3C 84 was determined from Jupiter with an accuracy of 10 %. After the self-calibration using the AIPS task of ASCAL, the calibrated continuum phases and gains were applied to the spectral line visibilities using the task ASCOR. Then the spectral imaging was carried out.

Table 1. Summary of NGC 1275.

Parameter	Value
R.A. (1950) ^a ...	3 ^h 16 ^m 29 ^s .57
Dec. (1950) ^a ...	41°19′51″94
Adopted distance ^b ...	70 Mpc
Systemic velocity (LSR) ^c ...	5273 ± 18 km s ⁻¹
Morphological type ...	cD
Magnitude	12 mag.
log P(0.4 GHz) ^d ...	25.22 W Hz ⁻¹
Flux density (1.4 GHz) ^e ...	21.1 Jy
(8.3 GHz) ...	33.6 Jy
(22.2 GHz) ...	43.4 Jy
(110.0 GHz) ^f ...	4.3 Jy
(IRAS 100 μm) ...	6.98 Jy
(IRAS 60 μm) ...	7.15 Jy
(IRAS 25 μm) ...	3.54 Jy
L _{IR} ^g	1.0 × 10 ¹⁰ L _⊙

^aFrom the position of radio core determined by VLA (Whiteoak *et al.* 1987)

^bAssuming $H_0 = 75 \text{ km s}^{-1} \text{ Mpc}^{-1}$

^cSystemic velocity referred from Inoue *et al.* 1996

^dMirabel *et al.* 1989a

^eWhite and Becker 1992

^fNMA flux measurement (1997 Dec.)

^gKawara and Taniguchi 1993

Fig. 1.— *left*: An optical broad-band image of NGC 1275, obtained by the Palomar 48 inch Schmidt. The image size is $11'.0 \times 11'.0$. $1'.0 = 21$ kpc ($D = 70$ Mpc). *right*: The MERLIN 73 cm image of the radio structure of 3C 84 at the resolution $1''.2$. The contour begins at ± 12 mJy beam $^{-1}$ and intervals 12 mJy beam $^{-1}$ up to 238 mJy beam $^{-1}$. The peak flux density is 8370 mJy beam $^{-1}$ (Pedlar et al. 1983).

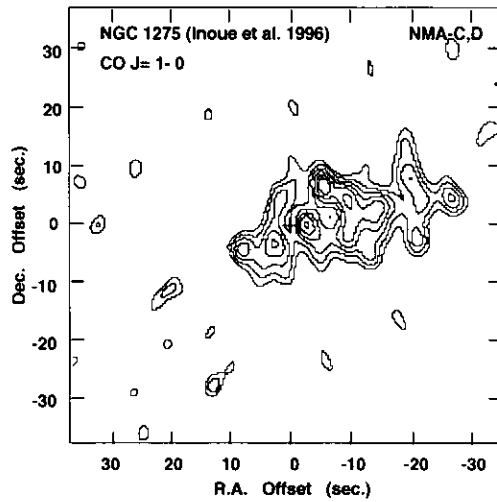


Fig. 2.— A velocity-integrated map of CO ($J = 1 \rightarrow 0$) emission in NGC 1275 using NMA-C,D, observed by Inoue et al. (1996). The velocity range covers $V_{\text{LSR}} = 4971 - 5577$ km s $^{-1}$. The synthesized beam size is $5''.1 \times 3''.6$ in P.A. = 5.6° . The rms noise level is 10 mJy beam $^{-1}$. The contour interval is 10 mJy beam $^{-1}$ and the lowest contour is 20 mJy beam $^{-1}$. The map center (phase center) is marked by a cross.

Table 2. Observing parameters for the Rainbow

Parameter	Value
Observation date	1998 Jan. 28, 29
Array Configuration	AB (Rainbow Mode)
Phase center position	
Right Ascension (1950)	$3^h 16^m 29^s.57$
Declination (1950)	$41^\circ 19' 51''.84$
Total observation time	10 hr
Total on-source time	7 hr
Number of correlations	15
Primary beam of the 45 m telescope (FWHP)	$16''$
Synthesized beam (FWHM, uniform weight)	$1''.7 \times 0''.8$
Line (transition)	CO ($J = 1 \rightarrow 0$)
Rest frequency	115.271204 GHz
Velocity center (LSR)	5600 km s^{-1}
Observing frequency	113.139188 GHz
Bandpass Calibrator	3C 273
Phase Calibrator	3C 84 (4.3 Jy at ~ 110 GHz)
Bandwidth	1024 MHz
Velocity coverage	2650 km s^{-1}
Total number of the spectral channel	128
Velocity (frequency) resolution	20.8 km s^{-1} (8 MHz)

Table 3. Observing parameters for the NMA-D

Parameter	Value
Observation date	1997 Dec. 29
Array Configuration	D (the most compact array)
Phase center position	
Right Ascension (1950)	$3^h 16^m 29^s.57$
Declination (1950)	$41^\circ 19' 51''.84$
Total observation time	8 hr
Total on-source time	4.5 hr
Number of correlations	15
Primary beam of the 10 m telescope (FWHP)	$72''$
Synthesized beam (FWHM, natural weight)	$8''.9 \times 5''.9$
Line (transition)	CO ($J = 1 \rightarrow 0$)
Rest frequency	115.271204 GHz
Velocity center (LSR)	5600 km s^{-1}
Observing frequency	113.139188 GHz
Bandpass Calibrator	3C 273
Phase Calibrator	3C 84 (4.3 Jy at ~ 110 GHz)
Bandwidth	1024 MHz
Velocity coverage	2650 km s^{-1}
Total number of the spectral channel	128
Velocity (frequency) resolution	20.8 km s^{-1} (8 MHz)

Data Reduction for the Rainbow

a. Self-calibration

One of the purposes of this observation is to examine the imaging capabilities of the newly built-up interferometer system. The problem is that there remains uncertainty of the 45 m baselines, introduced by the homologous deformation of the 45 m main reflector, uneven surface of the AZ rail, and other unidentified effects. The geometric delay in phase ($\Delta\phi_g$) is related to the separation of the phase centers of two antennas (b) as the following:

$$\Delta\phi_g = \frac{2\pi s_t \cdot b}{\lambda} \quad (3.1)$$

, where s_t is a unit vector towards the center of the target and λ is wavelength of the signal.

In conventional millimeter radio interferometric imaging we attempt to estimate and remove the phase errors using phase-referencing method. Due to the variation of phase errors in observations, we use calibrator observations to determine instrumental phase errors. We refer to this technique as phase-referencing. We involve the regular observations of a nearby relatively bright objects such as quasars to use phase corrections and the phase of the referenced point source is applied to the target visibility data. The effects of baseline errors, however, relate to the angular separation between the target and reference source:

$$\Delta\phi_g = \frac{2\pi b \cdot (s_t - s_{cal})}{\lambda} \quad (3.2)$$

, where s_{cal} is the calibrator source vector. The wider target-reference separation is, the larger the phase error. This phase error will contribute to the position error in the image. In contrast, if we assume that the target source is used as well as a phase calibrator, the phase errors would be negligible, even if large baseline errors still remain.

Instead of using the calibrator source to estimate phase errors, it is possible to use the target source itself to calibrate the phase data. This method is known as self-calibration. In this case the target source of NGC 1275 is a bright continuum source with peak flux density of ~ 4 Jy at 2.6 mm, such that self-calibration technique might be applicable to this object. In addition to it, the effect baseline errors are minimized in the image quality.

b. Data Analysis

Data reduction of line emission based on self-calibration technique proceeded as diagrammed in Figure 6.

'Sub-ref' correction: What we should do first is to make corrections of a shift of focal point caused by sub-reflectors and then we apply the solutions to the raw visibility data. The mean value of the shift is given approximately by the phase-connection value as follows:

$$\Delta\phi_{subr} = \frac{4\pi S (1 - \sin EL)}{\lambda}, \quad (3.3)$$

where $S = 23$ mm, EL is an elevation angle of the main reflector.

Bandpass correction: Then we proceed to bandpass correction. The peak line flux with single-dish observations is ~ 500 mJy at CO (1–0), and the flux with NMA-C,D configuration with the synthesized beam of $\sim 5''$ is ~ 80 mJy beam $^{-1}$ (Inoue *et al.* 1996). Then, the peak line-to-continuum emission ratio ($\sim 2 - 12$ %, assuming the continuum flux density to be 4 Jy) of the galaxy is expected to be so small that it might be critical to obtain high spectral dynamic range. As mentioned above 3C 273 was used as a bandpass calibrator by observing about 30 min. at the end of each observation period, resulting the rms noise of 3 % per channel (8 MHz). Actually, we made bandpass tables by averaging the spectral channels over 8 channels (64 MHz) and attained the rms level being less than 1%.

Continuum baseline determination: The relative phases of 45 m – 10 m baselines over the whole bandwidth vary slightly as a function of time during the observation period. This error caused a linear phase slope ($15 - 20^\circ$) seen over the passband of 1024 MHz and was removed by complex dividing using NGC 1275 itself in the visibility data in order that we might be able to obtain linear baseline over the passband. The resultant rms sensitivity of the baseline error is estimated to be $30 \sim 40$ mJy per one baseline. The continuum baseline level was determined from averages of line-free frequency channels between 20 – 60 and 98 – 115 channels. The continuum was then subtracted from the spectral visibilities to produce continuum-free visibilities. The continuum subtraction error introduced by baseline determination was estimated to be 19 mJy beam $^{-1}$, estimated from the cleaned continuum image.

Imaging: Phase calibrations were provided by observations of NGC 1275 itself. The absolute flux calibration was determined from observations of planets with an error of typically 10 %. The phase solutions obtained from the continuum data in self-calibration process using AIPS were, finally, applied to the line data that does not contain continuum emission. The details will be discussed in the following sections.

Data Reduction for the NMA-D

The visibilities are divided into the continuum and spectral line visibilities after the removal of bad data points. The continuum baseline was determined from an average of line-free frequency channels between 20 – 60 th and 98 – 115 th channels and the continuum was then subtracted in the (u,v) plane. The self-calibration process follows after that, using the continuum visibility set. After the self-calibration using the AIPS task of ASCAL, the calibrated continuum phases and gains were applied to the spectral line visibilities using ASCOR. Then the spectral imaging was carried out.

Results

The Rainbow

a. Continuum

Continuum emission visibilities were obtained from the 7 hr integration by averaging across the continuum regions of spectra (69 spectral channels), excluding the line emission regions (32 channels) and the edges of the observing band. The effective continuum bandwidth is about 450 MHz. The resulting images are shown in Figure 7. The rms noise is about 19.0 mJy beam $^{-1}$ and the beam size is $1''.7 \times 0''.8$

(uniform weight) and P.A.= -73° . The measured total flux density of continuum emission is 4.3 ± 0.5 Jy at ~ 110 GHz. The absolute flux measurements for 3C 84 were repeated for several times throughout observing season of 1997 – 1998. Its variabilities had been within systematic errors that arise in data reduction process of flux calibration observations. Using the above values, I proceeded the self-calibration in both phases and amplitudes with the AIPS task ASCAL and the resultant peak flux density is 3.83 Jy beam^{-1} in the cleaned continuum image.

b. Velocity-integrated maps

The spectral visibilities obtained after continuum subtraction and self-calibration were averaged in time about 7 hr. Figure 8 show the velocity-integrated maps ($V_{\text{LSR}} = 5030 - 5250$ km s^{-1}). The rms noise levels are ~ 19 mJy beam^{-1} in a uniformly weighted map and 12 mJy beam^{-1} in a naturally weighted map. The peak flux densities are 112 mJy beam^{-1} and 84 mJy beam^{-1} in a uniformly and naturally weighted map, respectively. The CO emission in both images are observed at the center position higher than a 5σ detection level. In the uniformly weighting map, a Rayleigh-Jeans brightness temperature averaged over the beam area for the central CO peak is about 6 K at $\lambda = 2.6$ mm.

Figure 8 shows that the unresolved CO emission peak is detected only at the continuum center position. This result should be compared to the previous observations as the followings: Reuter *et al.* (1993) found the CO (1–0) emission peak at the position of continuum center with the $21''$ beam size of the IRAM 30 m. In the Inoue *et al.* (1996) map obtained from NMA-C,D configurations, the CO (1–0) peak is resolved and split into the *twin peaks* with a separation of $7''$ and one can find no intense CO emission at the center of the view field. In the Rainbow map, the central unresolved CO emission is prominent with an angular size of about $2'' \times 1''$ ($1''$.0 corresponds to 350 pc at the distance of 70 Mpc), and therefore the CO emission in the Rainbow map is seen concentrated $r \lesssim 400$ pc region. Thus, the results derived from the previous NMA observations by Inoue *et al.* (1996) are inconsistent with those by the Rainbow observations. This discrepancy will be discussed in the later section.

The total flux intensity estimated from the NMA spectrum in Fig 11 is 28.8 ± 2.9 Jy km s^{-1} . The resultant uncertainty is due to absolute flux calibration error.

c. Velocity channel maps and spectrum

In Figure 9 and Figure 10, the velocity channel maps with 82.8 km s^{-1} velocity width in the range of $V_{\text{LSR}} \simeq 4855 - 5515$ km s^{-1} are shown, whose visibilities are weighted uniformly and naturally, respectively. The rms noise in each map is ~ 28 mJy beam^{-1} (uniform) and 13 mJy beam^{-1} (natural). The peak flux density is 230 mJy beam^{-1} at the $V_{\text{LSR}} = 5144$ km s^{-1} in the uniform-weight map and 180 mJy beam^{-1} in the natural-weight map. We must note that the CO line emission in the center of the field of view ($r \lesssim 1.5$ arcsec.) is clearly detected at the three channels $V_{\text{LSR}} = 5060, 5144$, and 5227 km s^{-1} .

In Figure 11, the interferometric spectrum integrated over the $2''$ region centered on the continuum point source at the NGC 1275 nucleus is shown ($\Delta v = 20.8$ km s^{-1} , natural weight). The spectrum is plotted together with that obtained using the IRAM 30 m telescope (Reuter *et al.* 1993).

In Fig 12, the interferometric spectrum made in the same manner as Figure 11, plotted together with H_2 $v = 1 - 0$ S(1) emission at 2.1 μm (Inoue *et al.* 1996) is shown. Although in Figure 9 and Figure 10 negative contours are seen at the continuum center position, this might be due to the continuum subtraction error. This trend is also found in the CO spectrum in Figure 11.

The CO emission is seen at $V_{\text{LSR}} = 5020 - 5270 \text{ km s}^{-1}$ and arises only from the continuum center position likewise the velocity-integrated map. The velocity channel maps consist of eight velocity channels in total and there are five line-free channels (corresponding to $\Delta V \simeq 420 \text{ km s}^{-1}$) in which neither continuum nor line emission is detected. The CO line spectrum in Figure 11 also shows that the CO (1–0) emission is detected only in eleven velocity channels, which correspond to $\Delta V \simeq 230 \text{ km s}^{-1}$ and no emission is found in other channels. The existence of line-free channels suggests that continuum subtraction in the (u,v) plane worked well and there remains no continuum emission over the velocity range. The weaker negative components offset from the center position in velocity-channel maps might be due to the phase calibration or the continuum subtraction errors.

It should be noted that the CO (1–0) emission is seen only on the center and on the blue side of the line, in contrast to the CO (1–0) spectrum obtained with the IRAM 30 m and the NMA reported by Reuter et al. (1993) and Inoue *et al.* (1996), respectively. In order to check that the central CO peak and asymmetry in velocity are real, I accessed the earlier NMA-D low spatial resolution ($\simeq 9''$) CO (1–0) data, which were obtained on 28 – 29 December in 1997. The description related to that is in the following section.

c. Achieved mapping performance of the Rainbow Array

The resulting synthesized beam of the Rainbow array and NMA in AB configuration made by discarding only the 45m baselines are listed in Table 4. Thus, the continuous 7 hr track of NGC 1275 produced the synthesized beam size of $2'' \times 1''.1$ for NMA-AB and $1''.7 \times 0''.8$ for the Rainbow (uniform weighting). To enhance the 45 m baseline sensitivity, the weighting factor of 4 is applied to the 45m-baselines, following the expecting baseline sensitivity. The Rainbow beam size is improved by $\sim 20\%$ better than that of NMA-AB, the highest resolution configuration consisting of only 10 m dishes. Rms noise levels in velocity-channel maps are 46 mJy beam^{-1} and 28 mJy beam^{-1} with NMA-AB and the Rainbow, respectively. The effect of the 45 m baselines resulted in improvement of relative sensitivity by a factor of 1.6. This is close to the estimated array sensitivity ratio (~ 2.5) between the Rainbow Array and NMA. The absolute mapping sensitivity is larger by the factor of three than the calculated rms noise level.

NMA-D

a. Velocity-integrated map

Figure 15 shows a velocity-integrated map ($V_{\text{LSR}} = 5070 - 5190 \text{ km s}^{-1}$) obtained by NMA in D configuration, plotted with the Rainbow map to compare difference in mapping scales. It is noteworthy that the CO (1–0) emission peak is seen at the center of the nucleus with an extended linear structure in P.A. $\simeq -70^\circ$. The central CO emission peak in this map is consistent to the results obtained by the Rainbow in contrast to the lack of the CO peak in published NMA images. The rms noise level is $\sim 17 \text{ mJy beam}^{-1}$. No primary beam response was corrected, since the emission is seen only in the center. The peak flux density is $129 \text{ mJy beam}^{-1}$, so the intensity of CO in this map is higher than 5σ detection level. The CO integrated intensity from the central $12''$ in Figure 15, measured by about $9''$ beam, is $16.6 \pm 2.3 \text{ Jy km s}^{-1}$, while the CO intensity from the central $65''$ with about $5''$ beam reported by Inoue *et al.* (1996) is $640 \pm 130 \text{ Jy km s}^{-1}$. The explanation for differences between these values are as follows; 1) the follow-up NMA-D observation does not pick up the extended weaker CO emission because of the poor sensitivity:

The number of visibility in this observation is fewer than that in their map due to the shorter integration time (4.5 hrs) compared with that they used (22.5 hr). The rms noise level of NMA-D data is calculated poorer by ~ 2.2 than that of Inoue *et al.* from the theoretical noise estimation, however, the resultant rms noise in their map is 10 mJy beam^{-1} , whereas 16 mJy beam^{-1} in this map. There must be some other reasons to increase noise in this map such as weather conditions, data-calibration errors, and so on.

In Figure 17, the NMA-D CO (1–0) velocity-integrated map is shown superposed on the previous NMA-C,D CO (1–0) image (Inoue *et al.* 1996). The CO distribution apparently seems to bridge between CO *twin peaks* detected by them. However, CO *twin peaks* are not definitely detected in this observation. The details for that will be discussed in the following section. Figure ?? shows the superimposed image on the narrow band CCD image of H α and [N II] emission at the systemic velocity, obtained at Lick Observatory. The CO emission nearly coincides with the central emission.

b. Velocity channel map and spectrum

In Figure 13, the velocity channel maps with 82.8 km s^{-1} velocity width in the range of $V_{\text{LSR}} = 4855 - 5515 \text{ km s}^{-1}$ are shown (natural weight). The peak flux density is $114 \text{ mJy beam}^{-1}$ with the rms of 22 mJy beam^{-1} . The CO emission is seen only at the $V_{\text{LSR}} = 5144 \text{ km s}^{-1}$ channel.

In Figure 14, the interferometric spectrum integrated over the $5''$ region centered on the continuum point source is shown. The spectrum is plotted together with that obtained using the IRAM 30 m telescope. The CO ($J = 1 \rightarrow 0$) emission is seen over $V_{\text{LSR}} = 5070 - 5190 \text{ km s}^{-1}$. The integrated-velocity range in Figure 15 is determined from this spectrum. The asymmetries in velocity structures are similar to those in Figure 14.

Thus, the lower resolution NMA-D array data confirmed that the presence of the central CO peak in the Rainbow map is real.

Discussion

Compact CO Emission at the Nucleus: Comparison with Inoue *et al.*

The most interesting result which these observations address is the discovery of the central CO peak in the inner arcsecond of NGC 1275. The compact CO (1–0) line emission is found to be significantly concentrated within $r = 400 \text{ pc}$ from the center. The total integrated intensity of $28.8 \text{ Jy km s}^{-1}$ is about 4.5 % of that derived from an estimation in Inoue *et al.* (1996). Assuming for a Galactic CO-to- H_2 conversion factor of $2.8 \times 10^{20} \text{ cm}^{-2} (\text{K km s}^{-1})^{-1}$ (Bloeman *et al.* 1986), the total molecular mass (M_{H_2}) within 1 kpc from the center is calculated as follows:

$$M_{\text{H}_2} = 1.4 \times 10^9 \left(\frac{I_{\text{CO}}}{28.8 \text{ Jy km s}^{-1}} \right) \left(\frac{D}{70 \text{ Mpc}} \right)^2 M_{\odot} \pm 1.3 \times 10^8 M_{\odot} \quad (3.4)$$

, where I_{CO} and D represent the total CO intensity in Jy km s^{-1} and distance to the galaxy in Mpc, respectively. The derived molecular mass is comparable to that in nearby Seyferts with gaseous nuclei, such as NGC 1068 or NGC 3079 (e.g., Scoville *et al.* 1988b) and the far-infrared luminous galaxies in merger/interacting process (e.g., Sanders *et al.* 1988). The derived M_{H_2} value can be compared to that of Lazareff *et al.* (1989) and Reuter *et al.* (1993) who observed CO (1–0) with the IRAM 30 m with $21''$ beam and estimated $M_{\text{H}_2} = 2.7 - 6.0 \times 10^9 M_{\odot}$. Mirabel *et al.* (1989a) found the $M_{\text{H}_2} = 3.2 \times 10^9$

M_{\odot} within a beam area of $55''$ with the NRAO 12 m telescope. From the interferometric observations by Inoue *et al.* with a $\sim 5''$ synthesized beam, the M_{H_2} within the radius of $4''$ from the continuum center is $8.6 \times 10^9 M_{\odot}$ and the $3.0 \times 10^{10} M_{\odot}$ over the primary beam of $72''$. Thus, the M_{H_2} obtained with the Rainbow Array within the radius of $1''$ from the center is smaller than that by any other previous CO (1–0) measurements, suggesting that I observed the molecular gas arising from the very compact region in the nucleus.

The determination of the M_{H_2} strongly depends on the Galactic conversion factor. We must note that the molecular gas condition in the cluster is different from that in the Galactic region.

Due to the narrower $16''$ field of view limited by the primary beam size of the 45 m telescope, the CO emission extending up to $30''$ (~ 10 kpc) in the east-west direction seen in the published NMA image is not detected in the Rainbow images, while the central CO emission ($r \lesssim 400$ pc) with high brightness was identified in the Rainbow image. The IRAM single-dish observations identified the both CO (1–0) and CO (2–1) peak at the nucleus with the beam size of $21''$ and $12''$, respectively (Reuter *et al.* 1993). Those results are consistent to the maps imaged by both the Rainbow Array and NMA-D in that they found the CO peak at the center, though the resolutions are larger. The failure to detect the CO emission at the center position in the previously obtained NMA maps imaged by Inoue *et al.* seems to be due to the continuum subtraction error. It is plausible that they subtract the central line emission peak as well as the continuum component at the center. This probably causes the relative weakness of the line emission at the central a few arcsecond region. The total continuum bandwidth used for determination of the continuum baseline is as much as 450 MHz in the Rainbow observation, while the bandwidth available for them is at most 50 MHz (total bandwidth is 320 MHz). The accuracy of determination of the continuum baseline must have been improved in my images, compared with that in their images. Considering these facts, I am confident that the CO peak at the nucleus is real.

The smaller Rainbow synthesized beam determined by the 45 m telescope can explain that the extended components which are visible in the previous maps are completely resolved out and only compact component with the high brightness at the center remained unresolved in the image. The distribution of CO line emission in NMA-D map (see Figure 17) is seen as an elongation from east-west to north-west direction in P.A. = -70° , that is nearly consistent with the previous results. In the velocity-integrated maps, neither the CO *twin peaks* nor molecular ring with a radius of 1.2 kpc around the center, reported by Inoue *et al.* (1996), was found. This discrepancy could be attributed to the poor sensitivity due to shorter integration time (4.5 hr) and spatial resolution ($9''$) of the NMA-D map. It is possible that the $9''$ beam size produced by NMA-D was not sufficient to resolve the CO *twin peaks* with an only $7''$ separation. As a check that the CO *twin peaks* are real in their map, the additional NMA observations at a higher angular resolution should be conducted.

The extended CO component in NMA-D map looks like bar-like structure and the central peak emission appears to be linked by the blue clusters seen in the center of the broad-band HST image (Holtzman *et al.* 1992), as displayed in Figure 16.

H₂ Emission at the Nucleus

According to Inoue *et al.* (1996), they found the $2.1 \mu m$ H₂ emission to be unresolved within $r \lesssim 350$ pc at the continuum center position (see Figure 12) because of the instrumental limitation of $2''$ slit size. The spatial distribution of H₂ emission is roughly consistent with the CO (1–0) distribution detected within $r \lesssim 350$ pc from the nucleus. They believe that H₂ line is excited at ~ 1800 K, being possibly explained by the shock induced by the collisions of gas clouds. According to the estimation of molecular gas density,

$N(\text{H}_2) = 8.4 \times 10^{17} \text{ cm}^{-2}$ (Inoue *et al.* 1996), this derived value is smaller by a magnitude of five than that estimated from the CO (1–0) intensity. This implies that only a small fraction of molecular gas is excited to such a high temperature at the nucleus.

Interpretation of the central CO peak

The CO emission is seen only on the blue side of the line spectrum with respect to the systemic velocity. The previous interferometric or single-dish observations show the quite good symmetrical CO distribution to the systemic velocity of NGC 1275. There is conflict between those results. The explanation for that is as follows. The CO emission on the red side of the line is mainly seen on the east of the nucleus in the previous map, where the line intensity is relatively weaker and CO emission is extended, and hence the smaller Rainbow synthesized beam ($1''$) have resolved the CO emission at the east. As a result, only the blue-shifted emission remains in the velocity maps. As far as the follow-up NMA-D results are concerned, its poor sensitivity and low spatial resolution could not pick up the red-shifted features on the east. Alternatively, though less plausible, there happened the spectral variation during observing epochs. Thus, the CO observations with the Rainbow detected one of the velocity features reported in the previous NMA maps.

If the molecular mass estimated in the previous section is uniformly distributed over a range of radius 400 pc, the mean gas density per volume (n_{H_2}) is estimated only $\sim 300 \text{ cm}^{-3}$. This value is too small to form molecular torus at the nucleus. The gas must be confined to the smaller region, thin, dense gas disk/torus with the density of $\sim 10^5 \text{ cm}^{-3}$ (Matsushita *et al.* 1998). The CO (1–0) molecular emission at the nucleus in NGC 1068 is resolved into two peaks at $r < 100 \text{ pc}$ from the center (Tacconi *et al.* 1997) in CO (2–1) observations, which implies evidence for molecular torus. The further interferometric investigation with the higher angular resolution would be crucial to discriminate the unresolved molecular torus at the center of NGC 1275.

Origin of Molecular Gas

The molecular mass concentration of $\sim 10^9 M_{\odot}$ in circumnuclear region ($< 1 \text{ kpc}$) is similar to that in nearby Seyfert galaxy NGC 1068, while the asymmetric distribution of molecular gas in the published single-dish or interferometric maps is unusual even in the gas-rich spirals and it seems to have relation with the origin of the gas. The similarity between the distribution of $\text{H}\alpha$ and CO emission, extending nearly 10 kpc from the center, suggests the cooling flow motion of the cold material out of the galaxy as is proposed in many published papers. However the cooling process of cold gas is not clear and it is hard to explain the elongated CO distribution by use of the cooling flow model.

We can compare the integrated-intensity image of the central CO emission with the HST image, involved with the previously published CO image in Figure 16, showing a morphological correlation especially between the central CO emission in the blue cluster and the CO *twin peaks* associated with the dark lanes. It should be noted that the detected CO peak in the center is located between *twin peaks* in Figure 16. The spatial distribution of young clusters seems not to be so much different from the extended CO emission (Holtzman *et al.* 1992, Richer *et al.* 1993, Norgaard *et al.* 1993, Inoue *et al.* 1996). The total mass of the young clusters is estimated to be $10^6 M_{\odot}$ (Richer *et al.* 1993), which is smaller by the three order of magnitude than that derived from the central CO emission ($r < 400 \text{ pc}$). This implies that

only a small fraction of the molecular gas was used for production of stellar clusters in the central region.

Inoue *et al.* (1996) argues that their observed CO peaks are located where the extent of dark lanes meets the ring-like orbit of molecular gas in Figure 16. This is suggestive that the observed CO ring-like structure is very much like that seen in several barred spirals. The central CO emission peak and molecular bar-like structure imply the similarity to the barred spirals where the non-axisymmetric potential is considered to be the driving source of gas onto the nucleus (Ishizuki *et al.* 1990, Kenney *et al.* 1992).

Comparison with NGC 1068

In Table 5 are shown the physical parameters of NGC 1275 in comparison with those of NGC 1068. It is very interesting that the nuclear mass to the inner ring ($r < 1.2$ kpc) mass ratio ($M_{\text{H}_2}(\text{nucleus})/M_{\text{H}_2}(\text{ring})$) in NGC 1275 is about 10 % and this trend is also common to the central 1.5 kpc in NGC 1068 (Table 5). According to Shlosman *et al.* (1989), this percentage is a critical for a ring collapse in a two dimensional simulation of self-gravitating gas. The fact that ratios of nuclear molecular gas to the total mass interior to the ring or spiral arms are the same in both galaxies would prove the presence of similar physical process which connects between the large-scale galactic disk and nuclear region.

Based on the morphological properties which I derived from the data both in this thesis and previous results by Inoue *et al.*, I conclude that the circumnuclear region in NGC 1275 has striking similarities in morphology with that in NGC 1068. Those two have following common molecular gas structures in their circumnuclear regions: the ring-like or spiral arms structures at the radius 1.2 – 1.5 kpc from the nucleus, the molecular bar-like structure which overlays the distribution of the young stellar population, and the nuclear gas concentration. The latter two common structures have become clear for the first time in this thesis. The central continuous structure, nuclear bar, in NGC 1068 is detected in CO ($J = 1 \rightarrow 0$) with BIMA (Helfer and Blitz 1995), of which extent is in good agreement with that of $2.1 \mu\text{m}$ stellar bar (Scoville *et al.* 1988a, Helfer and Blitz 1995) where the young clusters exist. In NGC 1068, it is assumed that the molecular bar plays an important role in driving non-circular motions to lead the molecular gas falling onto the nucleus in the inner part of the galaxy (e.g., Combes and Gerin 1985). In the case of NGC 1275, the bar-like structure between CO *twin peaks* in Figure 17 is found and its location can be overlaid with stellar clusters optically identified at the systemic velocity of NGC 1275 (Shields and Filippenko 1990). HST revealed the blue young clusters (Holtzman *et al.* 1992, Norgaard *et al.* 1993) at the central 8 kpc region. By analogy with NGC 1068, here propose a model of gas transport mechanism in NGC 1275; the molecular gas in the ring-like structure at $r \approx 1.2$ kpc is transported along the molecular bar-like structure into the nuclear region abounding with molecular gas, which feeds the central engine: origin of its radio activity. The schematic view for this explanation is shown in Figure 18.

It is likely that some fractions of molecular gas were consumed as a fuel for star formation undergoing at the nucleus. The value of $L_{\text{IR}} / M_{\text{H}_2}$ is used as an index to compare the starforming activity in galaxies. Adopting $L_{\text{IR}} = 1.0 \times 10^{11} L_{\odot}$ estimated from IRAS $100 \mu\text{m}$ flux (Kawara and Taniguchi 1993) and $M_{\text{H}_2} = 1.4 \times 10^9 M_{\odot}$ ($r < 400$ pc), $L_{\text{IR}} / M_{\text{H}_2}$ will be $\sim 70 L_{\odot} M_{\odot}^{-1}$. This value is larger than that of the typical starburst nucleus ($\sim 20 L_{\odot} M_{\odot}^{-1}$), induced by the galaxy interaction/merger (Young and Devereux 1991). This is suggestive of intense starburst in the nuclear region of NGC 1275.

It is noteworthy that the circumnuclear gas surrounding the radio-loud nucleus of NGC 1275 has a similar structure with that around the radio-quiet nucleus of NGC 1068. I suggest, therefore, that what determines the radio activity in NGC 1275 is *not* the circumnuclear gas around the nucleus, but it might relate to the nature of the central engine which produces strong radio-jet.

Summary

In this chapter, I have presented the high-resolution interferometric CO ($J = 1 \rightarrow 0$) images of radio-loud AGN, NGC 1275. The data was obtained mainly from the Rainbow Array observations. The additional data were also obtained by conventional NMA in D configuration. I discussed the relationship between the extended structure of NGC 1275 on larger than 1 kpc scale and the CO concentration at the nucleus of the galaxy on less than 1 kpc scale. The important results of this study are as follows:

1. The observations of NGC 1275 were made to examine the line-mapping performance as well as pursuing the scientific outputs of the new Rainbow Array. The shift of the focal point of the 45m telescope during observations causes uncertainty of the delay offset value between the 45 m – 10 m baselines, though the self-calibration technique eliminated this effect in data reduction process. We must note that this kind of calibration method can be available when the target source happens to be a strong radio continuum source itself like NGC 1275 (3C 84). In order to carry out the imaging observation in any other objects, we will have to establish a method for baseline calibration for the 45 m telescope baselines. In these observations the expected *relative* mapping sensitivities at 2.6 mm were nearly achieved by addition of the 45 m telescope to NMA. The absolute value of sensitivities were higher by a factor of five than the value estimated from the thermal rms noise. This could not be due to the array performance, but to the incompleteness of self-calibration. The successful line-mapping observations using the Rainbow proved its imaging capabilities.

2. The CO (1–0) emission was found and unresolved at the radius $r \simeq 400$ pc from the continuum nucleus. The calculation of molecular mass (M_{H_2}) within the central $r < 400$ pc region is estimated about 4.5% of the mass derived from the published interferometric CO (1–0) image integrated over $65''$ region in the center. This is because 1) The narrow field of view that is determined by the 45 m primary beam size of $16''$ (FWHM) does not pick up the extended CO emission in nearly $30''$. 2) The synthesized beam size produced from the Rainbow full-track observation is $1''.7 \times 0''.8$. This finest beam size have resolved out the extended CO (1–0) structure seen in the previously obtained single-dish or interferometric images.

3. The lack of central CO peak emission in the CO map imaged by Inoue *et al.* (1996) is probably due to the continuum subtraction error. It is likely that they subtracted the CO emission at the nucleus with the continuum emission seen in the map center. The line-free velocity (frequency) channels available in their observations are insufficient to determine the average continuum baseline level. Actually, the equivalent CO (1–0) velocity width of NGC 1275 ranges nearly ~ 600 km s^{−1}, while the velocity coverage of the correlator which they used was only ~ 800 km s^{−1}. In the case of this thesis observation using UWBC, the continuum reception bandwidth is wide (~ 2500 km s^{−1}) enough for us to allow continuum subtraction with an accuracy of $\sim 2\%$.

4. Inoue et al. (1996) reported the detection of $2.1 \mu\text{m}$ hydrogen line emission at the nucleus using 3.0 m Infrared Telescope Facility and it was found spatially unresolved at $r = 350$ pc from the center. The linear dimension of H₂ peak emission nearly matches the unresolved size of CO peak emission at the nucleus. The massive stellar bar observed at H₂ $2.1 \mu\text{m}$ along the molecular bar in NGC 1068 is not seen NGC 1275 so far, but the HST observation discovered the young blue clusters in the central 8 kpc region

of NGC 1275 (Holtzman *et al.* 1992). This could be the presence of star formation along the molecular bar-like system.

5. The velocity structures obtained from Rainbow observations conflict with those in the published results, while the follow-up NMA-D observations are consistent with Rainbow results. The observed asymmetry in velocity shows that the red-shifted features are not completely detected, but only blue-shifted features are visible in the maps. This discrepancy can be explained as follows; The extended red-shifted features are resolved out with the small synthesized beam of the Rainbow, and therefore the only blue-shifted features, which are relatively intense and compact, remain unresolved in the maps.

6. The derived mean gas density (n_{H_2}) in the central CO peak is estimated only $\sim 300 \text{ cm}^{-3}$. If the central CO emission is the molecular torus, the gas interior to 400 pc must be clumpy or confined within a more compact region.

7. The observed *twin peaks* structure forming the ring-like orbit with the 1.2 kpc radius which is prominent in the published CO image and the CO central concentration seem to imply that the central CO emission could be the results of gas fueling process from the outer CO ring-like structure onto the nucleus. In addition, the detected molecular bar-like structure in the young stellar cluster optically identified between the *twin peaks* are similarly seen in NGC 1068.

8. I discovered the morphological similarities between the molecular gas structure of NGC 1275 and NGC 1068. These suggest that the circumnuclear molecular gas ($r < 1 \text{ kpc}$) surrounding its radio-loud nucleus is very similar to that of Seyfert galaxy containing radio-quiet nucleus. The circumnuclear regions of AGN on $100 \text{ pc} < r < 1 \text{ kpc}$ scales are fairly common each other observed regardless of the host galaxy type, either spiral or elliptical. The origin of the radio-activity can be produced from the inner most region – the central engine.

Table 4. Comparison of the mapping parameter between NMA and the Rainbow

	Rainbow	NMA-AB
Synthesized beam size ^a		
... uniform weight	$1''.7 \times 0''.8$	$2''.2 \times 1''.3$
... natural weight	$2''.2 \times 1''.1$	$2''.5 \times 1''.4$
rms noise (1σ)		
... uniform weight	28 mJy beam^{-1}	46 mJy beam^{-1}
... natural weight	13 mJy beam^{-1}	32 mJy beam^{-1}

^aBeam position angles of the Rainbow and NMA-AB are -73° and -78° , respectively

Table 5. Nature of molecular gas in circumnuclear region

Parameter	NGC 1068 ^a	NGC 1275 ^b
Distance	14 Mpc	70 Mpc
Radius of the nucleus (ring)	130 pc (1.5 kpc)	400 pc ^b (1.2 kpc ^c)
Velocity (v_{rot})	100 km s^{-1}	130 km s^{-1}
M_{H_2} (nucleus)	$\sim 10^8 M_\odot$ ^d	$1.4 \times 10^9 M_\odot$
(inner ring ^e)	$1.4 \times 10^9 M_\odot$	$3 \times 10^{10} M_\odot$ ^c
M_{dyn} (nucleus)	$3.0 \times 10^8 M_\odot$	$1.5 \times 10^9 M_\odot$
$n(\text{H}_2)$ ^f (nucleus)	$2 \times 10^4 \text{ cm}^{-3}$	$3 \times 10^2 \text{ cm}^{-3}$
$N(\text{H}_2)$ ^g (nucleus)	$5 \times 10^{22} \text{ cm}^{-2}$	$3 \times 10^{23} \text{ cm}^{-2}$

^a Helfer et al. (1993)

^b This thesis

^c Inoue et al. (1996)

^d Individual clouds within spiral arms, of which typical size is $\sim 500 \text{ pc}$

^e Interior to the spiral arms (NGC 1068) or ring-like orbit (NGC 1275)

^f mean number density per unit volume

^g column density

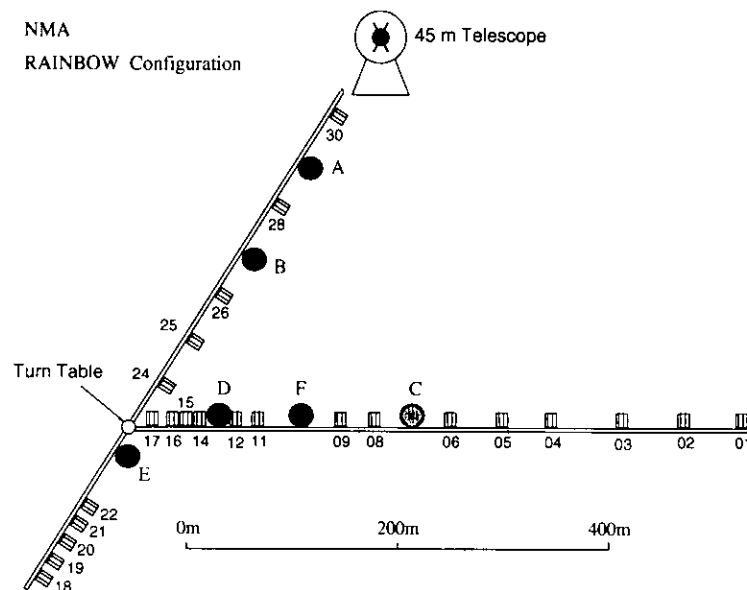


Fig. 3.— An overview of the NMA configuration in the Rainbow experiments. The positions of each 10 m telescope are denoted by filled circles. The C telescope did not work as the Rainbow Array at the time of the experiments.

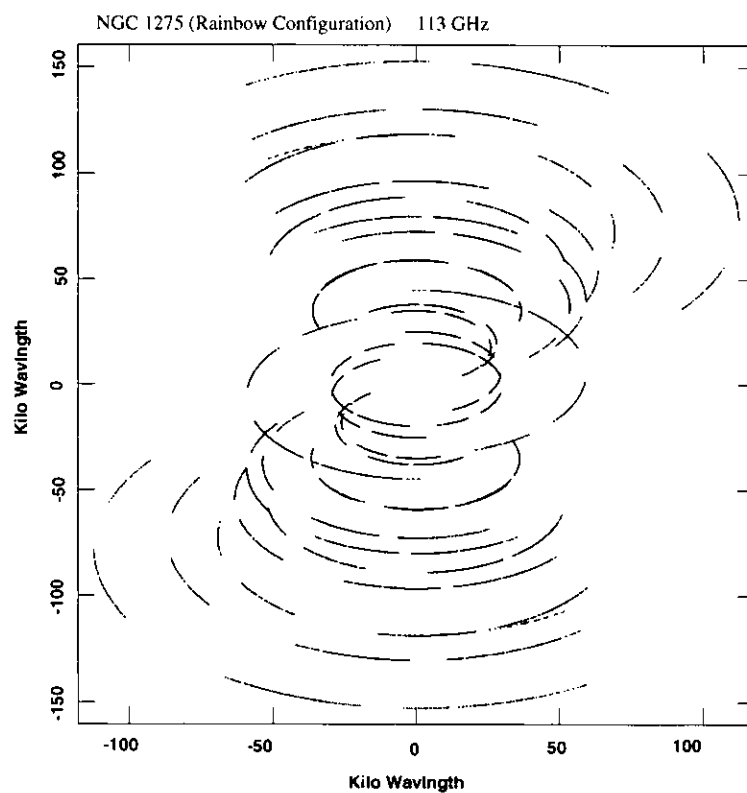


Fig. 4.— Full UV-plane coverage for 6 antennas, including the 45 m telescope. Plots are scaled in units of $k\lambda$.

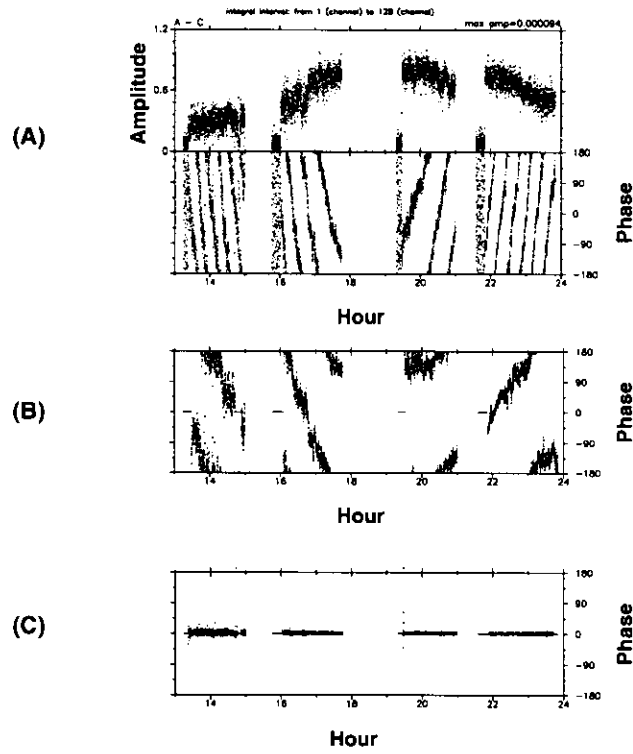


Fig. 5.— The fringe amplitudes and phases of NGC 1275 on the shortest 45 m – NMA 10 m baseline are shown as a function of time. (A) The measured fringe amplitude and phase (raw data; correlator outputs). (B) The fringe phase after removal of the effect of the 45 m focal point shift. (C) The fringe phase after self-calibration.

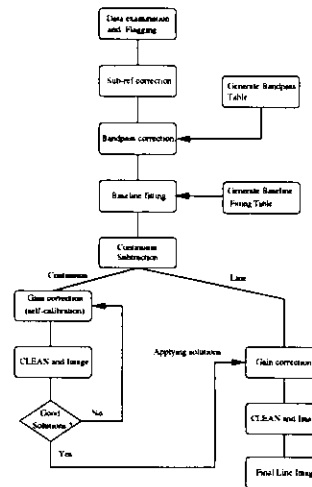


Fig. 6.— A schematic outline of the calibration procedure for CO in NGC 1275.

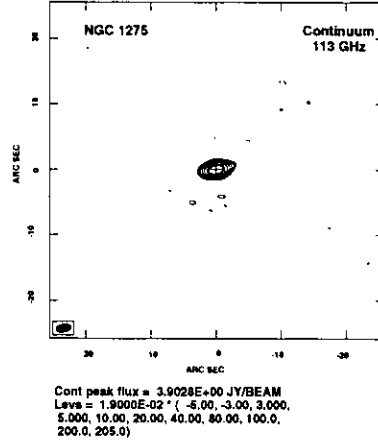


Fig. 7.— A Rainbow cleaned continuum image of NGC 1275 (3C 84) at 113.13 GHz. The continuum visibilities are made from the line emission-free frequency channels with the total bandwidth of about 600 MHz. The contour levels were -0.095, -0.057, 0.057, 0.095, 0.19, 0.38, 0.76, 1.5, 1.9, 3.8, and 3.9 Jy beam⁻¹. The peak flux density is 3.9 Jy beam⁻¹ and rms noise level is 19 mJy beam⁻¹. The contours are plotted clearly to show the dynamic range, of which 205. The synthesized beam (uniform weight) is plotted at the left bottom corner. The resulting spatial resolution is 1".7 × 0".8 and P.A. = -73.3°. The central cross mark denotes the continuum peak position.

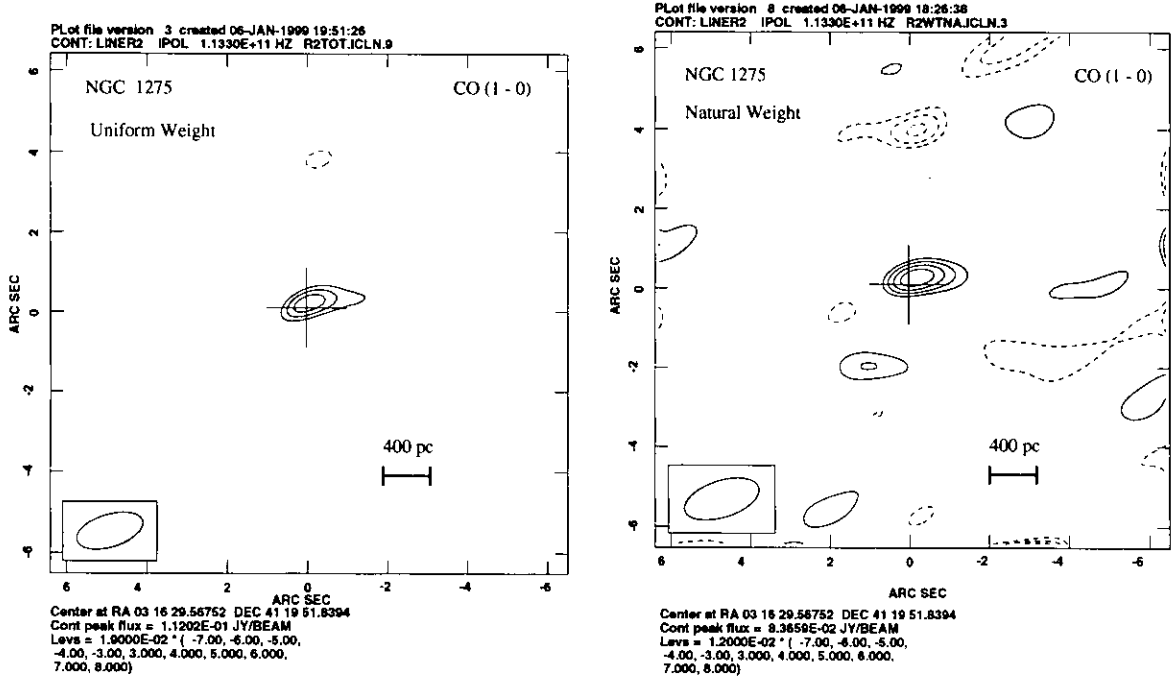


Fig. 8.— Velocity-integrated maps of NGC 1275, averaged from 5000 km s⁻¹ to 5310 km s⁻¹ (V_{LSR}). The field centers (continuum peak positions) are expressed by the crosses. Contour intervals are every 1 σ , plotted from the 3 σ rms noise level. Both of them are imaged using the Rainbow. left: uniformly weighted map with the peak flux is 112 mJy beam⁻¹, right: naturally weighted map with the peak flux is 83.7 mJy beam⁻¹. The synthesized beams are plotted at the left bottom corner of each map.

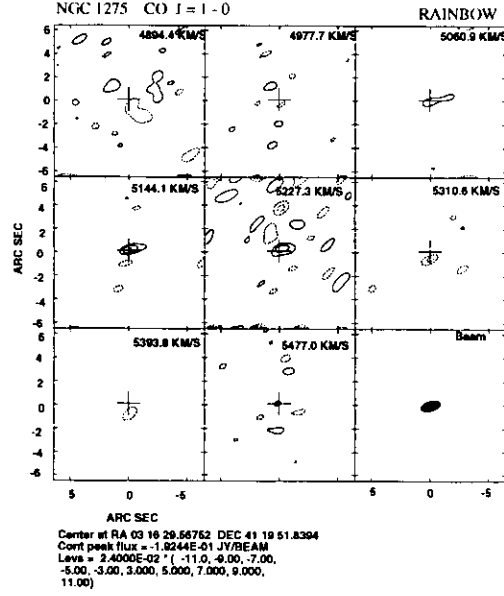


Fig. 9.— Velocity channel maps (uniform weight) with a velocity resolution of 83 km s^{-1} . The velocity covers from $V_{\text{LSR}} = 4855$ to 5515 km s^{-1} . The velocity on each panel shows the center velocity. The center position of the galaxy is marked by a cross in each panel. The synthesized beam ($1''.7 \times 0''.8$) is plotted at the bottom right panel.

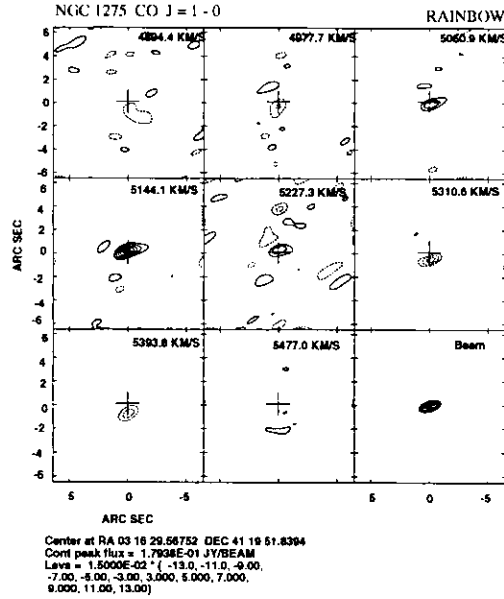


Fig. 10.— Velocity channel maps (natural weight) with the velocity resolution of 83 km s^{-1} . The velocity covers $V_{\text{LSR}} = 4855 - 5515 \text{ km s}^{-1}$. The synthesized beam ($2''.2 \times 1''.1$) is plotted at the bottom right panel.

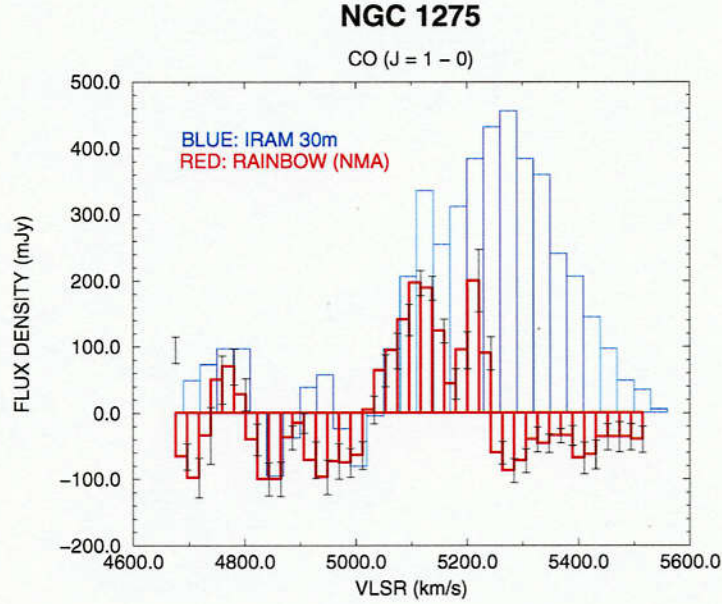


Fig. 11.— A CO ($J = 1 \rightarrow 0$) spectrum ($\Delta V = 20.8 \text{ km s}^{-1}$) obtained by the Rainbow (natural weight) with error bars (black), plotted together with the single-dish (IRAM 30 m) spectrum, smoothed to a velocity resolution of 30 km s^{-1} , reported by Lazareff *et al.* (1989). The systemic velocity of the galaxy is 5250 km s^{-1} .

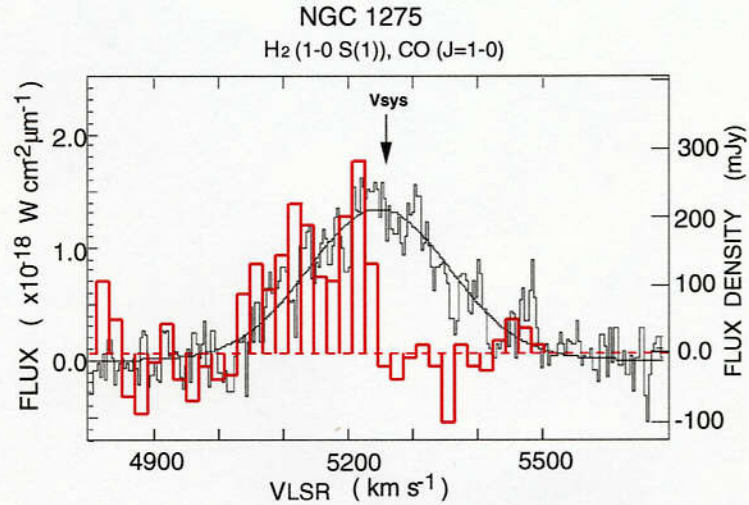


Fig. 12.— Spectrum of CO (1–0) (red line) with the Rainbow (uniform weight) overlaid with H₂ ($2 \mu\text{m}$) emission profile observed by Inoue *et al.* (1996). The velocity resolution is 20.8 and 30 km s^{-1} for CO (1–0) and H₂, respectively. The systemic velocity of NGC 1275 is marked by an arrow.

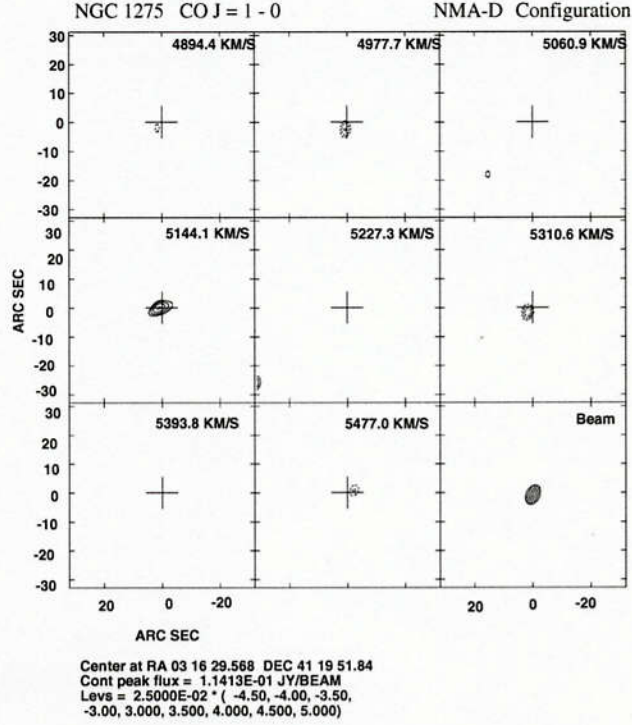


Fig. 13.— Velocity channel maps (natural weight) obtained with NMA in D configuration. The total velocity range is $V_{\text{LSR}} = 4855 - 5515 \text{ km s}^{-1}$. Each channel has the velocity width of about 83 km s^{-1} . The velocity on each panel shows the center velocity. The center position of the galaxy is marked by a cross in each panel. The synthesized beam is plotted at the bottom right corner.

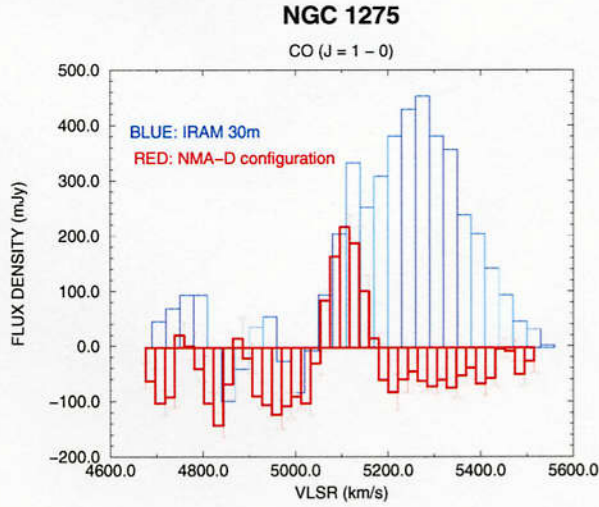


Fig. 14.— A $\text{CO } (J = 1 \rightarrow 0)$ spectrum ($\Delta V = 20.8 \text{ km s}^{-1}$) obtained by NMA in D configuration (natural weight) with error bars (dotted line), plotted together with the single-dish (IRAM 30 m) spectrum, smoothed to a velocity resolution of 30 km s^{-1} , reported by Lazareff *et al.* (1989). The systemic velocity of the galaxy is 5250 km s^{-1} .

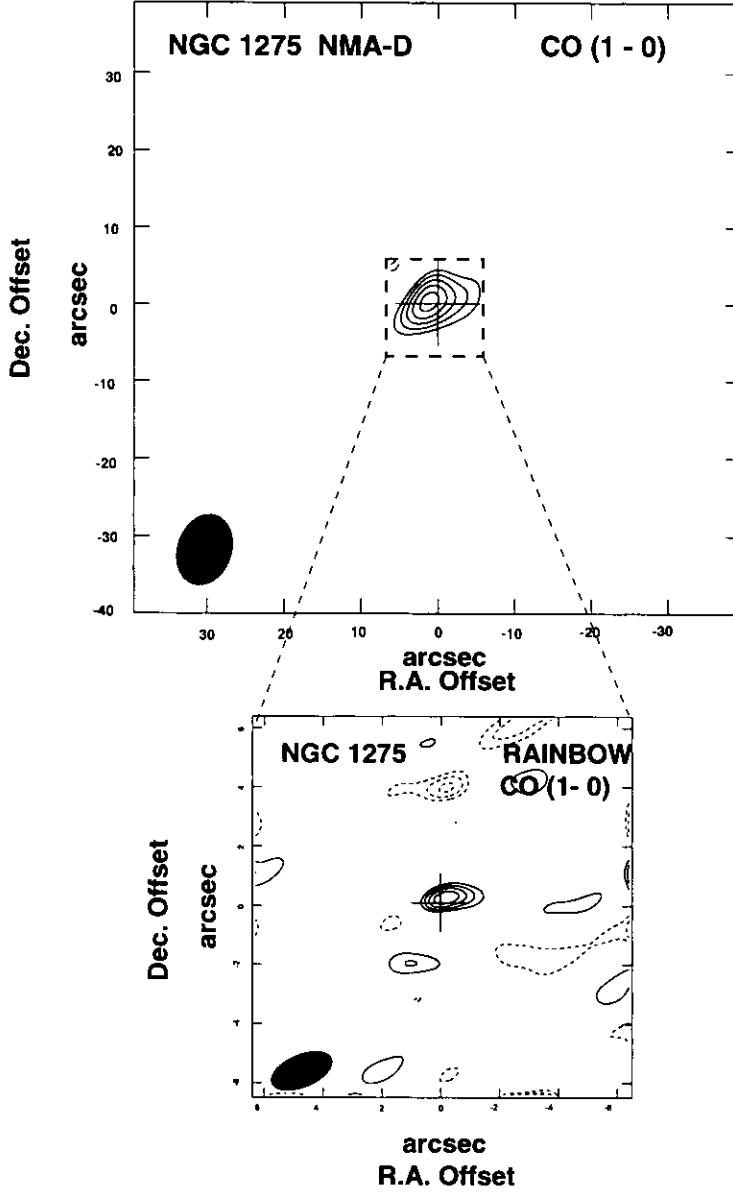


Fig. 15.— A velocity-integrated map (natural weight) with the NMA in D configuration, plotted with the high-resolution Rainbow velocity-integrated map (Contours are $3, 4, 5, 6, 7\sigma$ level. The sensitivity (1σ) is 12 mJy beam^{-1}). The integrated velocity range is $V_{\text{LSR}} = 5070 - 5190 \text{ km s}^{-1}$. The center position of the galaxy is marked by a cross. The synthesized beam ($8''.9 \times 5''.9$, P.A. = -20°) is plotted at the bottom left corner. The contour interval is a 1σ (17 mJy beam^{-1}), plotted from 3σ to 7σ .

Fig. 16.— The CO (1–0) emission contours superposed on the broad-band HST image obtained by Holtzman *et al.* (1992). The contour level starts from 52 mJy beam^{-1} with an interval of 20 mJy beam^{-1} for the *twin peaks* (Inoue *et al.* 1996), consist of red-shifted (thick red) and blue-shifted (thick blue) peak. *upper*: The *twin peaks* contours superposed on the bar-like CO emission (thick green) obtained from NMA-D. The contour level begins from $125 \text{ mJy beam}^{-1}$ with an 17 mJy beam^{-1} contour spacing. Each peak appears to be bridged by the extended CO 'bar'. *lower*: The *twin peaks* contours superposed on the CO peak emission obtained from Rainbow (thin black). The detected central CO emission is located between twin peak structure. The peak contour is 84 mJy beam^{-1} and the interval is 12 mJy beam^{-1} .

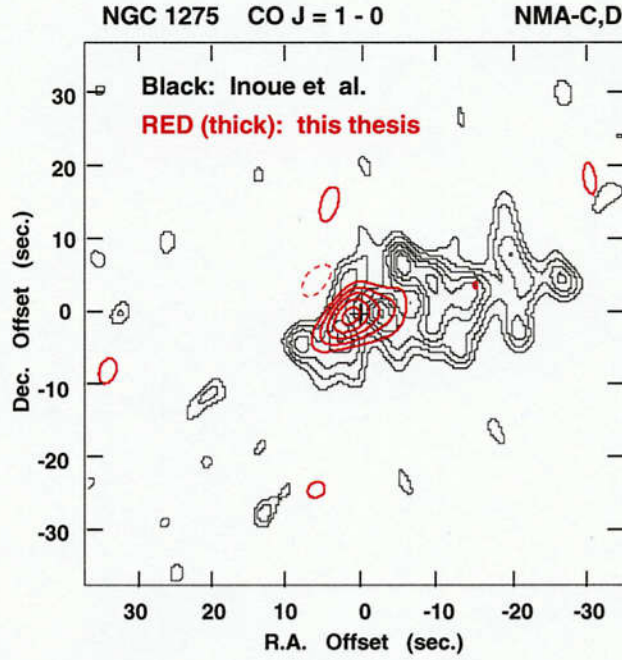


Fig. 17.— The obtained NMA-D CO velocity-integrated map (thick red) superposed on the map (thin black) observed by Inoue *et al.* (1996). The contour intervals are 20 mJy and 10 mJy in the NMA-D and their map, respectively. The lowest contour levels are 40 mJy and 20 mJy in the NMA-D and their map, respectively.

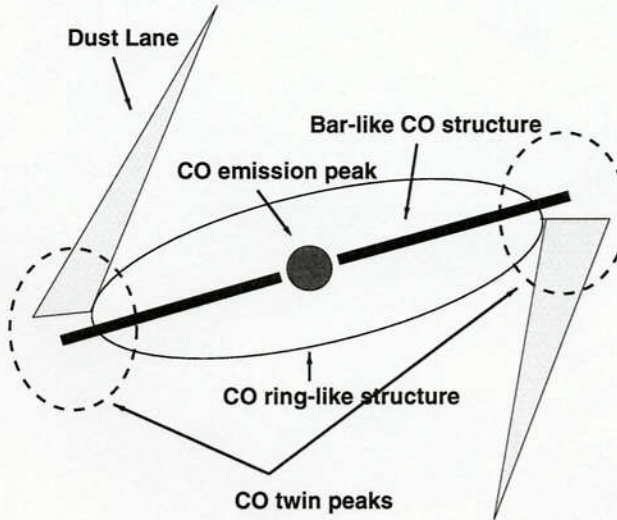


Fig. 18.— The model for the circumnuclear molecular gas structure in the inner 3 kpc region of NGC 1275. The dust lanes which are optically identified intersect the molecular ring at the CO *twin peaks*. The molecular gas in the ring-like orbit at $r=1.2$ kpc falls along the CO bar-like structure, and then flows into the nucleus in which CO is significantly concentrated within $r=400$ pc.

Chapter 4

WATER-VAPOUR MEGAMASER IN RADIO-ACTIVE GALAXY NGC 5793

The Host Galaxy

NGC 5793 is an edge-on spiral with dimensions of $3' \times 1'$ (de Vaucouleurs *et al.* 1976). HI and OH absorptions against a compact radio nucleus were found (Jenkins 1983, Whiteoak *et al.* 1987, Gardner *et al.* 1986). Both absorption lines obtained with VLA revealed plentiful absorbing material in front of the active nucleus, and the velocity ranges of the two absorption lines nearly coincide with each other (Gardner *et al.* 1986). The 21 cm continuum emission observed with the Gardner *et al.* (1992) showed that the radio nucleus consists of a bright continuum source with a diameter is about 16 – 80 milliarcsecond (mas), corresponding to 5 – 20 pc at a distance of 50 Mpc. The luminous and compact nucleus has a peak brightness temperature of 10^9 K, giving evidence for the existence of an AGN at the center. The galaxy which we selected comes from the IRAS Bright Galaxy Sample (Soifer 1987, Condon *et al.* 1990, Condon *et al.* 1991), which gives flux densities of Far-infrared and 21 cm radio continuum emission.

Summary of Observations

The radio synthesis observations presented in this Chapter were made using Very Large Array (VLA) and Very Long Baseline Array (VLBA), operated by National Radio Astronomy Observatory (NRAO), as well as single-dish telescope observations with the NRO 45-m and the Parkes 64-m radio telescope.

First, I present the detection of water vapour megamaser in NGC 5793 using the 45-m telescope. The properties of megamaser in this galaxy, attempted to be imaged with VLA in A configuration, have been studied with single-dish telescopes and its study extends a detailed, VLBI observations up to now. The VLBA observations of maser is then presented. The sub-parsec scale OH absorption and continuum structures at L- and C-Band in the nucleus of NGC 5793 are studied in next Chapter. Observation summary is shown in Table 1.

Detection of a Water-Vapor Megamaser

Introduction

Water-vapor megamasers, which have been found in the central regions of galaxies, are as much as 10^6 times more luminous than the masers found in galactic star-forming regions. These megamasers have been found in the nuclei of galaxies which have some level of nuclear activity. Although almost all of the megamasers exist in the Seyfert 2 galaxies or the LINERs, no H_2O masers have been detected in galaxies definitely classified as Seyfert 1's. Also, no megamasers have been found in normal galaxies (e.g., Braatz *et al.* 1994). These results suggest that megamasers are related to the nuclear activity of their host galaxies and to the classification scheme of Seyfert galaxies. Much of the emphasis in recent research on active galactic nuclei (AGNs) has been put in the area of unified models (Antonucci and Barvainis 1990). These models try to explain the observational differences between broad and narrow optical emission-line active galaxies by obscurity due mainly to a molecular disk around the central black hole and viewing-angle effects, rather than intrinsic physical properties. In these models, a Type2 Seyfert galaxy is nearly edge-on to our line of sight, and its broad-line region is shielded, being confined within an optically thick molecular disk or torus. If this disk contains dense molecular gas ($\sim 10^{10}\text{cm}^{-3}$) including H_2O molecules, and is strongly illuminated by the continuum background, the molecules could be amplified and maser emission would be observed. This could explain why H_2O megamasers have been found in Type2 Seyfert galaxies or LINERs which have an edge-on molecular disk.

Recent VLBI observations tell us that megamaser emission is a useful tool for studying the nuclear structure and dynamics within the sub-parsec region from the center of AGNs. For example, VLBA observations of the H_2O megamaser in NGC 4258 have revealed evidence of a massive black hole and a molecular disk rotating around it (Miyoshi *et al.* 1995). We report here on the first detection of H_2O megamaser emission from NGC 5793 and discuss the structure of the H_2O masing region. The parameters of the galaxy are listed in Table 3.

NRO 45 m Observations

Observations of the $6_{16}-5_{23}$ transition of water-vapour emission at a rest frequency of 22.23508 GHz were made with the 45-m telescope at the Nobeyama Radio Observatory on 1996 January 29, February 25, and March 4. The telescope beam (HPBW = $74''$) was pointed toward the nucleus of the galaxy. The position-switching mode with the reference position offset by $6''$ from the galaxy center was used. The telescope pointing was checked by observing a SiO maser star, R Hya; and its accuracy was estimated to be better than $10''$. We used a K-band cooled HEMT amplifier as a front-end receiver equipped with a linear polarization feed. The system noise temperature, including atmospheric effects and the antenna ohmic loss, was 170 – 260 K, depending on the weather conditions. The receiver back-ends were 2048-channel high-resolution acousto-optical spectrometers (AOSs). Each AOS provides a total bandwidth of 40 MHz, corresponding to 540 km s^{-1} with a velocity resolution of 0.50 km s^{-1} . We used a series of seven AOSs, each overlapping by 5 MHz, resulting in a total velocity range of $V_{\text{LSR}} = 1750 - 4710\text{ km s}^{-1}$. The calibration of the line intensity was performed by chopping the sky and a reference load at room temperature. The flux density of H_2O maser emission was calculated from the measured antenna temperature, T_A^* , and the telescope sensitivity, S/T_A^* , $2.76 \pm 0.22\text{ Jy}$.

Results of 45-m OBSERVATIONS

Figure 1 shows the H_2O maser spectra of NGC 5793 at three different epochs in the velocity range of $V_{\text{LSR}} = 2800 - 4200 \text{ km s}^{-1}$ in the radiodefinition. The variability of the maser emission over a period of about 60 days is clearly seen. Figure 2a presents the spectrum obtained by averaging the spectra over the three observations shown in Figure 1. Two distinct maser emission lines were found, at $V_{\text{LSR}} = 3190$ and 3677 km s^{-1} . The 3190 km s^{-1} feature is blue-shifted by 252 km s^{-1} with respect to the systemic velocity, $V_{\text{sys}} = 3442 \text{ km s}^{-1}$, with a peak flux density of $S_{\text{peak}} = 0.24 \text{ Jy}$ and a width of $\Delta V = 14.0 \text{ km s}^{-1}$. The 3677 km s^{-1} feature is red-shifted by 235 km s^{-1} for V_{sys} with $S_{\text{peak}} = 0.54 \text{ Jy}$ and $\Delta V = 1.3 \text{ km s}^{-1}$. The flux density of this feature was $S_{\text{peak}} = 0.54 \text{ Jy}$ on January 29, but decreased to $S_{\text{peak}} = 0.26 \text{ Jy}$ on February 25, and became invisible on March 4. The strength of the 3190 km s^{-1} feature, however, was not as variable as that of the 3677 km s^{-1} feature throughout the observing period. The apparent isotropic luminosities of the blue- and red-shifted features on January 29 were $L = 81 \pm 4 L_{\odot}$ and $44 \pm 4 L_{\odot}$, respectively, and the total luminosity was $125 \pm 8 L_{\odot}$. In addition to these strong high-velocity features, weaker emission around V_{sys} was found at $V_{\text{LSR}} = 3449 \text{ km s}^{-1}$ and 3519 km s^{-1} , which were three times the rms noise level (Figure 2b). These had peak flux densities of 25 ± 8 and $28 \pm 8 \text{ mJy}$, respectively. The total luminosity of all features derived from Figure 2b is more than $230 L_{\odot}$. Detailed spectral properties of the H_2O emission lines are listed in Table 3.

Discussion

We will consider the origin of the symmetric H_2O emission and a model for explaining how the maser emission arises from the galaxy center in terms of the geometry of a circumnuclear disk. The velocity range of the H_2O maser emission encompasses that of the CO ($J = 1 \rightarrow 0$) emission ($V_{\text{LSR}} = 3305 - 3661 \text{ km s}^{-1}$) obtained by recent observations with the Nobeyama Millimeter Array (Hagiwara and Kawabe, in preparation, see Figure 2a). Therefore, since the distribution of CO, which extends up to 0.8 kpc from the center, reveals the distribution of gas in the galactic disk, the inner H_2O masing region seems to be rotating faster than the outer CO gas disk. The H_2O maser emission shows two distinct high-velocity features which are symmetrically red- and blue-shifted by about $\pm 245 \text{ km s}^{-1}$ with respect to the systemic velocity of the galaxy, V_{sys} , and weak broad features nearby V_{sys} . The velocity range of the latter systemic features nearly coincide with those of the HI and OH absorption spectra (Figure 2b) obtained by a previous observation with VLA (Gardner *et al.* 1986) and by other observations (e.g., Jenkins 1983). The peak velocities of the systemic features at $V_{\text{LSR}} = 3449 \text{ km s}^{-1}$ and 3519 km s^{-1} are close to those of the HI and OH absorptions, while no absorption is seen at the velocities of the high-velocity features (Figure 2b). VLBI observations have revealed that the HI absorption is seen against the bright compact nucleus of the galaxy (Gardner *et al.* 1992). These results indicate that both HI and OH absorbing clouds and the masing region responsible for the systemic features are located in front of the central continuum source, which would amplify HI and OH clouds toward our line of sight, while the high-velocity features of H_2O maser arise off the direction of the central continuum source.

In order to explain the H_2O emission, we propose a model in which high-velocity features symmetrically offset from V_{sys} originate from the rotating disk or torus around the nucleus of the galaxy. This geometrical interpretation is derived by analogy with NGC 4258 (Watson and Wallin 1994, Miyoshi *et al.* 1995, Greenhill *et al.* 1995). The H_2O maser emission in NGC 4258 consists of features around the systemic velocity and high-velocity features that are quite symmetrically offset from V_{sys} (Nakai *et al.* 1993, Nakai *et al.* 1995a). These maser features are emitted from a circumnuclear disk showing a Keplerian rotation;

the systemic features arise from the inner edge of the disk in the line of sight toward the nucleus, and high-velocity features from the tangential points of the disk (Miyoshi *et al.* 1995). The similarity of the maser features between the two galaxies gives the geometrical model shown in figure 3. In the model the systemic and high-velocity features originate from a circumnuclear disk or 0.016'' torus with the rotational velocity, $v_{\text{rot}} = v_{\text{rot}}^* / \sin i = 245 \text{ km s}^{-1} / \sin i$, (where $v_{\text{rot}}^* = |V_{\text{LSR}} - V_{\text{sys}}|$, i.e., the line of sight velocity of v_{rot} and i is the inclination angle of the galaxy), which is determined by the velocity offsets of the high-velocity features with respect to the systemic velocity. Masers in the systemic velocity group are amplified in the line of sight toward the central continuum source. The upper limit of the diameter of the radio continuum nucleus can be inferred from the published VLBI image of Gardner *et al.* (1992). The VLBI core has an angular size of 16 mas, equivalent to a linear size of $\sim 4 \text{ pc}$ at a distance of 50 Mpc. Alternatively, adopting the 1% level of the peak flux density, the distribution of the 21 cm continuum emission extends to 80 mas, or 20 pc in linear size. Thus the diameter of the maser disk surrounding the nuclear region can be estimated to be at least larger than 4 – 20 pc. The lower limit of the diameter of the disk or torus would be one to two orders of magnitude greater than that of NGC 4258 ($\sim 0.26 \text{ pc}$; Miyoshi *et al.* 1995). We can estimate the mass confined within the lower limit of the inner radius of the disk or torus, based on our model. Adopting an inner radius of $r = 10 \text{ pc}$, and a rotation velocity of $v_{\text{rot}} = v_{\text{rot}}^* / \sin i$ ($i = 73^\circ$; Roth (1994)), the lower limit of the nuclear mass confined within the gas disk is

$$1.5 \times 10^8 \left(\frac{r}{10 \text{ pc}} \right) \left(\frac{v_{\text{rot}}^*}{245 \text{ km s}^{-1}} \right)^2 \left(\frac{0.956}{\sin i} \right)^2 M_{\odot}, \quad (4.1)$$

where we assumed the inclination angle of the maser disk, i , to be equivalent to that of the galactic disk. The calculated mass is more than four-times larger than that of NGC 4258, $3.7 \times 10^7 M_{\odot}$ (Miyoshi *et al.* 1995). Thus, the physical parameters of the nuclear region of NGC 5793 proved to be quite different from those of NGC 4258. The intensity of the systemic features is also much different between the two galaxies. The relatively weaker systemic features and intense high-velocity features in NGC 5793 have an opposite relationship to those of the maser features in NGC 4258. This may be because the inclination of the inner maser disk of NGC 5793 is smaller than that which we estimated from the outer galactic disk. The inclination angle of a molecular gas disk or torus in the nuclear region does not always coincide with that of the galactic disk. Therefore, only a small part of the inner edge of the disk, whose inclination is less than 73° , would be amplified by the continuum radiation, which results in the weaker systemic features and the strong high-velocity features in NGC 5793. A further investigation to confirm the systemic features should be carried out.

Moreover, we need VLBI observations to establish the validity of the model discussed above. Because the disk diameter of 20 pc corresponds to an angular size of 80 mas at a distance of 50 Mpc, it would be easy to determine the relative position of each maser feature, especially of the high-velocity features with respect to the systemic features.

CO (1–0) Distribution in NGC 5793

NMA Results

I could detect significant CO ($J = 1 \rightarrow 0$) emission toward the center of NGC 5793 for the first time using NMA. In Figure 4, the velocity channel maps at 3 arcsec. resolution (750 pc) are shown. The velocity resolution is 65 km s^{-1} . The velocity range in which CO ($J = 1 \rightarrow 0$) emission is significantly detected is

Table 1. Observation summary of NGC 5793

Telescope	Observing Date	Obs. Band	Line transition	Observing Time (hrs)	Comments
NRO 45-m ^a	Jan. 29 1996	K	H ₂ O	5	
NMA	Mar. 8,9 1996	2.6 mm	CO (1–0)	12	C config.
VLBA	Sep. 16 1996	K	H ₂ O	8	Failed
VLBA	Nov. 30 1996	L	OH (1665 /1667 MHz)	8	
VLA	Jan. 10 1997	K	H ₂ O	8	
VLBA	Mar. 2 1997	K	H ₂ O	8	No detection
Parkes 64-m	Aug. 18 1997	K	H ₂ O	16	
VLBA	Oct. 12 1997	C	Continuum	8	
VLBA	May 10 1998	K	H ₂ O	8	phase- reference

^aThe spectra have been actually monitoring.

Table 2: Parameters of NGC 5793

R.A.(1950) ¹⁾	14 ^h 56 ^m 37. ^s 0
Decl.(1950) ¹⁾	–16°29′04.9″0
Distance ²⁾	50 Mpc
Morphological type ³⁾	Sb
Magnitude (<i>V</i>) ⁴⁾	13.3 (mag)
Inclination angle ⁵⁾	73°
<i>V</i> _{sys} (LSR) ⁶⁾	3442 ± 72 km s ^{–1}
Flux density ^{7), 8)}	1.05 Jy at 1.404 GHz
	0.51 Jy at 4.860 GHz
	0.15 Jy at 14.940 GHz
	0.45 Jy at 25 μm
	6.36 Jy at 60 μm
	8.65 Jy at 100 μm
Spectral index ⁶⁾	0.59 (80 MHz – 1500 MHz)

1) Whiteoak *et al.* 1987

2) Assuming $H_0 = 75 \text{ km s}^{-1} \text{ Mpc}^{-1}$.

3) de Vaucouleurs *et al.* 1976

4) Longo and de Vaucouleurs 1989

5) Roth 1994

6) Palumbo *et al.* 1983 (Converted to LSR radio definition.)

7) Adopted from Whiteoak, Gardner (1987).

8) From IRAS Point Source Catalog (1985)

Fig. 1.— H_2O maser spectra of NGC 5793 measured with the NRO 45 m telescope, observed on 1996 January 29, February 26, and March 4. The arrow denotes the systemic velocity of the galaxy.

Fig. 2.— (a) Averaged maser spectrum of NGC 5793 over three sessions, from 1996 January 29 to March 4. An arrow at the bottom denotes the velocity range of CO ($J = 1 \rightarrow 0$) emission. (b) A comparison of HI (unbroken line) and OH (1667 MHz, dashed line) line with maser spectrum.

Fig. 3.— A cartoon of the geometry for the H₂O maser emission in the nuclear region of NGC 5793

Table 3: Monitoring results of H₂O megamaser emissions in NGC 5793.

parameters	red-shifted	systemic 1	systemic 2	blue-shifted
Velocity center* (km s ⁻¹)	3677	3519	3449	3190
Velocity width† (km s ⁻¹)	1.3	48	45	14
Peak flux density (mJy)				
January 29	540 ± 47			240 ± 47
February 25	260 ± 55			260 ± 61
March 4	< 182			210 ± 41
Averaged‡	55 ± 8	28 ± 8	25 ± 8	99 ± 8
Luminosity (L _⊙)				
January 29	44 ± 4			81 ± 4
February 25	20 ± 4			76 ± 11
March 4	< 20			56 ± 8
Averaged ‡	33 ± 3	51 ± 4	49 ± 4	80 ± 4

*Velocities are written in LSR definition. To convert to heliocentric velocities 8 km s⁻¹ should be added to LSR velocities.

†Velocity widths of systemic features are derived from the averaged spectrum shown in Figure 2b.

‡ Values are derived from figure 2b.

$V_{\text{LSR}} = 3190 - 3634 \text{ km s}^{-1}$. The compact CO emission is seen in maps with the radius of about 5'' (1.2 kpc) from the field center. From the velocity channel maps, there are position shifts of CO emission peak in each velocity channel seen in the NW – SE direction (P.A. $\simeq 40^\circ$). This is nearly consistent with the major axis of the galaxy’s disk in larger scale. The derived parameters by NMA observations are listed in Table 4.

Table 4. Parameters derived from CO (1–0) observations with NMA

Derived papameters	
CO radius	1.2 kpc
Line width	445 km s ⁻¹
M_{H_2}	$7.9 \times 10^9 M_\odot$
M_{dyn}	$3.7 \times 10^9 M_\odot$

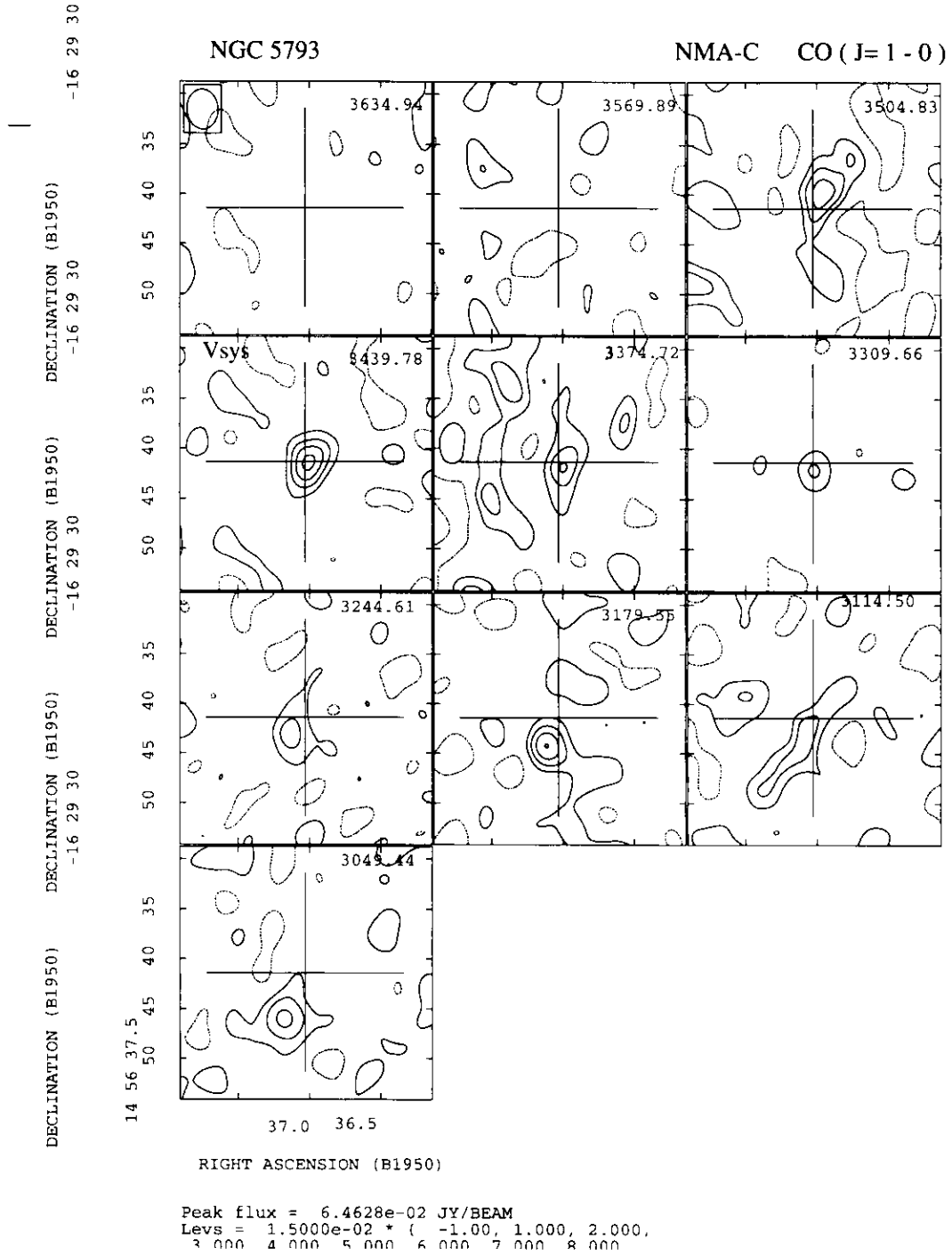


Fig. 4.— Velocity channel maps of CO ($J = 1 \rightarrow 0$) emission in the nuclear region of NGC 5793 with NMA-C. Center positions are marked by crosses. A synthesized beam is displayed at the upper-left corner. A factor of 2.2 has to be multiplied to the written contour scales to measure real flux densities.

High-Resolution Study of Water-Vapor Maser

VLA Observations

Observations and Results

Observations of the maser emission with the VLA-A were made in 1997 January for 6 hours with 27 antennas. The sources were observed alternating frequency, centered on 21.948, 21.965, 21.982, and 22.001 GHz, respectively, every 90 minutes, in order to cover four detected maser features with a 6.25 MHz bandwidth. The resultant effective velocity resolution using 64 spectral channels was 1.32 km s^{-1} and velocity coverage was 85 km s^{-1} . A bright radio source of 1507-168 was observed for both gain and phase calibrations, while 3C 268 was used to calibrate the bandpass shape of the NGC 5793 data and to scale the absolute flux density of the maser.

The continuum data was obtained by averaging the line-free channels. Phase corrections derived from the continuum data were obtained using self-calibration procedure and the resulting phase corrections were then applied to the line data. Continuum emission superimposed on the maser line emission was subtracted in the UV plane. The line spectra and CLEANed images were then made from these calibrated data with a synthesized beam of $0.13'' \times 0.08''$. The only $V_{\text{LSR}} = 3190 \text{ km s}^{-1}$ feature was detected with a peak flux density of $64.9 \pm 4.0 \text{ mJy beam}^{-1}$, while other velocity features were not detected at all. It is likely that these features became weaker below the detection limit of . The detected maser spectrum over $V_{\text{LSR}} = 3160 - 3230 \text{ km s}^{-1}$ and unresolved continuum image are shown in Figure 5. The continuum map has a thermal noise of about $0.135 \text{ mJy beam}^{-1}$.

The continuum is not resolved by the $130 \times 80 \text{ mas}$ beam, implying that the radio continuum source has a structure that is less than $\sim 30 \text{ pc}$. The position of blue-shifted maser emission, obtained by integrating the line emission range from $V_{\text{LSR}} = 3190 - 3220 \text{ km s}^{-1}$, coincides with that of continuum peak within 10 mas.

The summary of the VLA observations is the following.

- The systemic and red-shifted features were not detected. It is likely that maser emission has become quiet after the first discovery on January 29 in 1996.
- Only a blue-shifted feature was detected. The feature seems to contain at least three velocity components.
- The position between the blue-shifted maser spot and K-band continuum source is consistent within 10 mas, or 3 pc.

Further VLBI investigations on milliarcsecond scale resolution should be conducted in order to search distribution of maser spots and continuum emission.

VLBA Observations

Observations

Observations were performed in three sessions during 1996 – 1998 (see Table 1). In each epoch, the VLA was phased to VLBA to improve sensitivity. In the first two epochs, due to relatively poor baseline sensitivity of $\sim 10 \text{ mJy}$, neither any continuum nor maser emission was detected. The peak flux density

of maser features is becoming weak, < 100 mJy in single-dish observations, while the maser intensity in the galaxy has a trend of decreasing since the first discovery on 1996 December (Hagiwara *et al.* 1997). To detect maser features with VLBA, special care for observations was required. On the third epoch on 1998 May 10, a phase-referencing mode observation was employed at K-band. In order to detect both weak continuum and maser emission expected for K-band, phase-referencing was carried out to the nearby compact radio source PKS 1504-166, whose position (α ; 15 07 04.7869, δ ; -16 52 30.267; J(2000) (Moellenbrock *et al.* 1996)) is accurately determined within 2 degrees of NGC 5793. The rms noise in final images is expected to be ~ 0.1 mJy beam $^{-1}$.

In the third session, four 8 MHz IF bands were employed; two of which were dedicated to observing blue- and red-shifted features centered on $V_{\text{LSR}} = 3190$ and 3677 km s $^{-1}$, respectively and the remained bands were positioned to the centroids of systemic features of $V_{\text{LSR}} = 3449$ and 3519 km s $^{-1}$. The observations of bandpass and phase calibrators of 4C 39.25 were interleaved during the session in addition to the phase-referencing observations. The resultant total on-source time was about 4 hours. The continuum image was produced from the single channel centered on $V_{\text{LSR}} = 3677$ km s $^{-1}$ that is devoid of maser line.

Results and Discussion

The cross-correlation maser spectrum (blue-shifted feature) taken with the VLA-Pietown baseline is plotted in Figure 6. The peak flux density is 37 ± 2 mJy and the rms noise level is ~ 5 mJy. Each velocity channel is integrated over 500 kHz (6.7 km s $^{-1}$) wide to obtain spectral sensitivity. The spectra of maser emission is seen between shortest baselines. The calibration of flux density is accurate to about 5%. Figure 7 shows continuum emission image at 22 GHz obtained from the single IF channel devoid of maser emission with rms noise level of 1.5 mJy beam $^{-1}$. The continuum emission is detected with a peak flux density of 9.0 mJy above 5σ detection limit and its peak position roughly coincides with those at lower frequencies. The velocity-channel maps ($\Delta V = 13.4$ km s $^{-1}$) are shown in Figure 8, where maser emission is seen split into two parts with the peak flux density of 24 mJy beam $^{-1}$. The rms noise in channel maps is about 4.3 mJy beam $^{-1}$.

The measured position of the brightest maser spot (α ; 14 59 24.76085, δ ; -16 41 36.2667; J(2000)) is offset from the position of 22 GHz continuum emission peak (α ; 14 59 24.76154, δ ; -16 41 36.2543; J(2000)) by 13 mas ($\Delta\text{RA} = 7$ mas, $\Delta\text{Dec} = 12$ mas), or 3 pc. The relative position error between the maser and continuum is quite small, depending mainly on the residual phase slope due to any error we made in estimating the group delay and the error in the absolute position of the calibrator source. These will be second order effects and will be of the order of hundreds of micro-arcseconds. In this case, the position errors would be much smaller since we applied the same calibration to both emission. The obtained H₂O maser emission is unambiguously associated with central continuum source (C1(C)) at 1.6 and 5 GHz source (see Figure 9). The distribution of maser spots linearly elongated almost north-east direction, at a position angle of 40°, that is consistent with 1.6, 5.0 and, 22 GHz continuum emission. The emission subtends 3.6 mas (0.83 pc) or about three beamwidths, assuming that the fainter north-west spot is real.

The masers in NGC 5793 is very similar to those in NGC 1052 and NGC 1068 in that velocities of masers are offset from the systemic velocity of the galaxy and maser spots are displaced from the nucleus and coincident with radio continuum component (Gallimore *et al.* 1996a, Claussen *et al.* 1998). Based on the past and present observations, the simplest explanations for maser spots are broken down as follows.

- The water maser spots lie in a rotating molecular disk around the nucleus of NGC 5793. Taking the distance to the brightest maser spot from the continuum peak (C1(C)) to be a radius of rotation,

the gravitationally bounded mass within the radius will be $4.5 \times 10^7 M_{\odot}$. This is as much as the enclosed mass derived from NGC 4258 (Miyoshi *et al.* 1995). Theoretically these masers are in the Keplerian part of the velocity curve. It is noteworthy that we, here, supposed that a central engine or possibly a black hole exists, in the the continuum peak (C1(C)).

- The maser spots superposed on the continuum emission could arise from a dense molecular cloud or disk foreground to the jet. The maser amplifies the background radio continuum, as is not the case with results of NGC 4258. Similarly, it is likely that the masers lie in dense molecular gas in the jet.

If we assume that the 'true' core of the galaxy lie in nearby the component C4, the kinematical interpretation of maser emission would be even more complicated. In order to study the velocity gradients and relative positions of systemic and red-shifted features detected by the 45m, further VLBA observations and single-dish monitoring of maser to find the opportunity of observation will be crucial.

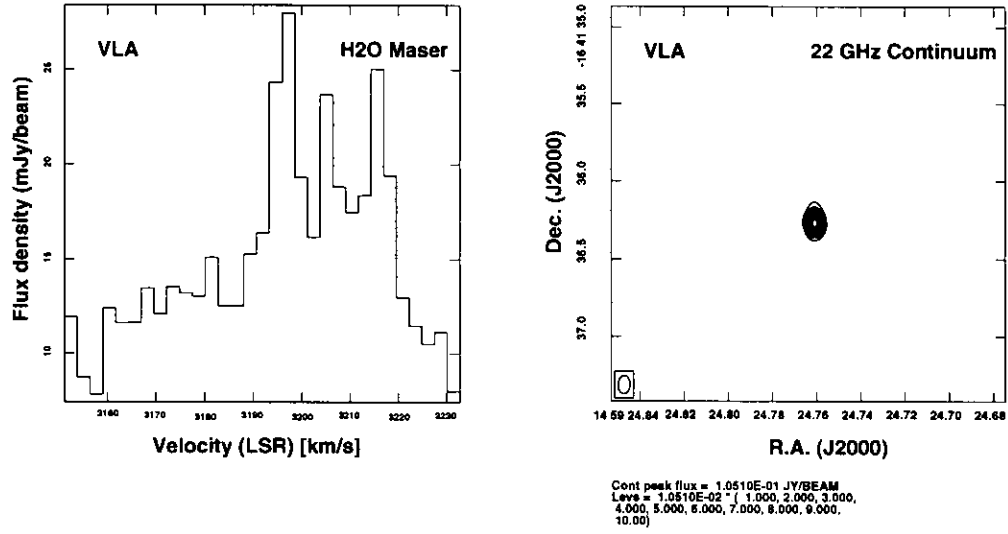


Fig. 5.— *left*: A VLA-A spectrum of water maser emission. Velocities are written in LSR. *right*: A VLA-A continuum map at 22 GHz.

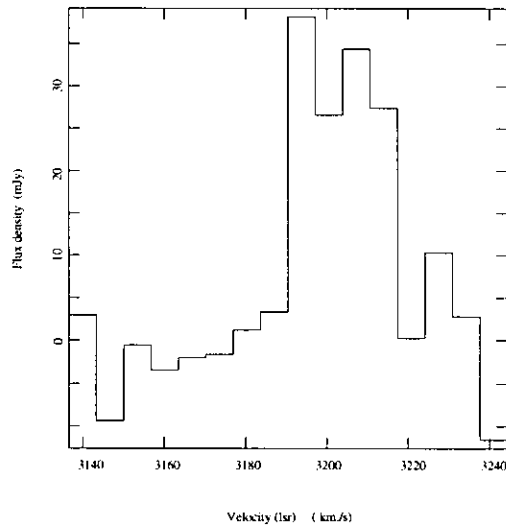


Fig. 6.— A H₂O maser spectrum of the blue-shifted feature, obtained with VLBA on 1998 May 10 in the VLA-PT baseline.

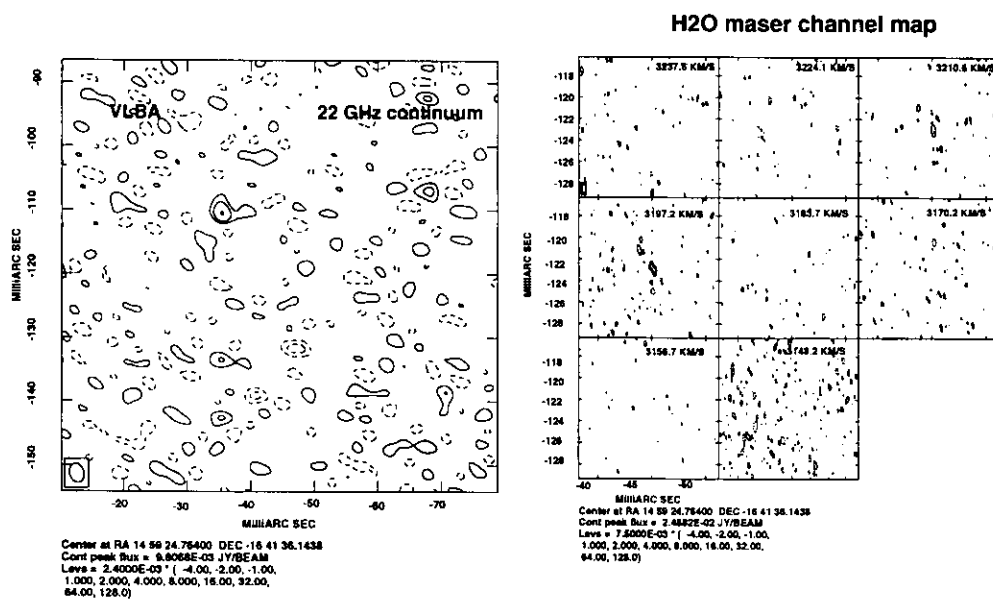


Fig. 7.— A 22 GHz continuum image obtained with VLBA.

Fig. 8.— Velocity channel maps of NGC 5793. The maser feature is seen around at 3197.2 km s^{-1} . (The position of the images wrt the L and C-band images are uncertain.)

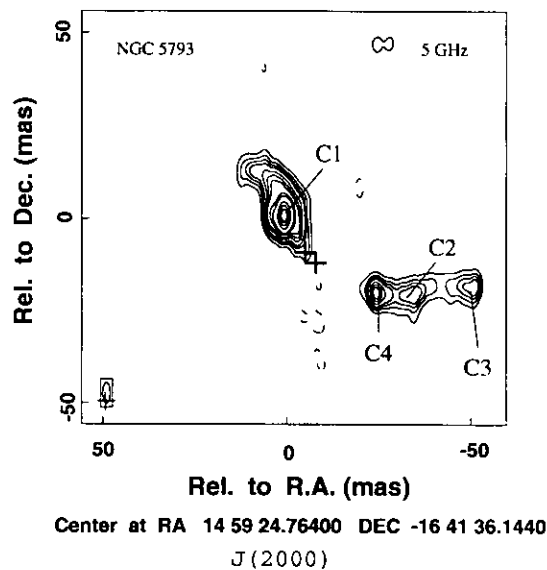


Fig. 9.— A 5 GHz continuum image of the nuclear region of NGC 5793. The two crosses mark the positions of two separate maser spots.

Chapter 5

HIGH-RESOLUTION OH ABSORPTION STUDY OF NGC 5793

Introduction

The discovery and sub-parsec scale studies of H₂O maser emission toward the nuclei of several galaxies have greatly improved our understanding of the circumnuclear regions of active galactic nuclei (AGN). Intense interferometric studies of the maser in the Seyfert/LINER galaxy NGC 4258 mainly using VLBI provided a detailed description of a rotating circumnuclear disk in Keplerian motion with a radius of 0.13 pc, bound by a super massive black hole with a mass of $3.7 \cdot 10^7 M_{\odot}$ (Miyoshi *et al.* 1995; Greenhill *et al.* 1995; Nakai *et al.* 1993). Similar H₂O masing disks as those found in NGC 4258 have been identified in other AGN: NGC 1068 (Greenhill *et al.* 1996), NGC 3079 (; Satoh *et al.* 1998) and NGC 4945 (Greenhill *et al.* 1997). These results imply that a sub-parsec or parsec-scale molecular disk/torus surrounding the nucleus is common to some narrow-line AGN and that their existence agrees well with the scheme which describes the unification of different types of AGN, originally proposed by Antonucci (1993).

VLBI observation of nuclear absorption lines is another method of studying kinematics of the innermost region of circumnuclear gas. Gallimore *et al.* (1996a) found that the spectral profile and location of the HI absorption on 100 pc scales in NGC 1068 are consistent with those of H₂O masers which are seen around the nucleus and 30 pc further out along the jet. VLBI observations of NGC 1068 with sub-milliarcsecond angular resolution showed that nuclear H₂O masers are distributed with a radius of 0.65 pc showing sub-Keplerian rotation (Greenhill *et al.* 1996). These observational facts strongly suggest that the structure and kinematics of the circumnuclear gas might be traced by absorption-lines as well as water masers.

NGC 5793 is an edge-on disk galaxy with a bright compact nucleus in radio continuum emission. Baan *et al.* (1998) classified the optical emission of NGC 5793 as being Seyfert type 2, which implies AGN activity. The galaxy lies at a distance of 46 Mpc and assuming $H_0 = 75 \text{ km s}^{-1} \text{ Mpc}^{-1}$, 1 milliarcsecond (mas) corresponds to 0.23 pc. Gardner *et al.* (1992) made a VLBI image of the 21 cm continuum emission and found that the radio nucleus of NGC 5793 is unresolved with a radius of 16 mas, or about 4 pc on

a linear scale. The NRAO Very Large Array (VLA)¹ observations of the intense HI and OH absorption toward the nucleus demonstrated that the absorbing gas is located in a compact region around the nucleus (Gardner *et al.* 1986) and the wide velocity range of the HI and OH absorption profiles, $\sim 200 \text{ km s}^{-1}$, is interpreted as the result of a number of clouds of dense gas along the line of sight. Gardner *et al.* (1992) also performed HI absorption-line imaging with VLBI and concluded that three absorbing systems with different velocities are present, two of which are associated with the nucleus, while the third may be associated with gas flowing away from the nuclear region. However, insufficient spatial resolution made it difficult to determine whether or not the absorption really arises from the nucleus itself.

Single-dish observations detected intense H_2O maser emission from NGC 5793 (Hagiwara *et al.* 1997). The spectrum shows strong high-velocity features displaced by $\sim \pm 245 \text{ km s}^{-1}$ on either side of the systemic velocity of the galaxy ($V_{\text{LSR}} = 3442 \text{ km s}^{-1}$), accompanying weaker features that are observed near the systemic velocity. Hagiwara *et al.* (1997) showed that the two velocity peaks of the H_2O systemic features seem to correspond to those of the OH absorption line peaks (Gardner *et al.* 1986), indicating a similar distribution of the H_2O and OH molecular gas in the galaxy. The parsec scale molecular absorption associated with AGN is a powerful tool for probing a inner layer of circumnuclear molecular gas which is considered as an energy source in the vicinity of a central engine. The nucleus of NGC 5793 also contains large opacity ($\tau > 2$) HI absorption covering a wide velocity range. According to the most recent HI absorption observation with VLBI, Pihlström *et al.* (in press) find that the atomic HI gas is not associated with the $< 10 \text{ pc}$ region close to the nucleus and suggest that it is probably associated with the outer galactic disk imaged using CO emission by Hagiwara (1998). In contrast, the OH molecular gas on parsec scales could trace a compact molecular gas disk/torus surrounding nucleus.

In this paper we describe the VLBI observations in Sect. 2, present the results of both continuum and OH absorption imaging in Sect. 3, and discuss the structure and kinematics of the nuclear region in Sect. 4.

Observations

Observations of NGC 5793 at both 18 cm continuum and OH spectral line were made with the Very Long Baseline Array (VLBA) and Very Large Array (VLA) operated as a phased array of the National Radio Astronomy Observatory (NRAO) on 1996 November 30. Observations of 6 cm continuum emission with the VLBA alone were carried out on 1997 October 15. In the session of the OH line at 18 cm, we observed the 1665 and 1667 MHz main line transitions of the $^2 \Pi_{3/2}$, $J=3/2$ ground-state of OH in absorption toward the background radio continuum source. A continuous full track observation of 7.3 hours was performed, of which about 4 hours were spent on NGC 5793.

At 6 cm we observed in a phase-referencing mode, using the calibration source 1507-168 about 2 degrees away from NGC 5793, although we later found that NGC 5793 could be detected without phase-referencing. The total time of one cycle was 6 minutes; 4 minutes for NGC 5793 and 2 minutes for 1507-168. The resulting total integration time spent on NGC 5793 was about 4 hours. At 18 cm the data were recorded in left circular polarization in four 8 MHz bands. At 6 cm data were recorded in dual circular polarization in four 8 MHz bands. At both wavelengths, the data were taken with 2-bit sampling.

At 18 cm each baseband channel was divided into 512 spectral points, yielding a frequency resolution of 15.6 kHz, which corresponds to a velocity resolution of 2.81 km s^{-1} . The total velocity coverage for

¹The National Radio Observatory is a facility of the National Science Foundation operated under cooperative agreement with Associated Universities, Inc.

each intermediate frequency band (IF) was 1440.5 km s^{-1} . In order to cover two OH absorption lines at 1665 and 1667 MHz plus the continuum we centered three IF bands on 3449, 3519, 3637 and one on 3190 km s^{-1} , respectively (hereafter, all velocities are in the radio definition and with respect to LSR). These four Doppler velocity centers were referenced to the 1667 MHz line. The first three IFs were calibrated separately and only one IF was used for absorption line imaging. The fourth IF was used for the continuum imaging since no absorption line or emission was present in the passband. At 6 cm, individual IFs with 16 spectral channels were combined into one continuum channel after phase and gain calibrations.

The system temperature and antenna sensitivity for each VLBA antenna over the observing frequency are 30 – 100 K and 11 Jy K^{-1} , respectively. The data were calibrated using the NRAO AIPS package. The delay and delay rate calibration was determined throughout the observation using 4C39.25 and 1507-168 as calibration sources. The absolute flux calibration was determined by observations of 3C 286. After the initial cleaned maps were obtained, self-calibration on the continuum source was employed, initially assuming a point source model, to refine the phase solutions.

Results

Continuum

The continuum image of NGC 5793 at 18 cm obtained from the OH absorption free IF channel is shown in Figure 1. The restoring beam size is 12.3×4.4 milliarcsecond (mas) in P.A. = -7.5° . The rms noise in this image is $0.21 \text{ mJy beam}^{-1}$. The map shows that the twisted radio structure is split into two parts: a central bright component [C1(C)] with accompanying minor components [C1(NE) and C1(SW)] and a western elongated feature in P.A. $\simeq -70^\circ$ (C2), connecting knots C2 and C3. The subcomponents C1(NE) and C1(SW) are almost symmetrically extended along a P.A. of 40° around the central peak of the C1(C). The knots C1(NE), C2, and C3 may compose a bending jet extending over nearly 18 pc across the C. The peak flux density of $308 \text{ mJy beam}^{-1}$ at C1(C) corresponds to a brightness temperature of $8.0 \times 10^9 \text{ K}$.

Figure 2 shows the 6 cm map with a restoring beam size of 3.7×1.4 mas in P.A. -4.7° . The rms noise in the image is $0.043 \text{ mJy beam}^{-1}$. Intensity of the central component C1(C) is the strongest also at this wavelength and its peak flux density is 91 mJy beam^{-1} corresponding to a brightness temperature of $2.6 \times 10^9 \text{ K}$. The twisted curvature of the structure is consistent with that of the 18 cm image. The component extends towards northeast and southwest, bending symmetry, and is connected with C1(NE). However, the component C1(SW) seen at 18 cm is not detected at 6 cm at all. The major axis of the overall distribution of the component C1 has a position angle of about 40° that is almost consistent with that previously obtained at 21 cm with the HPBW of 30 mas synthesized beam (Gardner *et al.* 1992). In the western elongation, we can clearly identify a new bright component C4 at its eastern edge, lying at a distance of 32 mas (7.4 pc) from the peak C1(C). The length of the western elongation is approximately 7.4 pc at 18 cm and 5.5 pc at 6 cm. The peak position of the component C2 at 6 cm is offset northward by ~ 5 mas from that at 18 cm.

The total flux density at 18 cm is $647 \pm 9 \text{ mJy}$ in figure 1, while $191 \pm 3 \text{ mJy}$ at 6 cm in figure 2. Based on a comparison with the VLA in B-configuration data (Gardner *et al.* 1986), we estimate that our images recover $\sim 65 \%$ of the total flux in the 18 cm map, but only $\sim 30 \%$ in the 6 cm map. Brightness temperatures (T_b) and Spectral indices at each component that are measured between two wavelengths with the same beam size are summarized in Table 2, using the 6 cm flux densities obtained from deconvolved beam size of 18 cm. The measured brightness temperatures of $10^8 \sim 10^9 \text{ K}$ is three to four orders of magnitude higher than the limit of T_b of $\sim 10^5 \text{ K}$ for starburst related thermal plus synchrotron emission

Table 1. Adopted parameters of NGC5793.

R.A. (J2000) ^a ...	14 ^h 59 ^m 24. ^s 030 ± 0. ^s 001
Decl. (J2000) ^a ...	-16°41'36".12 ± 0."02
Distance ^b ...	46 Mpc
Systemic Velocity(LSR) ^c ...	3442 ± 72 km s ⁻¹
Type ...	Sb; ^d Seyfert 2 ^e
Position angle of the major axis ^f ...	150°
Inclination angle of the galactic disk ^g ...	73°

^aPosition of a radio core determined by VLA (Whiteoak *et al.* 1987). The coordinates are converted from those of B1950

^bAssuming $H_0 = 75 \text{ km s}^{-1} \text{ Mpc}^{-1}$

^cHagiwara *et al.* (1997)

^dde Vaucouleurs *et al.* (1976)

^eBaan *et al.* (1998)

^fWhiteoak, Gardner (1987)

^gRoth (1994)

Table 2. VLBI Components In NGC 5793

Component	$S_{\text{peak}}^{\text{a}}$ (mJy beam ⁻¹)		T_{b}^{b} (K)		Spectral index $\alpha_{6-18 \text{ cm}}^{\text{d}}$
	18 cm	6-cm ($\theta_{\text{beam}} = \theta_{18\text{cm}}$) ^c	18 cm	6-cm	
C1(C) ...	308 ± 19	91.1 ± 4.6 (139 ± 7.0)	8.0×10^9	2.6×10^9	-0.70 ± 0.11
C1(NE) ...	80.1 ± 9.0	13.8 ± 3.0 (25.0 ± 1.3)	2.1×10^9	4.0×10^8	-1.0 ± 0.16
C1(SW) ...	12.8 ± 6.4	- ^e (-)	3.4×10^8	- ^e	-
C2 ...	18.0 ± 0.9	5.1 ± 0.3 (10.6 ± 0.5)	4.7×10^8	1.5×10^8	-0.46 ± 0.09
C3 ...	28.3 ± 1.4	5.3 ± 0.3 (12.2 ± 0.6)	7.4×10^8	1.6×10^8	-0.72 ± 0.10
C4 ...	(16.1)	11.1 ± 0.6 (18.5 ± 0.6)	(4.2×10^8)	3.2×10^8	(0.13)

^aPeak flux density

^bBrightness temperature

^cFrom image convolved to the resolution at 18 cm

^d $\alpha; S_{\nu} = \nu^{\alpha}$

^eThe component is not detected in 6 cm image

(Lonsdale *et al.* 1993), strongly suggesting that the nucleus of NGC 5793 contains AGN.

The OH Absorptions

The phase and gain solutions obtained with one absorption-free IF channel were applied to the IF channel which contains both absorption and continuum emission. The continuum level was determined by averaging all channels. The continuum emission was then subtracted from the spectral line visibility cubes. Figure 3 shows the 18 cm VLBA spectrum with a spectral resolution of 5.6 km s^{-1} , associated with C1(C); the two main OH transitions at 1665 and 1667 MHz are clearly seen in absorption. The 1667 MHz absorption spectra was also previously detected with VLA (Gardner *et al.* 1986). After continuum subtraction the spectrum has been converted to optical depth using the above continuum level. At both transitions, several velocity features are detected, although some with poor signal-to-noise ratio. We fitted a single Gaussian component to the spectrum shown in Figure 3 in order to determine the optical depth and velocity width. The quality of the data did not warrant using additional components. The resultant opacity, integrated intensity and column density are listed in Table 3. The absorption velocity center (Gaussian fitted) is $3454 \pm 9 \text{ km s}^{-1}$, while the center velocity derived by Gardner, Whiteoak (1986) is 3462 km s^{-1} . This difference between them can be explained by systematic errors. There is also weak evidence for the OH absorption of 1665 and 1667 MHz against components C1(NE) and C3, similar to that against the C1(C), while the absorption against C1(SW) and C2 are too weak to estimate optical depths. However, the optical depths, line shapes, and velocity widths of the OH towards both C2 and C3 do not show any significant difference from those towards C1(C). Figure 4 shows the total OH absorption integrated intensity image over 10 velocity channels or 56 km s^{-1} at 1667 MHz. The integrated absorption flux density is $-158 \text{ mJy km s}^{-1}$. Significant OH absorption is detected mainly around the position of C1(C) as seen in Figure 4. The absorption is apparently concentrated mostly around position of C1(C) indicating that the absorption traces the background continuum emission there. In figure 5, channel maps of the 1667 MHz OH absorption integrated every 5.6 km s^{-1} are shown; nine channel maps covering a velocity range -29 to 17 km s^{-1} are displayed. The absorption shows a velocity gradient from north to south, starting approximately at 3420 km s^{-1} at 5 mas north of C1 and moving to 3460 km s^{-1} at 3 mas south of C1. In figure 6, position-velocity diagrams of the 1667 MHz absorption are displayed. Cuts were made through component C1 along axes of P.A. = 60° (NE – SW) and P.A. = 150° (NW – SE) in Figure 1. A velocity shift of 40 km s^{-1} is seen over a distance of 10 mas or 2.3 pc in the velocity range $3425 < v < 3465 \text{ km s}^{-1}$. This velocity range symmetrically spans to the systemic velocity of NGC 5793, 3442 km s^{-1} . The velocity gradient in the 1665 MHz line does not clearly have the trend as that seen in the 1667 MHz. This is mainly due to low signal-to-noise ratio of 1665 MHz line data. From Figure 7 showing the mean velocity field, we measure a kinematic major axis across C1(C). The position angle of the axis is estimated about 150° .

Discussions

The Continuum Structures

We derive basic morphological and spectral properties of the parsec-scale radio structure of NGC 5793 from the 18 cm and 6 cm continuum maps and discuss the implications of these results. The continuum radio source has a core-jet structure that is typical for those seen in Seyfert galaxies and radio active galaxies. The VLBA data at both wavelengths suggest that the three components C1(C), C1(NE), and C3

Table 3. Parameters of the OH absorption feature.

	VLA ^a 1667 MHz	1665 MHz	VLBA 1667 MHz
Optical depth (τ)			
Peak value ...	0.065 ± 0.006	0.086 ± 0.015	0.085 ± 0.013
Gaussian fitted value ...	—	0.066 ± 0.016	0.080 ± 0.012
Center Velocity (LSR) ^b ...	3462 km s^{-1} ^c	$3445 \pm 3 \text{ km s}^{-1}$	$3454 \pm 4 \text{ km s}^{-1}$
ΔV (FWHM) ...	39.4 km s^{-1}	$18 \pm 0.4 \text{ km s}^{-1}$	$28.4 \pm 0.5 \text{ km s}^{-1}$
$\int \tau dv$...	—	1.53 km s^{-1}	3.75 km s^{-1}

^aGardner *et al.* 1986; No published data for 1665 MHz

^bVelocity center is referenced to the 1667 MHz OH absorption

^cConverted to Radio LSR definition; $V(\text{radio heliocentric}) - 8.0 \text{ km s}^{-1}$

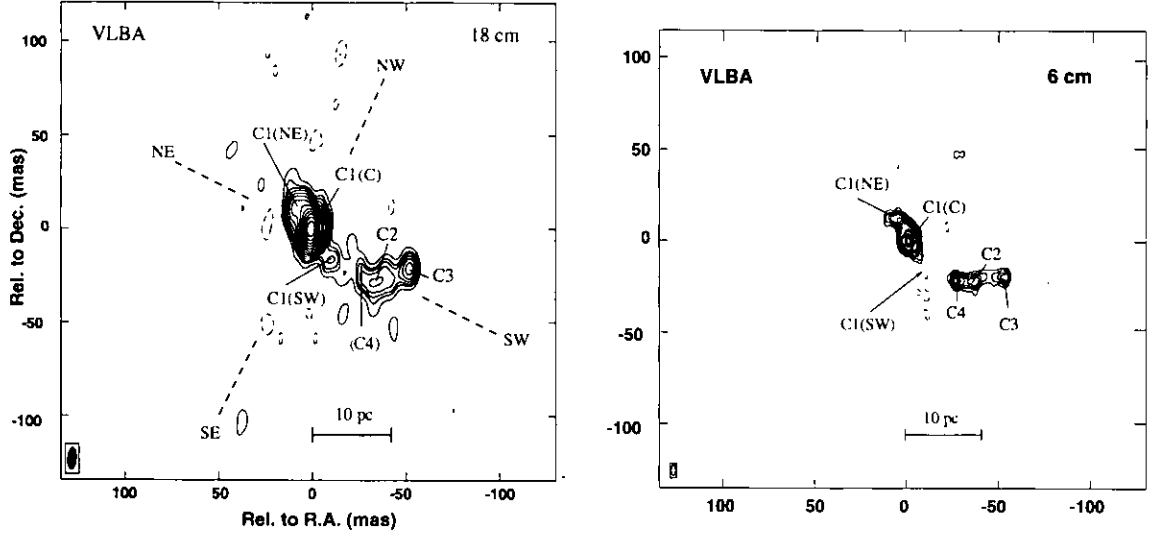


Fig. 1.— Fig. 1 (left): A cleaned VLBA map at 18 cm. The contour levels are -1%(dashed), 1%, 2%, 3%, 4%, 5%, 7%, 10%, 14%, 20%, 25%, 40%, 50%, 70%, and 100% of the peak surface brightness of $308.4 \text{ mJy beam}^{-1}$. The synthesized beam of 12.3×4.4 milliarcsecond (mas) in P.A. = -7.5° is shown in the left-hand corner. Fig. 2 (right): A cleaned 6 cm map. Contours are plotted at -1 (dashed), 1, 2, 3, 4, 6, 8, 10, 15, 20, 40, 60, 80, and 100 % of the peak surface brightness of $91.1 \text{ mJy beam}^{-1}$. The synthesized beam of 3.7×1.4 mas in P.A. = -4.7° is shown in the left-hand corner. The center position is the same as that in Fig.1.

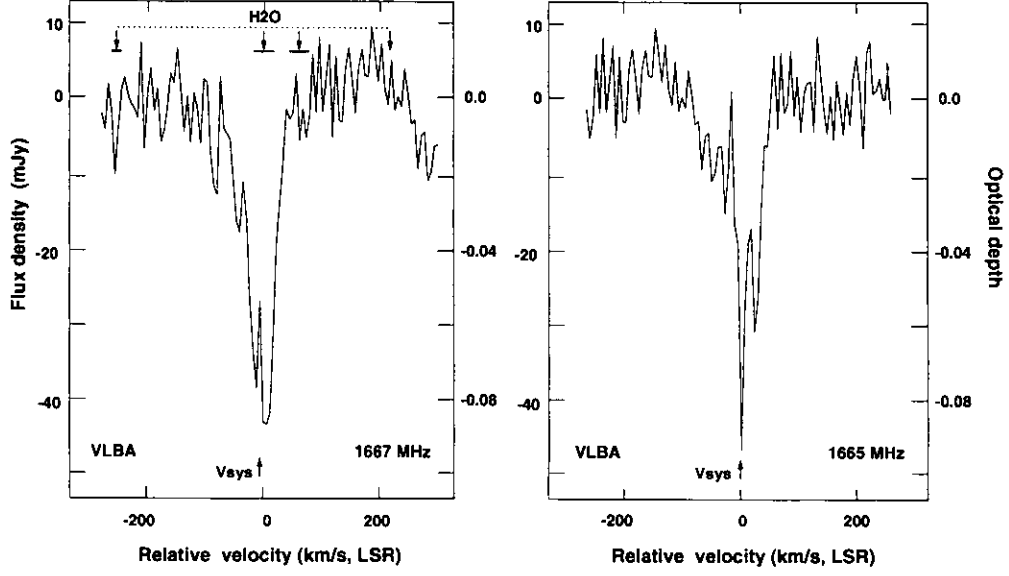


Fig. 2.— The OH absorption spectra of 1667 (left) and 1665 MHz (right) with a spectral resolution of 31.3 kHz, or 5.6 km s^{-1} . The absorption intensities are shown as to the flux density and optical depth. The relative LSR velocities are referred to the rest frequency of each OH transition at 1665.402 and 1667.359 MHz, or $V_{\text{LSR}} = 3445$ and 3454 km s^{-1} . The peak velocities ($V_{\text{LSR}} = 3190, 3449, 3519$, and 3677 km s^{-1}) and velocity ranges of the H_2O maser emission are indicated in the 1667 MHz frame by downward-pointing arrows and thick lines. The systemic velocity (V_{sys}) of 3442 km s^{-1} is denoted by an upward-pointing arrow.

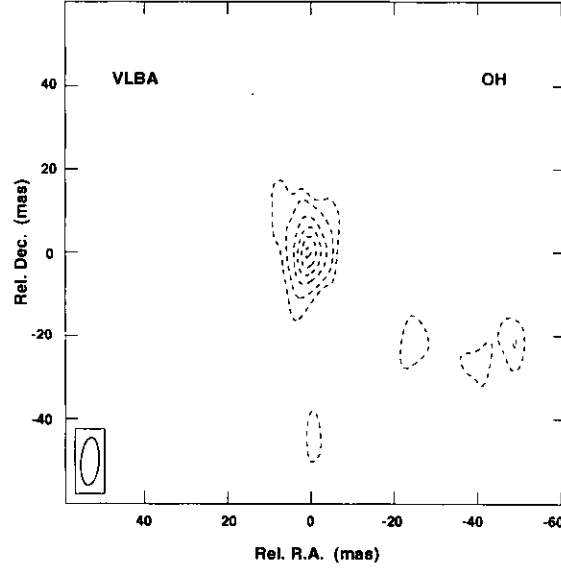


Fig. 3.— An integrated intensity map of 1667 MHz OH absorption, integrated over the velocity width of 44.8 km s^{-1} . The integrated velocity range is from $V_{\text{LSR}} = 3422 - 3467 \text{ km s}^{-1}$. Dashed contour levels are 98, 80, 60, 40, 20, and 10% of the peak intensity of $-158 \text{ mJy km s}^{-1} \text{ beam}^{-1}$. The synthesized beam is shown in the left-hand corner. Significant absorption intensity is seen only around C1(C).

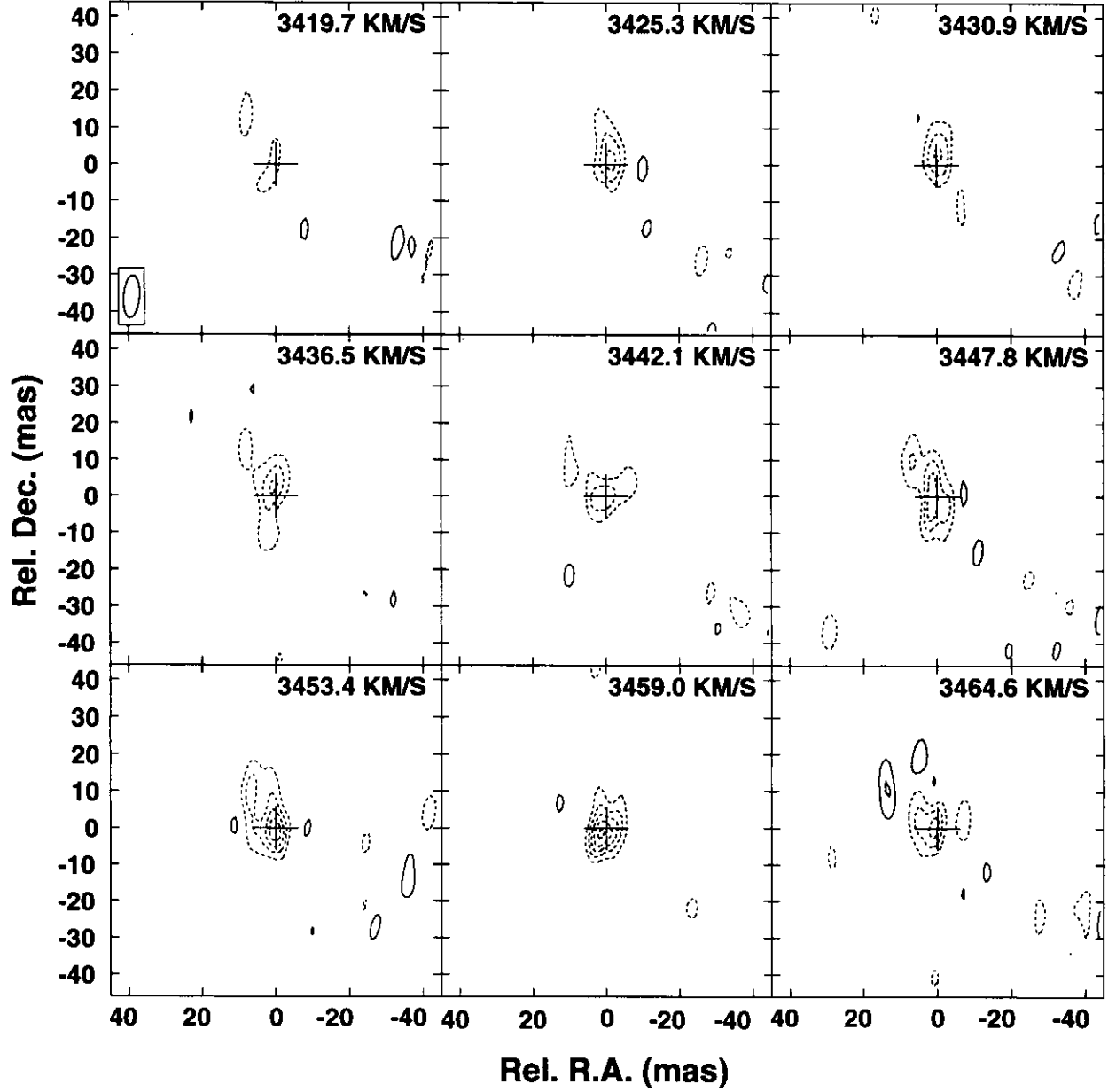


Fig. 4.— Velocity channel maps of the 1667 MHz OH absorption, each integrated over 5.6 km s^{-1} intervals. The contour levels are at -25, -20, -15, -10, -5 (1σ) (dashed), 5, and 10 (solid) mJy beam^{-1} . Each map is labeled in the upper right hand corner with the velocity (V_{LSR}) at the center of each channel. The cross in each panel denotes the position of the phase center. The synthesized beam is shown in the upper-left corner panel.

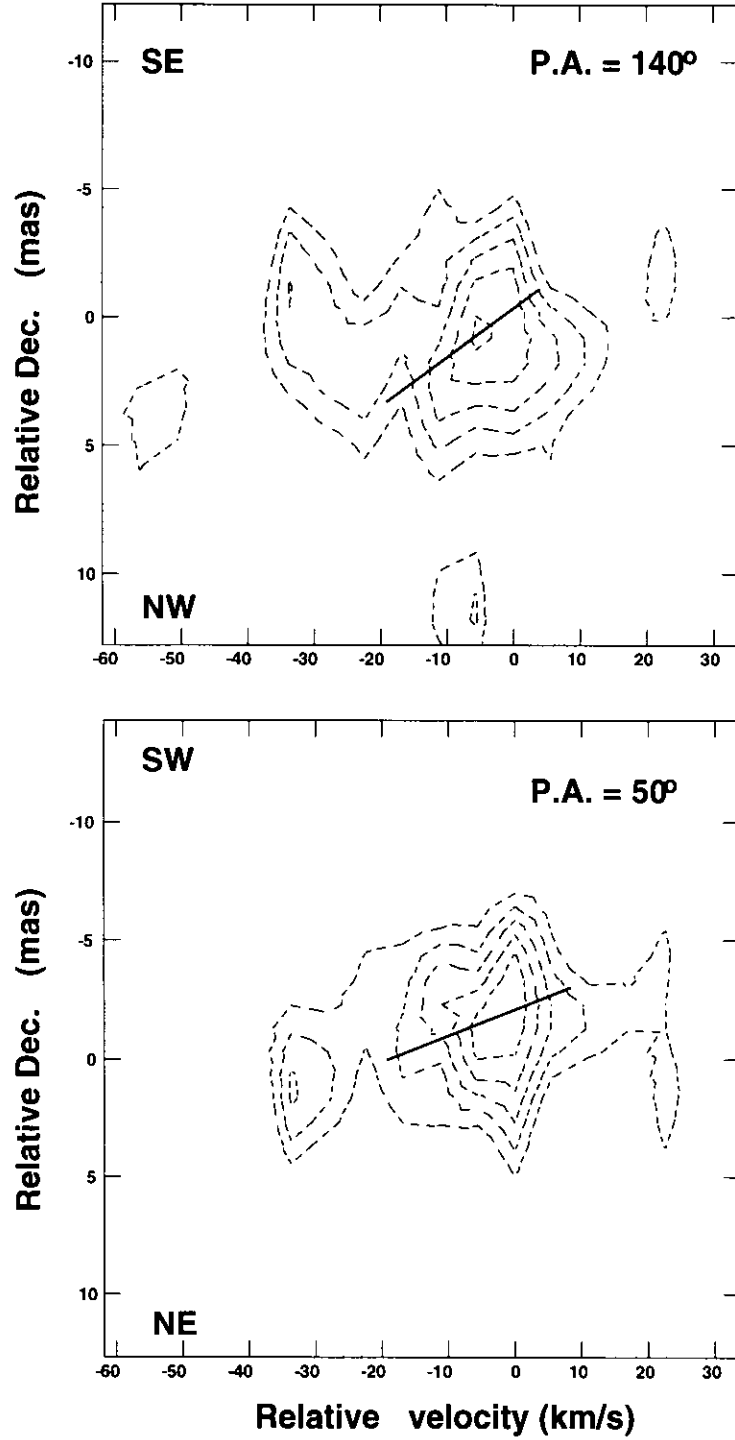


Fig. 5.— Position-Velocity diagrams of the OH absorption(1667 MHz) against the continuum center are shown with the velocity resolution of 5.6 km s^{-1} . In each diagram both the velocity and position are displayed by their offset values. The velocities are centered on 3459 km s^{-1} and the positions are measured from the continuum center, C1. A cut in each diagram shows that there exists a clear velocity gradient across the axis. *upper*; Sliced with P.A.= 140° nearly along the optical axis(150 deg.) across the C1(C). *lower*; Sliced with P.A. of 50° across the C1(C), taken perpendicularly to that of the upper diagram. The contour intervals are at 10%, 9%, 8%, 7%, 6%, 5%, 4%, 3%, -3%, -4 % of the peak flux density of $-32 \text{ mJy beam}^{-1}$, plotted from $-9.6 \text{ mJy beam}^{-1}$. The rms noise level is $4.5 \text{ mJy beam}^{-1}$ in both images.

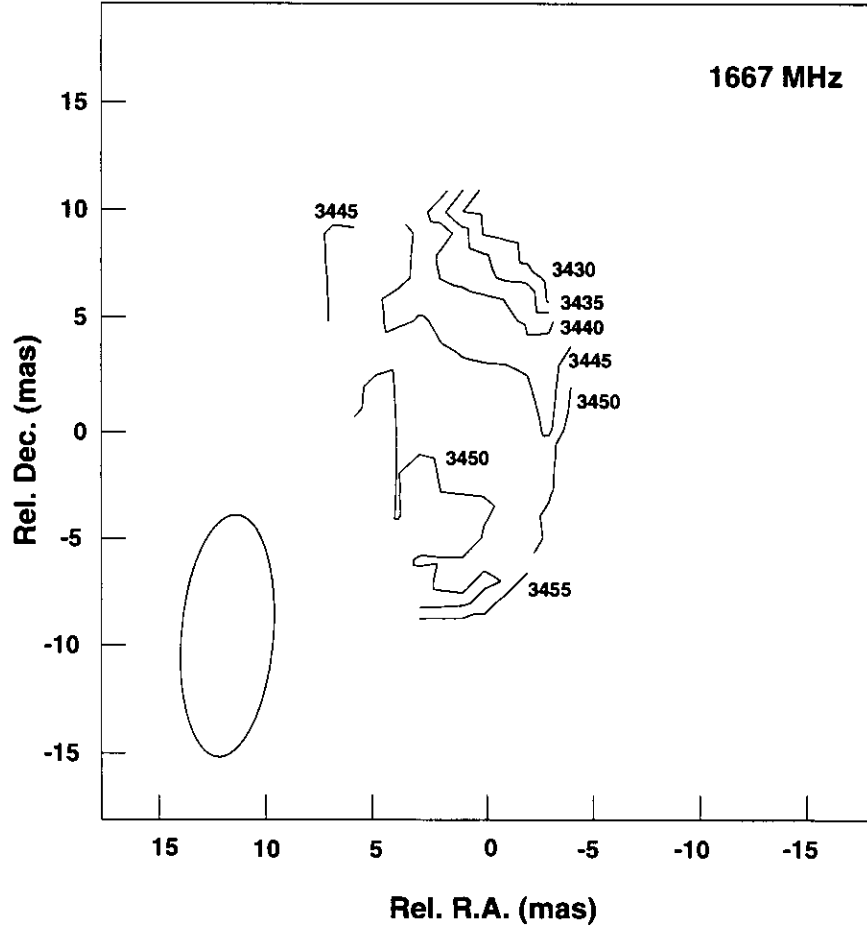


Fig. 6.— The first moment map shows a distinct velocity field for the OH absorption at 1667 MHz covering C1(C). Velocity contours are presented at 5 km s^{-1} intervals, and velocities are labeled in units of km s^{-1} (V_{LSR}). The 18 cm synthesized beam is plotted in the bottom left corner. The velocity gradient is clearly seen nearly along the major axis of the galaxy ranging from $V_{\text{LSR}} = 3430 - 3455 \text{ km s}^{-1}$.

have steep spectra of $-1.0 < \alpha < -0.7$ (see Table 2). The component C4 in the 6 cm map could not be clearly identified in the 18 cm map. Adopting the 18 cm flux density at the C4 position in 6 cm image to be 16.1 mJy, the spectral index of α would be 0.13. Only the spectrum at the C4 is definitely inverted ($\alpha > 0$) and flat between these two wavelengths. The C3 shows relatively flat spectrum among these four peaks, but it is safely to be said that the spectrum at C3 is also steep. One might ask which component is the 'true' radio core of the galaxy? If we assume that the continuum peak C1(C) is the core, it follows that the steep spectrum of C1(C) is due to mixture of spectra from several components including a flat-spectrum radio core, suggesting that the continuum structure is not still resolved on a few parsec from the center. Steep spectra in the range $-1.3 \lesssim \alpha \lesssim -0.5$ are generally observed in extragalactic extended radio sources (Barvainis and Lonsdale 1998), as those in the components in NGC 5793.

The other plausible candidate for the 'true' core is the C4 in the 6 cm image. In contrast to the structure at 6 cm, the 18 cm image at the position of C4 shows weak extended radio emission. There are two possible explanations for this. We can account for the relative faintness of C4 at 18 cm by invoking a model of free-free absorption by the optically thick intervening gas, which is highly inclined to the line of sight. In this case, the relative flatness of the C4 spectrum can be explained by a radio continuum core lying inside the obscuring gas in our line of sight. Both the central continuum structure containing C1(C) and the western extended emission containing C2 and C3 could be interpreted as jets that are directed from the highly inclined disk/torus, whose major axis lies at P.A. of $\sim 140^\circ$. Alternatively, our failure to detect the component C4 in 18 cm map could be explained by the time variability of the flux density between the two observing epochs and due to the relative faintness of 18 cm flux density, the spectrum at C4 apparently shows flat, positive spectral index (see Table 2). In this case, the real spectrum at the C4 might be as steep as other components.

Uncertainty of the C4 position and spectrum in both images makes us difficult to conclude that the C4 is the nucleus. It is likely that C1(C), the most intense continuum peak, might be a position of the 'true' radio nucleus. The C1(SE), C2, C3, and C4 are the continuous chain of jet ejected from the nucleus, while the C1(NE) is the counter jet extending toward north-east. The bending structure of the jet nearly at the C4 could be explained by deflection by gas clouds and the collimation axis of the jet is forced to be changed there.

Properties of the OH Absorption

Table 3 lists the single-Gaussian fitted parameters derived at C1(C) from the observed spectra in Fig. 3. The optical depth in the OH line at 1667 MHz, derived with the VLA in A-configuration was 0.065 ± 0.006 (Gardner *et al.* 1986), while that derived from our VLBA data is 0.080 ± 0.012 at the Gaussian peak. The optical depth obtained by the smaller VLBA synthesized beam (HPBW = $0.012''$) is consistent with that observed with the VLA (HPBW = $4''$) within the errors. As mentioned in the previous section, we found no significant absorption at other positions in the continuum emission image, implying the possibility that the foreground absorbing gas is spatially confined. The coincidence of these optical depth values within the errors does not contradict the above description. The velocity widths of the absorption line in the 1667 MHz transition obtained with the VLBA ($28.4 \pm 0.5 \text{ km s}^{-1}$) is narrower by $\sim 30\%$ than that observed with the VLA (39.4 km s^{-1}). This is attributed to the $\sim 35\%$ missing flux density of the background continuum emission (which is resolved on parsec scales in our VLBA image). The extended radio continuum emission imaged by the VLA-A array, which is resolved in the 18 cm VLBA continuum image, seems to contribute several weaker OH velocity components which we cannot see in the VLBA profiles. It is interesting that compared with the HI absorption line widths from $< 100 \text{ pc}$ scale circumnuclear gas in Seyfert nuclei such

as NGC 4151 (Mundell *et al.* 1995; Dickey 1986), the OH absorption of NGC 5793 is much narrower. Assuming the gas to be optically thin (The optical depth of 0.08 supports the fact that the OH absorbing layer is not optically thick.), we can estimate the OH column density along the line of sight. The OH column density at 1667 MHz is as the following:

$$N(\text{OH}) = 2.2 \times 10^{14} T_{\text{ex}} \int \tau dv \text{ [molecules cm}^{-2}\text{]}, \quad (5.1)$$

where T_{ex} is the OH excitation temperature (Elitzur 1992). Adopting the value for the absorption intensity from Table 4 the column density is $\sim 8.4 \times 10^{14} T_{\text{ex}}$ molecules cm^{-2} , which is in the range of the OH column densities found in molecular disks of galaxies (Baan *et al.* 1984, Baan *et al.* 1992).

The absorption profiles in Fig. 3 show that the 1667 MHz feature is as deep as the 1665 MHz feature. For local thermodynamic equilibrium (LTE), the OH line ratio of the 1667/1665 MHz transition is expected to be 1.8 (Elitzur 1992). The hyperfine ratios of the peak OH optical depths and the OH opacity intensity derived by single Gaussian-fitting of the absorption line of each transition is 1.3 ± 0.1 and 2.5 ± 0.2 (see Table 3), showing significant deviation from the theoretical LTE ratio of 1.8 seen in galactic objects (; Lucas *et al.* 1996). However, deviation from the LTE value is not unusual in extra-galactic objects (e.g., Baan *et al.* 1995). Low signal-to-noise ratios in the absorption profiles prevent us from a detailed discussion of the line ratio. Since the absorbing gas is probably spatially extended with respect to the synthesized beam, the effect of a beam-filling factor cannot be ruled out.

Distributions and Kinematics of Molecular Gas

The most intriguing result derived from our observations is that an OH velocity gradient symmetrically spanning the systemic velocity in the central region was detected. We determined a value of $\approx 8.7 \text{ km s}^{-1} \text{ pc}^{-1}$ for the velocity gradient across C1(C). Since the intensity distribution of the OH absorption (Fig. 4) (although it is difficult to make a map of OH optical depth because of the weakness of the continuum except at C1(C)) is well correlated with that of the background continuum emission (Fig. 1), the column density of OH does not vary across the continuum, suggesting that OH gas is distributed over a wider area than the continuum. Because the OH absorption is not seen in the outer region due to a lack of background continuum emission, it might be difficult to determine if the OH velocity field around C1(C) is caused by molecular gas associated with the nucleus. Nevertheless, in this section we examine the kinematical properties of the OH gas, making use of the results of H_2O maser and CO molecular gas observations.

High-resolution millimeter observations of CO ($J = 1-0$) with the Nobeyama Millimeter Array (NMA) found a rotating molecular gas structure in the central region of the galaxy with a radius of $\sim 1 \text{ kpc}$ along P.A. = $\sim 140^\circ$, spanning $V_{\text{LSR}} = 3305 - 3661 \text{ km s}^{-1}$ (Hagiwara *et al.* 1997, Hagiwara *et al.* 1998a). In this paper, the OH velocity gradient shows a reversal of the sense of rotation observed in the central region of $\sim 10 \text{ pc}$. This suggests that the OH absorbing gas that we detected with the VLBA is kinematically distinct from the outer disk observed in CO. This kind of compact gaseous subsystem which is kinematically independent from the larger scale galactic molecular gas disk has been observed in other galaxies, such as, NGC 4826 (Braun *et al.* 1992), NGC 253 (Anantharamaiah and Goss 1996), and NGC 3079 (Sato *et al.* 1998).

In the following we consider that the velocity gradient observed around C1 might arise from a rotating molecular disk with a radius (r) centered on the nucleus. In order to explain the H_2O spectrum showing systemic and red- and blue-shifted features in NGC 5793, Hagiwara *et al.* (1997) proposed a nearly edge-on circumnuclear molecular disk/torus with a radius of $r > 4 - 20 \text{ pc}$ and a rotation velocity of $V_{\text{rot}} = 245 \text{ km}$

s^{-1} .

$$\frac{dV}{dl} = \frac{dV_{\text{rot}}\theta}{d(r\theta)} \simeq \frac{V_{\text{rot}}}{r} \quad (5.2)$$

, where l is the projected distance from the source center, $i = 73^\circ$ is an inclination of the molecular rotating disk, and $\sin\theta \approx \theta$ is adopted (Nakai 1995b). We adopt the inclination of the OH disk is to be 73° that of galaxy's optical disk. For $V_{\text{rot}} = 245 \text{ km s}^{-1}$ and $dV/dl = 8.7 \text{ km s}^{-1} \text{ pc}^{-1}$, r is estimated to be about 28 pc. Using this value for the radius of a molecular disk/torus around C1(C), the mass confined within the disk is $4.2 \times 10^8 M_\odot$. This estimate is larger by approximately a factor of three than the mass previously derived from water maser profiles (Hagiwara *et al.* 1997), because they adopted $r = 10 \text{ pc}$. We must note, however, that the mass estimate will depend on the assumed inclination angle of the rotating gas disk. The fact that H_2O maser features were preferentially observed in the edge-on molecular disks supports our assumption (e.g., Miyoshi *et al.* 1995). On the other hand, the gas mass of molecular hydrogen that is determined from the CO intensity in the outer disk is $7.9 \times 10^9 M_\odot$ (Hagiwara *et al.* 1998a). The OH gas mass within a radius of 10 mas or 23 pc from the continuum peak corresponds to about 5% of that in the CO disk with a radius of $\sim 1 \text{ kpc}$, implying that the density of observed OH gas is significantly greater than that of the outer molecular gas disk.

Relation to H_2O Maser Emission and HI Absorption

One of our motivations for this observation was to investigate whether or not the OH absorption in NGC 5793 takes place in the same molecular cloud that contains the H_2O maser. The centroid velocities of the H_2O emission peaks at $V_{\text{LSR}} = 3449$ and $3519 \pm 5 \text{ km s}^{-1}$ are close to those of the OH absorption lines observed with the VLA (Gardner *et al.* 1986), although only the OH feature at 3449 km s^{-1} was detected in our VLBA observation (the 1667 MHz spectrum of Fig. 3). The 3519 km s^{-1} absorption feature, which is weaker than that at 3449 km s^{-1} , was not clearly detected, probably because the extended background continuum necessary to observe it in absorption is resolved with the VLBA. Another OH velocity component was found in the velocity range of the H_2O maser feature at 3449 km s^{-1} , however there is no clear evidence for a rotating OH molecular disk/torus around the nucleus or a relationship with the proposed water maser disk proposed in Hagiwara *et al.* (1997). The large value of the OH column density along the line of sight, the high mass density of the observed absorbing cloud and the existence of the velocity gradient around the nuclear region, dynamically independent from the outer galactic disk, demonstrate that the observed OH absorption probably arises through the dense molecular gas in the circumnuclear region of NGC 5793. On the other hand, according to the most recent HI absorption studies with VLBA, no significant velocity field similar to the OH field (this paper) is not detected (Pihlström *et al.*, in press). The HI absorbing clouds might trace the region in physically different condition, where OH gas distributes, because the HI absorption line features show optically thick ($\tau = 2.0 \sim 2.5$) properties.

Summary

We have mapped the distribution of continuum emission and of the OH absorption at 1667 MHz in the Seyfert galaxy NGC 5793 on parsec scale with VLBI. The observed structure of the OH absorption shows a velocity gradient across the continuum structure of C1, symmetrically spanning with respect to the systemic velocity. The direction of the OH velocity gradient is inconsistent with that of rotation of the

kiloparsec scale CO disk of the galaxy, though the P.A. of these two axes are nearly aligned: we discovered a counter-rotating gaseous component in the inner region on 10 parsec scale. If circular rotation across C1(C) is assumed to explain the velocity gradient, based on analogy with the H₂O maser emission in the galaxy, the binding mass is $4.2 \cdot 10^8 M_{\odot}$. This value corresponds to nearly 5 % of the molecular gas mass existing in the kiloparsec-scale galactic disk. The interpretation of the observed OH absorption distribution is not unique. The OH absorption could arise from dense molecular gas in the 10 parsec scale circumnuclear disk/torus or from spatially extended diffuse molecular gas on kiloparsec scales in the galactic disk. The structure and spectra of the continuum components are difficult to interpret. However, C1(C) is the strongest component and is that against which its strongest OH absorption occurs, suggesting that C1(C) is the core. More data are required to resolve this issue.

VLBA observations at 1.3 cm on smaller than parsec scale, already underway, will hopefully be able to reveal the relationship between the distribution of H₂O masers and molecular absorptions.

Chapter 6

SUMMARY

The construction of the Rainbow Array system; NMA – NRO 45 m telescope interferometer was successfully conducted. After the verification of mapping performance of the Rainbow Array system, spectral line observations of peculiar, radio-loud galaxy NGC 1275 have been carried out using this new facility. The data presented here represent the first attempt to combine the high resolutions and sensitivities of NRO telescopes to give more detailed astronomical images. The synthesized beam attained, roughly, $1''.0$ at λ 2.6 mm, which corresponds to ~ 400 pc at the distance to NGC 1275, 70 Mpc. This beam size is appropriate for investigating the molecular torus/disk in the circumnuclear region of AGN, because the spatial extent of the circumnuclear torus/disk is believed to be sufficiently smaller than 1 kpc scale from the nucleus, which is inferred from the molecular torus found in M 51 and NGC 1068.

Rainbow observations of NGC 1275 revealed that the molecular gas of $\sim 10^9 M_{\odot}$ is concentrated within $r = 400$ pc from the nucleus. The discovery of this CO emission peak is confirmed by the following NMA observations at the $9''$ resolution. Then, I found that the lack of CO peak at the nucleus in the published image obtained by Inoue *et al.* (1996) is due to the error in their analysis when determining the continuum baseline. The distribution of $2.1 \mu\text{m}$ H_2 emission which they also reported the detection nearly matches the unresolved size of CO peak emission at the nucleus. Therefore, I am confident that the high-resolution CO images obtained by the Rainbow Array are reliable. When combined the observational results with those obtained from Inoue *et al.* (1996) and broad-band HST images, it will be clear that the circumnuclear region traced by molecular gas shows the characteristic structure; the ring-like structures at the radius 1.2 kpc from the nucleus, the molecular bar-like structure intermediates between the CO *twin peaks* and the nuclear gas concentration. This is quite similar to that in Seyfert galaxy NGC 1068 with a radio-quiet nucleus. These similarities in morphology suggest that the detected CO peak emission could be interpreted as a result of gas fueling phenomenon along the molecular bar from the crowding of gas in the ring-like orbital structure.

It is very interesting that a scenario for the energy transport mechanism into the radio-loud nucleus is similar to that for the radio-quiet nucleus. I conclude that what determines the radio activity in NGC 1275 is *not* the circumnuclear gas extending on 100 pc – 1 kpc scales, but it might relate to the activity in the central engine on less than sub-parsec scales.

The search for circumnuclear region in the radio-active galaxy, NGC 5793 began with the detection of high-velocity water maser features in the galaxy. VLBI investigations of its circumnuclear region were then conducted using VLBA at a milli-arcsecond resolution, which enables the sub-parsec scale maser mapping

in NGC 5793. The VLBA observations detected only the blue-shifted velocity features. The maser spots were found to be offset from the continuum peak by about 3 pc in good alignment with a position angle of nuclear continuum jet-like structure. The maser emission could arise in a molecular cloud foreground to the jet, and be amplifying the radio jet in the background, unlike the situation found in NGC 4258. Intense research for the kinematics of masers should be made to find for velocity structures or maser distribution to refine our understanding on the nuclear region of AGN.

High-resolution imaging of OH absorption with VLBA revealed that there exists compact OH gas distribution on about 5 pc from the radio nucleus in NGC 5793. The OH molecular absorption shows the velocity gradient along the axis of the galactic disk in larger scale. The sense of velocity gradient is inconsistent with that of the CO disk with a radius of about 600 pc, which was obtained from the NMA observation. The OH absorbing gas might trace the parsec scale molecular gas in the dusty tours in the circumnuclear region of this galaxy.

This thesis pursued the investigation of two radio-active galaxies, NGC 1275 and NGC 5793. I researched the circumnuclear region in radio-active AGN by means of molecular gas (CO, OH, H₂O) on different scales from 1 pc to 1 kpc relative to the nucleus in hoping that I will be able to find the characteristic mechanism which provides the energy into the active nucleus, however, no significant differences between radio-quiet and radio-active nucleus in both of galaxies are found. This type of research should be conducted until we can measure a larger sample of sources.

Acknowledgements

I would like to thank my supervisor Ryohei Kawabe and Ko-Ichiro Morita for the use of facilities at the Nobeyama Radio Observatory and a number of useful advice in their academic fields and Rainbow projects that I have been involved.

I am grateful to Sachiko Kawabe-Okumura for continuing assistance in observations and data reduction of NGC 1275. Thanks are also due to Kazuyoshi Sunada, who actually taught me up the instrumentation of the SIS receiver in the first place. In designing the optical feeding system mounted on the 45 m telescope cabin, I received kind suggestions and advice from Jyunji Inatani, Nobuharu Ukita and Takashi Noguchi. During observations on which this thesis is based, I was fortunate to get extensive assistance by Kotaro Kohno, Kiyoshi Nakajima and Masao Saito while I was unfamiliar to the NMA observing system.

In interpreting of my data and the previous NMA observations on NGC 1275, I have benefitted from helpful discussions with Seiji Kamenno and Baltasar Vila-Vilaro. I wish to express gratitude to Takenori Nakano for frequent and helpful discussions in the general field of astronomy.

Other major contributors to this thesis have included Phil Diamond, Naomasa Nakai and Makoto Miyoshi, who introduced me to the megamaser observations using VLBA and VLA when I began to study AGN in Nobeyama. I was further indebted to the NMA staffs, and in particular to Hiroyuki Iwashita and Toshikazu Takahashi for the laboratory experiments during the period of receiver development and the staffs of the several observatories.

I would like to express my special gratitude to my officemates in Room 201, Munetake Momose, Dyukgyo Roh, Takahiro Tsutsumi, Toshihito Shibatsuka, Satoki Matsushita and Ray Furuya for their good companionship as well as their patience. I must not forget to mention about PC freaks, Takeshi Kamazaki and Seiji Katagiri, who provided me a way to escape from the academic work by putting me up to the 'Windows world'. The construction of the Rainbow system is a labor-intensive form of radio interferometry at millimeter wave as well as VLBI, although it has been my good fortune to be given an opportunity in joining this promising project.

This research was supported in part by the Foundation for the Promotion of Astronomy of Japan.

I have looked forward a long time to being able to acknowledge today the aid by Mother for never asking why I did not get a regular occupation and for letting me to do what I believe – no matter what it would be.

REFERENCES

- Adams, T. and Weedman, D. 1975, MNRAS, **199**, 19
- Allen, S.W., and Fabian, A.C. 1997, MNRAS, **286**, 583
- Anantharamaiah K.R., Goss W.M., 1996, ApJ, 466, L13
- Antonucci, R.R.J., and Miller, J.S. 1985, ApJ, **297**, 621
- Antonucci R., and Barvainis R. 1990, ApJ, **363**, L17
- Antonucci, R. 1993, ARA&A, **31**, 473
- Awaki, H. 1997, In *“Emission Lines in Active Galaxies: New Methods and Technics ”*, IAU Colloquium 159, eds. by B.M.Peterson, F-Z Cheng, and A.S.Wilson, San Francisco: ASP, 44
- Baan, W.A., Haschick, A.D. 1984, ApJ, **279**, 541
- Baan, W.A., Rhoads, J., Haschick, A.D. 1992, ApJ, **401**, 508
- Baan W. A., Irwin J. A., 1995, ApJ, 446, 602
- Baan W. A., Salzer J. J., LeWinter, R. D., 1998, ApJ, 509, 633
- Barthel, P.D. 1989, ApJ, **336**, 60
- Barvainis, R., and Lonsdale, C. 1998, AJ, **115**, 885
- Blandford, R.D. 1990, in *Active Galactic Nuclei*, ed. by T.J.L. Courvoisier and M. Mayor, 161
- Bloeman, J.B.G.M., et al. 1986, A&A, **154**, 25
- Braatz, J.A., Willson, A.S., Henkel, C. 1994, ApJ, **437**, L99
- Braatz, J.A., Willson A.S., and Henkel C. 1994, ApJS, **106**, 51B
- Braatz, J.A., Willson A.S., and Henkel C. 1996, ApJS, **106**, L51 (Paper I)
- Braatz, J.A., Willson A.S., and Henkel C. 1997, ApJS, **110**, 321 (Paper II)
- Braine, J., Wyrowski, F., Radford, S.J.E., Henkel, C., and Lesch, H. 1995, A&A, **293**, 315
- Braun R., Walterbos R. A. M., Kennicutt R. C., Jr., 1992, Nature, 360, 442
- Bridges, T.J. and Irwin, J.A. 1998, MNRAS, **300**, 967
- Burbidge, E.M., and Burbidge, G.R. 1965, ApJ, **142**, 1351
- Chikada, Y., Ishiguro, M., Hirabayashi, H., Morimoto, M., et al. 1987, IEEE Proc. **75**, 1203
- Claussen, M.J., Heiligman, G.M., and Lo, K.Y. 1984, Nature, **310**, 298
- Claussen, M.J., Diamond, P.J., Braatz, J.A, Wilson, A.S., and Henkel, C. 1998, ApJ, **500**, L129
- Combes, F., and Gerin, M. 1985, A&A, **150**, 327

- Condon, J.J., Helou, G., Sanders, D.B., Soifer, B.T. 1990, ApJS, **73**, 359
- Condon, J.J., Frayer, D.T., Brodrick, J.J. 1991, AJ, **101**, 362
- Conway, J.E., and Blanco, P.R. 1995, ApJ, **449**, L131
- Conway, J.E. 1998, In *Radio Emission from Galactic and Extragalactic Compact Sources, IAU Colloquium 164*, eds. by J.A.Zensus, G.B.Taylor and J.M.Wrobel, San Francisco: ASP, 231
- de Vaucouleurs G., de Vaucouleurs A., Corwin H.G. Jr. 1976, Second Reference Catalogue of Bright Galaxies, University of Texas, Austin
- de Young, D.D., Roberts, M.S, and Sasalaw, W.C. 1973, ApJ, **185**, 809
- Dickey, J.M. 1986, ApJ, 300, 190
- dos Santos, P.M., Lepine, J.R.D. 1979, Nature, **278**, 34
- Drinkwater, M.J., Combes, F., and Wiklind, T. 1996, A&A, **312**, 771
- Ekers, R.D., van der Hulst, J.M., and Miley, J.K. 1976, Nature, 176,**262**, 369
- Elitzur M., 1992, Astronomical Masers (Kluwer Academic Publishers)
- Fabian, A.C., Nulsen, P.E.J., and Canizares, C.A. 1984, Nature, **310**, 733
- Fabian, A.C. 1994, ARA&A, **32**, 277
- Fanaroff, B.F., and Riley, J.M. 1974, MNRAS, **167**, 31
- Fath, E.A. 1911, ApJ, **33**, 58
- Ferruit, P., and Pecontal, E. 1994, A&A, **288**, 65
- Gallimore, J.F., Baum, S.A., O’Dea, C.P., Brinks, E., and Pedlar, A. 1996, ApJ, **462**, 740
- Gallimore, J.F., Baum, S.A., O’Dea, C.P. 1996, ApJ, **464**, 1996
- Gallimore, J.F., Baum, S.A., and O’Dea, C.P. 1997, Nature, **388**, 852
- Gardner F.F., Whiteoak J.B. 1986, MNRAS, 221, 537
- Gardner, F.F., Whiteoak J.B., Norris R.P., Diamond P.J. 1992, MNRAS, **258**, 296
- Golombek, D., Miley, G.K., and Neugebauer, G. 1988, AJ, **95**, 26
- Greenhill L.J., Jiang, D.R., Moran, J.M., Reid, M.J., Lo K.Y., Claussen, M.J. 1995, ApJ, **440**, 619
- Greenhill, L.J., Gwinn, C.R., Antonucci, R.R.J., and Barvainis, R. 1996, ApJ, **472**, L21
- Greenhill, L.J., Moran J.M., and Herrnstein, J.R. 1997, ApJ, **481**, L23
- Gunn, J.E. 1979, in *Active Galactic Nuclei*, Cambrigde University Press, 213
- Hagiwara, Y., Kohno, K., Kawabe, R., Nakai, N. 1997, PASJ, **49** , 171

- Hagiwara, Y., Diamond, P.J., Kawabe, R., Nakai, N. 1998, In *Radio Emission from Galactic and Extragalactic Compact Sources, IAU Colloquium 164*, eds. by J.A.Zensus, G.B.Taylor and J.M.Wrobel, San Francisco: ASP, 233
- Hagiwara, Y., Diamond, P.J., Kawabe, R., Nakai, N., in preparation
- Heckman, T.M., Eric, P.S., Baum, S.A., van Breugel, W.J.M., et al. 1986, ApJ, **311**, 526
- Heckman, T.M., Baum, S.A., van Breugel, W.J.M., and McCarthy, P. 1989, ApJ, **338**, 48
- Helfer, T.T. and Blitz, L. 1995, ApJ, **450**, 90
- Herrnstein, J.R., Greenhill, L.J., Moran, J.M., Diamond, P.J., Inoue, M., Nakai, N., and Miyoshi, M. 1998, ApJ, **497**, 69
- Ho, L.C., Filippenko, A.V., and Sargent, W.L.W. 1995, ApJS, **98**, 477
- Ho, L.C. 1996, PASP, **108**, 637
- Holtzman, J.A., Faber, S.M., Shaya, E.J., et al. 1992, AJ, **103**, 691
- Inoue, Y. M., Kamenno, S. Kawabe, R., Inoue, M., Hasegawa, T., and Tanaka, M. 1996, AJ, **111**, 1852
- Inoue, M. Ph.D Thesis, 1995, Tokyo University
- Irvine, W.M., Goldsmith, P.F., Hjalmarson, A. 1986, in “Interstellar Processes”, eds. Hollenbach, D.J., Thronson, Jr., H.A. (Reidel), 561
- Ishizuki, S., Kawabe, R., Ishiguro, M., Okumura, S.K., Morita, K-I., Chikada, Y., and Kasuga, T. 1990, Nature, **344**, 224
- Jackson, J.M., Paglione, T.D., Ishizuki, S., and Nguyen-Q-Rieu. 1993, ApJ, **418**, 13
- Jenkins, C.R. 1983, MNRAS, **205**, 1321
- Joint IRAS Working Group, 1985, IRAS Point Source Catalog (Washington, D.C., U.S. Govt. Printing Office)
- Shields, J.C., and Filippenko, A.V. 1990, ApJ, **353**, 7
- Kaneko, N., Morita, K., Fukui, Y., Takahashi, N, Sugitani, K., Nakai, N., and Morita, K-I. 1992, PASJ, **44**, 341
- Kawara, K., and Taniguchi, Y. 1993, ApJ, **410**, 19
- Kenney, J.D.P., Wilson, C.D., Scoville, N.Z., Devereux, N.A., and Young, J.S. 1992, ApJ, **395**, 79
- Khachaman, Y., Weedman, R. 1971, ApJ, **336**, 13
- Koekemoer, A.M., Henkel, C., Greenhill, L.J., Dey, A., Breugel, W.V., Codella, C., Antonucci, R. 1995, Nature, **378**, 697
- Kohno, K., Kawabe, R., Tosaki, T., and Okumura, S.K. 1996, ApJ, **461**, 29
- Kohno, K. Ph.D Thesis 1998, Tokyo University.

- Lazareff, B., Castets, A., Kim, D.W., and Jura, M. 1989, ApJ, **336**, 13
- Lees, J.F., Knapp, G.R., Rupen, M.P., and Philips, T.G. 1991, ApJ, **379**, 177
- Longo G., de Vaucouleurs A. 1983, University of Texas, Austin Astronomy Monographs, No. 3
- Lonsdale, C.J., Smith, H.E., Lonsdale, C.J. 1993, ApJ, **405**, L9
- Lucas, R., Liszt, H.S. 1996, A&A, **307**, 237
- Lynds, R. 1970, ApJ, **159**, L151
- Matsusita, S., Kohno, K., Vila-Vilaro, B., Tosaki, T., and Kawabe, R. 1998, ApJ, **495**, 267
- Mazzarella, J.M., Graham, J.R., Sanders, D.B., and Djorgovski, S. 1993, ApJ, **409**, 170
- Meixner, M., Puchalski, R., Blitz, L., Melvyn, W., and Heckman, T. 1990, ApJ, **354**, 158
- Minkowski, R. 1957. IAU Symposium 4, “*Radio Astronomy*” ed. H.C.van de Hulst (Cambridge; Cambridge Univ. Press), 107
- Mirabel, I.F., Sanders, D.B., and Kazes, I. 1989, ApJ, **340**, L9
- Mirabel, I.F. 1989, ApJ, **340**, L13
- Miyoshi, M., Moran, J. M., Herrnstein, J. R., Greenhill, L. J., Nakai, N., Diamond, P. J., and Inoue, M. 1995, Nature, **373**, 127
- Moellenbrock, G.A., Fujisawa, K., Preston, R.A., Gurvits, L.I., Dewey, R.J., Hirabayashi, H., Inoue, M., Kamenno, S., Kawaguchi, N., Iwata, T., Jauncey, D.J., Migenes, V., Roberts, D.H., Schilizzi, R.T., and Tingay, S.J. 1996, AJ, **111**, 2174
- Mundell, C.G., Pedlar, A., Baum, S.A., O’Dea, C.P., Gallimore, J.F., and Brinks, E. 1995, MNRAS, **272**, 355
- Mushotzky, R.F., Holt, S.S., Smith, S.A., and 1981, ApJ, **244**, L47
- Nakai, N., Inoue, M., and Miyoshi, M. 1993, Nature, **361**, 45
- Nakai, N., Inoue, M., Miyazawa, K., Miyoshi, M., and Hall, P. 1995, PASJ, **47**, 771
- Nakai, N. 1995, in Proceeding of the 1st RESCEU International of Symposium on ” the Cosmological Constant and the Evolution of the Universe ”, eds. by K. Sato, T. Sugimotohara, and N. Sugiyama, (Tokyo: Universal Academy Press, Inc.), 113.
- Nakai, N., Miyoshi, M., Hagiwara, Y., Inoue, M. 1998, submitted to PASJ
- Nakai, N., Inoue, M., Hagiwara, Y., Miyoshi, M., and P.J.Diamond. 1998, In *Radio Emission from Galactic and Extragalactic Compact Sources, IAU Colloquium 164*, eds. by J.A.Zensus, G.B.Taylor and J.M.Wrobel, San Francisco: ASP, 237
- Norgaard-Nielsen, H.U., and Goudfrooij, P., Jorgensen, H.E., and Hansen, L. 1993, A&A, **279**, 61
- Norman, C., and Scoville, N. 1988, ApJ, **332**, 124

- Okumura, S.K. 1998, In *Proceedings of the International Symposium on 'Supercomputing'*, ed. by T. Ebisuzaki, Kluwer Academic Publishers, Dordrecht.
- Osterbrock, D.E. 1978 *Proc. of Natl. Acad. Sci. USA*, 1978, **75**, 540
- Osterbrock, D.E. 1977, *ApJ*, **215**, 733
- Padovani, P., Urry, C.M. 1990, *ApJ*, **356**, 75
- Palumbo, G.G.C., Tanzella - Nitti, G., Vettolani, G. 1983, *Catalogue of Radial Velocities of Galaxies*, Gordon and Breach Science Publishers, (New York)
- Pedlar, A., Boller, R.V., and Davies, R.D. 1983, *MNRAS*, **203**, 667
- Pedlar, A., Meaburn, J., Axon, D.J., Unger, S.W., Whittle, M., Meurs, E.J.A., Guernine, N. and Ward, M. 1989, *MNRAS*, **238**, 863
- Pedlar, A., Ghataure, H.S., Davies, R.D., Harrison, B.A., Perley, R., Crane, P.C., and Unger, S.W. 1990, *MNRAS*, **246**, 477
- Pedlar, A., Howley, P., Axon, D.J., and Unger, S.W. 1992, *MNRAS*, **259**, 369
- Pedlar, A., Kukula, M.J. 1994, *Proc. of IAU symposium 159*, 1994, 430
- Phillips, T.G. and Woody, D.P. 1982, *ARA&A*, **20**, 285
- Pihlström Y. M., et al., in press.
- Planesas, P., Scoville, N., Myers, S.T. 1991, *ApJ*, **369**, 364
- Reuter, H.-P., Pohl, M., Lesch, H., and Sievers, A.W. 1993, *A&A*, **277**, 21
- Richer, H.B., Crabtree, D.R., Fabian, A.C., and Lin, D.N.C. 1993, *AJ*, **105**, 877
- Romney, J.D. Ph.D Thesis 1979, California Institute of Technology.
- Roth, J. 1994, *AJ*, **108**, 862
- Rydbeck, G., Wiklund, T., Cameron, M., Wild, W., Eckart, A., Gensel, R., and Rothermel, H. 1993, *A&A*, **270**, L13
- Sakamoto, K. Ph.D Thesis 1996, Tokyo University.
- Sanders, D., Soifer, B., Elias, J., Madore, B., Matthews, K., Neugebauer, D., and Scoville, N. 1988, *ApJ*, **325**, 74
- Satoh, S., Inoue, M., Nakai, N., Shibata, K., Kamenno, S., Migenes, V. 1998, in *Radio Emission from Galactic and Extragalactic Compact Sources*, I.A.U. Colloquium 164, eds. G.B. Taylor, J.M. Wrobel, J.A. Zensus, (San Francisco: ASP), 219.
- Scoville, N.Z., Matthews, K., Carico, D.P., and Sanders, D.B. 1988, *ApJ*, **327**, 61
- Scoville, N., Soifer, B. 1988, *ApJ*, **325**, 74
- Seyfert, C. 1943, *ApJ*, **97**, 28

- Shlosman, I., Frank, J., and Begelman, M.C. 1989, *Nature*, **338**, 45
- Soifer B.T., Sanders D.B., Madore B.F., Neugebauer G.E., Danielson G.E., Elias J.H., Lonsdale C.J., and Rice, W.L. 1987, *ApJ*, **320**, 238
- Tacconi, L.J., Genzel, R., Blietz, M., Cameron, M., Harris, A.I., and Madden, S. 1994, *ApJ*, **426**, L77
- Tacconi, L.J., Gallimore, J.F., Genzel, R., Schinnerer, E., and Downs, D. 1997, *Ap&SS*, **248**, 59
- Tadhunter, C.N. and Tsvetanov, Z. 1989, *Nature*, **341**, 422
- Toomre, A. and Toomre, J. 1972, *ApJ*, **178**, 623
- Trotter, A.S., Greenhill, L.J., Moran, J.M., Reid, M.J., Irwin, J.A., Lo, K-Y. 1998, *ApJ*, **495**, 740
- Ulvestad, J.S., Neff, S.G., and Willson, A.S. 1986, *AJ*, **93**, 22
- Unger, S.W., Pedlar, A., Axon, D.J., Whittle, M., Meurs, E.J.A., and Ward, M.J. 1987, *MNRAS*, **228**, 671
- Unger, S.W., Lewis, J.R., Pedlar, A., and Axon, D.J. 1992, *MNRAS*, **258**, 371
- Urry, C.M., Padovani, P. and Stickel, M. 1991, *ApJ*, **382**, 501
- Urry, C.M., and Padovani, P. 1995, *PASP*, **107**, 803
- van Gorkom, J.H., and Ekers, R.D. 1983, *ApJ*, **267**, 528
- van Gorkom, J.H., Knapp, G.R., Raimond, E., Faber, S.M., and Gallagher, J.S. 1986, *AJ*, **91**, 791
- van Langevelde, H.J., van Dishoeck, E.F., Sevenster, M.N., and Israel, F.P. 1995, *ApJ*, **448**, L123
- Watson, W.D., and Wallin B.K. 1994, *ApJ*, **432**, L35
- White, D.A., Fabian, A.C., Johnstone, R.M., 1991, *MNRAS*, **252**, 72
- White, R.L., and Becker, R.H. 1992, *ApJS*, **79**, 331
- Whiteoak, J.B., Gardner, F.F. 1987, *Proc. Astro. Soc. Aust.*, **7**, (1)
- Wiklind, T., and Combes, F. 1996, *A&A*, **315**, 86
- Wilson, A.S., and Heckman, T.M. 1985, in *Astrophysics of Active galaxies and Quasi-stellar Objects*, ed. Miller, R.H., Oxford Univ. press, 96
- Wilson, A.S., and Colbert, E.J.M. 1995, *ApJ*, **438**, 62
- Wilson, A.S. 1997, In the proceedings of '*Accretion Processes in Astrophysical Systems: Some Like it Hot*', in press
- Wink, J.E., Guilleaume, S., and Wilson, T.L. 1997, *A&A*, **322**, 427
- Young, J.S., Claussen, M.J., and Scoville, N.Z. 1988, *ApJ*, **324**, 115
- Young, J.S., and Devereux, N.A. 1991, *ApJ*, **373**, 414

Appendix. Parameters in the Optics

X --- Relative distance from the sub-reflector of the 45m telescope
to feed horns, measured from the beam waist of the 45m optics.
W --- Beam radius at 1/e value
B --- Beam radius at - 30 dB level
R --- Beam curvature

All lengths in mm.

Parameters at 3 mm

NUMBER OF LENSES= 6
LENS= 1 FL= 6296.000 XL= 0.000
LENS= 2 FL= 6296.000 XL= 17000.000
LENS= 3 FL= 1633.000 XL= 24800.000
LENS= 4 FL= 1633.000 XL= 27200.000
LENS= 5 FL= 209.460 XL= 29400.000
LENS= 6 FL= 81.050 XL= 29928.000
FREQUENCY= 100.000 GHz WAVELENGTH= 2.998 mm
EDGE-LEVEL= - 30.00 dB B/W= 1.858
REFRACTIVE INDEX= 1.0
START FROM A SPHERICAL WAVEFRONT
XST= -26812.000 WS= 1477.000 RS= -20489.000

BEAM-WAISTS

WAIST= 0	X= -6324.646	W= 13.237	B= 24.600
WAIST= 1	X= 39175.305	W= 448.456	B= 833.438
WAIST= 2	X= 23271.047	W= 13.277	B= 24.674
WAIST= 3	X= 20259.713	W= 102.265	B= 190.056
WAIST= 4	X= 28928.449	W= 13.714	B= 25.488
WAIST= 5	X= 29716.387	W= 8.760	B= 16.280
WAIST= 6	X= 30045.527	W= 4.630	B= 8.605

BEAM AT LENSES

LENS= 1	W= 456.138	B= 847.715
RI=	6329.977	RO= -1172967.500
LENS= 2	W= 450.932	B= 838.039
RI=	-2025153.250	RO= -6276.487
LENS= 3	W= 110.694	B= 205.720

RI= 1551.269 R0= 30994.537
LENS= 4 W= 121.046 B= 224.960
RI= 24246.471 R0= -1750.925
LENS= 5 W= 35.562 B= 66.090
RI= 553.935 R0= -336.823
LENS= 6 W= 24.661 B= 45.831
RI= 242.169 R0= -121.822

X	W	B	R	
-26812.0000	1477.000	2744.947	-20489.0000	----
-26810.0000	1476.856	2744.679	-20487.0000	Sub-reflector
29386.0000	34.665	64.424	542.4562	
29388.0000	34.793	64.661	544.0867	
29390.0000	34.921	64.899	545.7204	
29392.0000	35.049	65.137	547.3572	
29394.0000	35.177	65.375	548.9972	
29396.0000	35.305	65.613	550.6403	
29398.0000	35.433	65.852	552.2864	
29400.0000	35.562	66.090	553.9354	----
29402.0000	35.351	65.698	-334.9539	Mirror #2
29404.0000	35.140	65.306	-333.0855	
29406.0000	34.929	64.914	-331.2189	
29408.0000	34.718	64.522	-329.3540	
29410.0000	34.507	64.130	-327.4909	
29412.0000	34.296	63.739	-325.6295	
29630.0000	12.857	23.894	-161.2366	
29632.0000	12.698	23.599	-161.0106	
29634.0000	12.541	23.307	-160.8707	
29636.0000	12.386	23.019	-160.8233	
29638.0000	12.233	22.735	-160.8756	
29640.0000	12.082	22.454	-161.0354	
29642.0000	11.933	22.177	-161.3113	
29644.0000	11.786	21.904	-161.7130	----
29646.0000	11.642	21.635	-162.2511	Mirror #3
29648.0000	11.499	21.371	-162.9378	
29650.0000	11.359	21.111	-163.7862	
29652.0000	11.222	20.855	-164.8117	
29654.0000	11.087	20.605	-166.0311	
29656.0000	10.955	20.359	-167.4638	
29658.0000	10.825	20.119	-169.1317	
29660.0000	10.699	19.883	-171.0597	

29690.0000	9.219	17.134	-271.4356
29692.0000	9.154	17.012	-289.5324
29694.0000	9.093	16.899	-311.2202
29696.0000	9.037	16.795	-337.5557
29698.0000	8.986	16.700	-370.0555
29700.0000	8.940	16.614	-410.9767
29702.0000	8.899	16.538	-463.8315
29704.0000	8.863	16.472	-534.4003
29706.0000	8.833	16.415	-632.9158
29708.0000	8.807	16.368	-779.3718
29710.0000	8.787	16.331	-1018.8057
29712.0000	8.773	16.304	-1478.3893
29714.0000	8.764	16.287	*****
29716.0000	8.760	16.280	*****
29718.0000	8.762	16.283	*****
29720.0000	8.769	16.296	1793.1321
29722.0000	8.781	16.319	1157.5304
29724.0000	8.799	16.353	856.9231
29726.0000	8.822	16.396	682.2280
29728.0000	8.851	16.449	568.3926
29730.0000	8.884	16.511	488.5932
29732.0000	8.923	16.584	429.7501
29734.0000	8.967	16.666	384.7246
29736.0000	9.017	16.757	349.2896
29738.0000	9.071	16.858	320.7828
29740.0000	9.130	16.967	297.4438
29742.0000	9.193	17.086	278.0618
29744.0000	9.262	17.213	261.7773
29746.0000	9.335	17.349	247.9624
29748.0000	9.412	17.493	236.1487
29750.0000	9.494	17.645	225.9788
29810.0000	13.444	24.984	162.6851
29812.0000	13.610	25.293	163.2402
29814.0000	13.777	25.604	163.8546
29816.0000	13.946	25.918	164.5247
29818.0000	14.116	26.234	165.2470
29820.0000	14.288	26.553	166.0188
29822.0000	14.460	26.874	166.8370
29824.0000	14.634	27.197	167.6991
29826.0000	14.809	27.523	168.6028
29828.0000	14.986	27.850	169.5458
29830.0000	15.163	28.180	170.5260
29832.0000	15.341	28.511	171.5414
29834.0000	15.521	28.845	172.5904

---- Wire grid

29836.0000	15.701	29.180	173.6711
29838.0000	15.882	29.517	174.7821
29840.0000	16.064	29.855	175.9219
29842.0000	16.248	30.195	177.0890
29844.0000	16.431	30.537	178.2823
29846.0000	16.616	30.881	179.5004
29848.0000	16.802	31.225	180.7423
29850.0000	16.988	31.572	182.0069
29852.0000	17.175	31.919	183.2932
29854.0000	17.363	32.268	184.6003
29856.0000	17.551	32.618	185.9272
29858.0000	17.740	32.970	187.2731
29860.0000	17.930	33.323	188.6372
29862.0000	18.121	33.676	190.0188
29864.0000	18.312	34.031	191.4172
29866.0000	18.503	34.388	192.8316
29868.0000	18.695	34.745	194.2615
29870.0000	18.888	35.103	195.7062

---- Mirror #5

29920.0000	23.848	44.321	235.3697
29922.0000	24.051	44.697	237.0608
29924.0000	24.254	45.075	238.7579
29926.0000	24.457	45.453	240.4607
29928.0000	24.661	45.831	242.1692
29930.0000	24.256	45.079	-119.8961
29932.0000	23.851	44.327	-117.9730
29934.0000	23.447	43.576	-116.0528
29936.0000	23.043	42.825	-114.1354
29938.0000	22.640	42.075	-112.2211

---- Teflon lens

30000.0000	10.463	19.446	-56.6132
30002.0000	10.095	18.762	-55.1226
30004.0000	9.731	18.084	-53.6810
30006.0000	9.370	17.414	-52.2960
30008.0000	9.014	16.753	-50.9765
30010.0000	8.663	16.100	-49.7336
30012.0000	8.318	15.458	-48.5810
30014.0000	7.979	14.828	-47.5360
30016.0000	7.647	14.211	-46.6203
30018.0000	7.323	13.609	-45.8622
30020.0000	7.008	13.025	-45.2987
30022.0000	6.705	12.460	-44.9794
30024.0000	6.413	11.918	-44.9724
30026.0000	6.135	11.401	-45.3736
30028.0000	5.873	10.914	-46.3229

30030.0000	5.628	10.460	-48.0319	
30032.0000	5.405	10.044	-50.8377	
30034.0000	5.204	9.672	-55.3110	
30036.0000	5.029	9.347	-62.5022	
30038.0000	4.883	9.075	-74.5775	---- feed horn

Parameters at 2 mm

NUMBER OF LENSES= 6

LENS= 1	FL=	6296.000	XL=	0.000
LENS= 2	FL=	6296.000	XL=	17000.000
LENS= 3	FL=	1633.000	XL=	24800.000
LENS= 4	FL=	1633.000	XL=	27200.000
LENS= 5	FL=	209.460	XL=	29400.000
LENS= 6	FL=	69.650	XL=	29928.000

FREQUENCY= 150.000 GHz WAVELENGTH= 1.999 mm

EDGE-LEVEL= - 30.00 dB B/W= 1.858

REFRACTIVE INDEX= 1.0

START FROM A SPHERICAL WAVEFRONT

XST= -26812.000 WS= 1477.000 RS= -20489.000

BEAM-WAISTS

WAIST= 0	X=	-6323.730	W=	8.825	B=	16.401
WAIST= 1	X=	76066.961	W=	442.656	B=	822.658
WAIST= 2	X=	23269.867	W=	8.851	B=	16.450
WAIST= 3	X=	15779.238	W=	90.079	B=	167.408
WAIST= 4	X=	28933.979	W=	9.149	B=	17.004
WAIST= 5	X=	29744.852	W=	6.646	B=	12.352
WAIST= 6	X=	30028.750	W=	3.479	B=	6.466

BEAM AT LENSES

LENS= 1	W=	455.955	B=	847.375
RI=	6326.101	R0=	-1323207.875	
LENS= 2	W=	450.722	B=	837.649
RI=	-1665146.125	R0=	-6272.285	
LENS= 3	W=	110.331	B=	205.046
RI=	1540.045	R0=	27054.869	
LENS= 4	W=	120.913	B=	224.712
RI=	25665.123	R0=	-1743.964	
LENS= 5	W=	33.670	B=	62.575
RI=	503.177	R0=	-358.834	
LENS= 6	W=	18.748	B=	34.842

30030.0000	5.628	10.460	-48.0319	
30032.0000	5.405	10.044	-50.8377	
30034.0000	5.204	9.672	-55.3110	
30036.0000	5.029	9.347	-62.5022	
30038.0000	4.883	9.075	-74.5775	---- feed horn

Parameters at 2 mm

NUMBER OF LENSES= 6

LENS= 1	FL=	6296.000	XL=	0.000
LENS= 2	FL=	6296.000	XL=	17000.000
LENS= 3	FL=	1633.000	XL=	24800.000
LENS= 4	FL=	1633.000	XL=	27200.000
LENS= 5	FL=	209.460	XL=	29400.000
LENS= 6	FL=	69.650	XL=	29928.000

FREQUENCY= 150.000 GHz WAVELENGTH= 1.999 mm

EDGE-LEVEL= - 30.00 dB B/W= 1.858

REFRACTIVE INDEX= 1.0

START FROM A SPHERICAL WAVEFRONT

XST= -26812.000 WS= 1477.000 RS= -20489.000

BEAM-WAISTS

WAIST= 0	X=	-6323.730	W=	8.825	B=	16.401
WAIST= 1	X=	76066.961	W=	442.656	B=	822.658
WAIST= 2	X=	23269.867	W=	8.851	B=	16.450
WAIST= 3	X=	15779.238	W=	90.079	B=	167.408
WAIST= 4	X=	28933.979	W=	9.149	B=	17.004
WAIST= 5	X=	29744.852	W=	6.646	B=	12.352
WAIST= 6	X=	30028.750	W=	3.479	B=	6.466

BEAM AT LENSES

LENS= 1	W=	455.955	B=	847.375
RI=	6326.101	R0=	-1323207.875	
LENS= 2	W=	450.722	B=	837.649
RI=	-1665146.125	R0=	-6272.285	
LENS= 3	W=	110.331	B=	205.046
RI=	1540.045	R0=	27054.869	
LENS= 4	W=	120.913	B=	224.712
RI=	25665.123	R0=	-1743.964	
LENS= 5	W=	33.670	B=	62.575
RI=	503.177	R0=	-358.834	
LENS= 6	W=	18.748	B=	34.842

RI= 209.476 R0= -104.344

X	W	B	R	
-26812.0000	1477.000	2744.947	-20489.0000	---- Sub-reflector
-26810.0000	1476.856	2744.679	-20487.0020	
-26808.0000	1476.712	2744.411	-20485.0020	
-26806.0000	1476.568	2744.144	-20483.0020	
-26804.0000	1476.423	2743.875	-20481.0020	
29400.0000	33.670	62.575	503.1765	---- Mirror #2
29402.0000	33.483	62.226	-356.9157	
29404.0000	33.295	61.877	-354.9982	
29406.0000	33.107	61.529	-353.0817	
29408.0000	32.920	61.180	-351.1662	
24410.0000	32.732	60.832	-349.2517	
29590.0000	16.244	30.188	-185.9905	
29592.0000	16.069	29.864	-184.3980	
29594.0000	15.895	29.541	-182.8162	
29596.0000	15.721	29.218	-181.2457	
29598.0000	15.548	28.896	-179.6869	
29600.0000	15.375	28.575	-178.1402	
29602.0000	15.203	28.254	-176.6063	
29604.0000	15.031	27.935	-175.0856	
29606.0000	14.860	27.616	-173.5787	
29608.0000	14.689	27.298	-172.0862	
29640.0000	12.037	22.371	-150.8396	
29642.0000	11.878	22.075	-149.7339	
29644.0000	11.720	21.781	-148.6636	----- Mirror #3
29646.0000	11.563	21.489	-147.6309	
29648.0000	11.407	21.199	-146.6382	
29650.0000	11.252	20.911	-145.6880	
29652.0000	11.098	20.625	-144.7830	
29654.0000	10.945	20.341	-143.9262	
29656.0000	10.794	20.060	-143.1209	
29658.0000	10.643	19.780	-142.3706	
29660.0000	10.495	19.504	-141.6792	
29720.0000	7.059	13.119	-218.8803	
29722.0000	6.997	13.004	-233.8620	
29724.0000	6.940	12.897	-252.1013	
29726.0000	6.887	12.799	-274.6350	
29728.0000	6.839	12.711	-302.9922	

29730.0000	6.797	12.632	-339.5256
29732.0000	6.759	12.562	-388.0524
29734.0000	6.727	12.502	-455.2039
29736.0000	6.700	12.452	-553.6048
29738.0000	6.679	12.412	-710.6205
29740.0000	6.663	12.382	-998.7410
29742.0000	6.652	12.363	-1693.8253
29744.0000	6.647	12.353	*****
29746.0000	6.647	12.354	*****
29748.0000	6.653	12.365	1534.6755
29750.0000	6.665	12.386	941.7271
29752.0000	6.682	12.418	681.6899
29754.0000	6.704	12.459	536.2240
29756.0000	6.732	12.510	443.6680
29758.0000	6.765	12.572	379.8777
29760.0000	6.803	12.643	333.4597
29762.0000	6.846	12.723	298.3354
29764.0000	6.895	12.813	270.9662
29766.0000	6.948	12.912	249.1519
29768.0000	7.006	13.021	231.4526

29910.0000	17.148	31.868	194.3459
29912.0000	17.324	32.197	195.9966
29914.0000	17.501	32.526	197.6555
29916.0000	17.679	32.855	199.3223
29918.0000	17.856	33.185	200.9969
29920.0000	18.034	33.515	202.6789
29922.0000	18.212	33.846	204.3681
29924.0000	18.390	34.178	206.0642
29926.0000	18.569	34.510	207.7670
29928.0000	18.748	34.842	209.4764
29930.0000	18.389	34.174	-102.4164

---- Teflon lens

29960.0000	13.044	24.241	-74.0162
29962.0000	12.691	23.587	-72.1740
29964.0000	12.340	22.934	-70.3415
29966.0000	11.990	22.282	-68.5197
29968.0000	11.640	21.633	-66.7097
29970.0000	11.292	20.985	-64.9126

30000.0000	6.304	11.716	-41.3431
30002.0000	6.002	11.155	-40.2846
30004.0000	5.708	10.609	-39.3784
30006.0000	5.423	10.078	-38.6644
30008.0000	5.148	9.567	-38.1983
30010.0000	4.885	9.078	-38.0594

30012.0000	4.635	8.614	-38.3650	
30014.0000	4.402	8.181	-39.2959	
30016.0000	4.188	7.783	-41.1462	
30018.0000	3.996	7.427	-44.4292	---- feed horn

Parameters at 1.3 mm

NUMBER OF LENSES= 6

LENS= 1 FL=	6296.000	XL=	0.000
LENS= 2 FL=	6296.000	XL=	17000.000
LENS= 3 FL=	1633.000	XL=	24800.000
LENS= 4 FL=	1633.000	XL=	27200.000
LENS= 5 FL=	209.460	XL=	29400.000
LENS= 6 FL=	41.320	XL=	29858.000

FREQUENCY= 210.000 GHz WAVELENGTH= 1.428 mm

EDGE-LEVEL= - 30.00 dB B/W= 1.858

REFRACTIVE INDEX= 1.0

START FROM A SPHERICAL WAVEFRONT

XST= -26812.000 WS= 1181.600 RS= -20489.000

BEAM-WAISTS

WAIST= 0 X=	-6323.910	W=	7.879	B=	14.643
WAIST= 1 X=	63190.020	W=	355.751	B=	661.150
WAIST= 2 X=	23270.098	W=	7.903	B=	14.687
WAIST= 3 X=	17119.730	W=	75.113	B=	139.594
WAIST= 4 X=	28932.889	W=	8.168	B=	15.180
WAIST= 5 X=	29738.002	W=	5.769	B=	10.722
WAIST= 6 X=	29910.945	W=	2.218	B=	4.121

BEAM AT LENSES

LENS= 1 W=	364.793	B=	677.953
RI=	6326.861	RO=	-1290749.000
LENS= 2 W=	360.611	B=	670.181
RI=	-1725545.500	RO=	-6273.111
LENS= 3 W=	88.322	B=	164.143
RI=	1542.250	RO=	27752.080
LENS= 4 W=	96.751	B=	179.809
RI=	25373.209	RO=	-1745.328
LENS= 5 W=	27.240	B=	50.625
RI=	513.258	RO=	-353.876
LENS= 6 W=	11.073	B=	20.579
RI=	164.710	RO=	-55.157

30012.0000	4.635	8.614	-38.3650	
30014.0000	4.402	8.181	-39.2959	
30016.0000	4.188	7.783	-41.1462	
30018.0000	3.996	7.427	-44.4292	---- feed horn

Parameters at 1.3 mm

NUMBER OF LENSES= 6

LENS= 1 FL=	6296.000	XL=	0.000
LENS= 2 FL=	6296.000	XL=	17000.000
LENS= 3 FL=	1633.000	XL=	24800.000
LENS= 4 FL=	1633.000	XL=	27200.000
LENS= 5 FL=	209.460	XL=	29400.000
LENS= 6 FL=	41.320	XL=	29858.000

FREQUENCY= 210.000 GHz WAVELENGTH= 1.428 mm

EDGE-LEVEL= - 30.00 dB B/W= 1.858

REFRACTIVE INDEX= 1.0

START FROM A SPHERICAL WAVEFRONT

XST= -26812.000 WS= 1181.600 RS= -20489.000

BEAM-WAISTS

WAIST= 0 X=	-6323.910	W=	7.879	B=	14.643
WAIST= 1 X=	63190.020	W=	355.751	B=	661.150
WAIST= 2 X=	23270.098	W=	7.903	B=	14.687
WAIST= 3 X=	17119.730	W=	75.113	B=	139.594
WAIST= 4 X=	28932.889	W=	8.168	B=	15.180
WAIST= 5 X=	29738.002	W=	5.769	B=	10.722
WAIST= 6 X=	29910.945	W=	2.218	B=	4.121

BEAM AT LENSES

LENS= 1 W=	364.793	B=	677.953
RI=	6326.861	RO=	-1290749.000
LENS= 2 W=	360.611	B=	670.181
RI=	-1725545.500	RO=	-6273.111
LENS= 3 W=	88.322	B=	164.143
RI=	1542.250	RO=	27752.080
LENS= 4 W=	96.751	B=	179.809
RI=	25373.209	RO=	-1745.328
LENS= 5 W=	27.240	B=	50.625
RI=	513.258	RO=	-353.876
LENS= 6 W=	11.073	B=	20.579
RI=	164.710	RO=	-55.157

X	W	B	R	
-26812.0000	1181.600	2195.958	-20489.0000	---- Sub-reflector
-26811.0000	1181.542	2195.851	-20488.0000	
-26810.0000	1181.485	2195.743	-20487.0000	
-26809.0000	1181.427	2195.637	-20486.0000	
-26808.0000	1181.370	2195.529	-20485.0000	
-26807.0000	1181.312	2195.422	-20484.0000	
-26806.0000	1181.254	2195.315	-20483.0000	
-26805.0000	1181.196	2195.208	-20482.0000	
29400.0000	27.240	50.625	513.2583	---- Mirror #2
29401.0000	27.163	50.482	-352.9227	
29402.0000	27.086	50.339	-351.9701	
29403.0000	27.009	50.196	-351.0177	
29404.0000	26.932	50.053	-350.0657	
29405.0000	26.855	49.910	-349.1139	
29406.0000	26.779	49.767	-348.1624	
29407.0000	26.702	49.624	-347.2113	
29408.0000	26.625	49.481	-346.2604	
29409.0000	26.548	49.338	-345.3098	
29410.0000	26.471	49.195	-344.3595	
29411.0000	26.394	49.052	-343.4095	
29412.0000	26.317	48.910	-342.4599	
29413.0000	26.240	48.767	-341.5105	
29414.0000	26.164	48.624	-340.5615	
29415.0000	26.087	48.481	-339.6127	
29416.0000	26.010	48.338	-338.6643	
29417.0000	25.933	48.196	-337.7162	
29418.0000	25.856	48.053	-336.7685	
29419.0000	25.780	47.910	-335.8210	
29420.0000	25.703	47.768	-334.8739	
29421.0000	25.626	47.625	-333.9272	
29641.0000	9.574	17.793	-152.3134	
29642.0000	9.511	17.676	-151.8895	
29643.0000	9.449	17.560	-151.4778	
29644.0000	9.386	17.444	-151.0786	---- Wire grid
29645.0000	9.324	17.329	-150.6923	
29646.0000	9.263	17.214	-150.3194	
29647.0000	9.201	17.100	-149.9602	
29648.0000	9.140	16.986	-149.6153	
29649.0000	9.079	16.873	-149.2851	
29650.0000	9.018	16.760	-148.9701	
29651.0000	8.958	16.648	-148.6709	

29652.0000	8.898	16.536	-148.3879
29653.0000	8.838	16.425	-148.1219
29654.0000	8.778	16.314	-147.8733
29655.0000	8.719	16.204	-147.6428
29656.0000	8.660	16.095	-147.4311
29657.0000	8.602	15.986	-147.2388
29658.0000	8.543	15.878	-147.0668
29659.0000	8.486	15.770	-146.9156

29731.0000	5.796	10.771	-773.2616
29732.0000	5.789	10.758	-899.9301
29733.0000	5.783	10.747	-1077.6460
29734.0000	5.778	10.738	-1344.6761
29735.0000	5.774	10.731	-1790.2766
29736.0000	5.771	10.726	*****
29737.0000	5.770	10.723	*****
29738.0000	5.769	10.722	*****
29739.0000	5.770	10.723	*****
29740.0000	5.771	10.726	*****
29741.0000	5.774	10.731	1792.6017
29742.0000	5.778	10.738	1345.9818
29743.0000	5.783	10.747	1078.4803
29744.0000	5.789	10.758	900.5085
29745.0000	5.796	10.771	773.6855
29746.0000	5.804	10.786	678.8262
29747.0000	5.813	10.803	605.2736
29748.0000	5.823	10.821	546.6343
29749.0000	5.834	10.842	498.8405
29750.0000	5.846	10.865	459.1804
29751.0000	5.859	10.890	425.7766
29752.0000	5.874	10.916	397.2883
29753.0000	5.889	10.944	372.7322
29754.0000	5.905	10.975	351.3712
29755.0000	5.923	11.007	332.6411
29756.0000	5.941	11.041	316.1035
29757.0000	5.960	11.077	301.4121
29758.0000	5.980	11.114	288.2900
29759.0000	6.002	11.154	276.5130

29850.0000	10.540	19.589	159.9035
29851.0000	10.606	19.712	160.4795
29852.0000	10.673	19.835	161.0630
29853.0000	10.739	19.958	161.6537
29854.0000	10.806	20.082	162.2515
29855.0000	10.872	20.206	162.8562

29856.0000	10.939	20.330	163.4676	
29857.0000	11.006	20.454	164.0855	
29858.0000	11.073	20.579	164.7097	---- Teflon lens
29859.0000	10.873	20.206	-54.2001	
29896.0000	3.781	7.027	-22.7823	
29897.0000	3.617	6.722	-22.3443	
29898.0000	3.457	6.426	-21.9931	
29899.0000	3.303	6.138	-21.7505	
29900.0000	3.154	5.862	-21.6464	
29901.0000	3.012	5.597	-21.7224	
29902.0000	2.877	5.347	-22.0389	
29903.0000	2.751	5.113	-22.6869	
29904.0000	2.635	4.897	-23.8094	
29905.0000	2.530	4.702	-25.6460	
29906.0000	2.438	4.531	-28.6297	
29907.0000	2.360	4.387	-33.6328	
29908.0000	2.298	4.271	-42.7124	---- feed horn

Parameters at 1.3 mm (half illumination mode)

NUMBER OF LENSES= 7

LENS= 1 FL=	65.000	XL=	0.000
LENS= 2 FL=	149.000	XL=	75.000
LENS= 3 FL=	209.460	XL=	458.000
LENS= 4 FL=	1633.000	XL=	2658.000
LENS= 5 FL=	1633.000	XL=	5058.000
LENS= 6 FL=	6296.000	XL=	12858.000
LENS= 7 FL=	6296.000	XL=	29858.000

FREQUENCY= 230.000 GHz WAVELENGTH= 1.303 mm

EDGE-LEVEL= - 30.00 dB B/W= 1.858

REFRACTIVE INDEX= 1.0

START FROM A SPHERICAL WAVEFRONT

XST=	-50.000	WS=	2.300	RS=	43.100
------	---------	-----	-------	-----	--------

BEAM-WAISTS

WAIST= 0 X=	-53.468	W=	2.206	B=	4.099
WAIST= 1 X=	-115.159	W=	8.718	B=	16.201
WAIST= 2 X=	249.927	W=	6.919	B=	12.858
WAIST= 3 X=	662.889	W=	12.560	B=	23.341
WAIST= 4 X=	7793.849	W=	39.063	B=	72.597
WAIST= 5 X=	6333.769	W=	11.170	B=	20.759

29856.0000	10.939	20.330	163.4676	
29857.0000	11.006	20.454	164.0855	
29858.0000	11.073	20.579	164.7097	---- Teflon lens
29859.0000	10.873	20.206	-54.2001	
29896.0000	3.781	7.027	-22.7823	
29897.0000	3.617	6.722	-22.3443	
29898.0000	3.457	6.426	-21.9931	
29899.0000	3.303	6.138	-21.7505	
29900.0000	3.154	5.862	-21.6464	
29901.0000	3.012	5.597	-21.7224	
29902.0000	2.877	5.347	-22.0389	
29903.0000	2.751	5.113	-22.6869	
29904.0000	2.635	4.897	-23.8094	
29905.0000	2.530	4.702	-25.6460	
29906.0000	2.438	4.531	-28.6297	
29907.0000	2.360	4.387	-33.6328	
29908.0000	2.298	4.271	-42.7124	---- feed horn

Parameters at 1.3 mm (half illumination mode)

NUMBER OF LENSES= 7

LENS= 1 FL=	65.000	XL=	0.000
LENS= 2 FL=	149.000	XL=	75.000
LENS= 3 FL=	209.460	XL=	458.000
LENS= 4 FL=	1633.000	XL=	2658.000
LENS= 5 FL=	1633.000	XL=	5058.000
LENS= 6 FL=	6296.000	XL=	12858.000
LENS= 7 FL=	6296.000	XL=	29858.000

FREQUENCY= 230.000 GHz WAVELENGTH= 1.303 mm

EDGE-LEVEL= - 30.00 dB B/W= 1.858

REFRACTIVE INDEX= 1.0

START FROM A SPHERICAL WAVEFRONT

XST= -50.000 WS= 2.300 RS= 43.100

BEAM-WAISTS

WAIST= 0 X=	-53.468	W=	2.206	B=	4.099
WAIST= 1 X=	-115.159	W=	8.718	B=	16.201
WAIST= 2 X=	249.927	W=	6.919	B=	12.858
WAIST= 3 X=	662.889	W=	12.560	B=	23.341
WAIST= 4 X=	7793.849	W=	39.063	B=	72.597
WAIST= 5 X=	6333.769	W=	11.170	B=	20.759

WAIST= 6 X= 82630.719 W= 186.283 B= 346.200
 WAIST= 7 X= 35930.676 W= 11.454 B= 21.287

BEAM AT LENSES

LENS= 1 W= 10.297 B= 19.137
 RI= 56.039 RO= 406.494
 LENS= 2 W= 12.566 B= 23.353
 RI= 366.589 RO= -251.032
 LENS= 3 W= 14.267 B= 26.515
 RI= 272.054 RO= -910.380
 LENS= 4 W= 67.093 B= 124.690
 RI= 2067.562 RO= -7769.506
 LENS= 5 W= 48.685 B= 90.480
 RI= -7679.858 RO= -1346.655
 LENS= 6 W= 242.592 B= 450.847
 RI= 6538.092 RO= -170033.734
 LENS= 7 W= 220.265 B= 409.353
 RI= -185331.438 RO= -6089.143

X	W	B	R	
-50.0000	2.300	4.274	43.1000	---- feed horn
-40.0000	3.359	6.243	23.6742	
-30.0000	4.935	9.172	29.3254	
-20.0000	6.671	12.398	37.5754	
-10.0000	8.469	15.740	46.6305	
0.0000	10.297	19.137	56.0391	---- Teflon lens
10.0000	10.558	19.622	393.2167	
20.0000	10.834	20.134	383.3839	
30.0000	11.123	20.672	376.2838	
40.0000	11.425	21.233	371.3878	
50.0000	11.738	21.815	368.2956	
60.0000	12.062	22.417	366.6983	
70.0000	12.396	23.037	366.3537	---- Teflon lens
80.0000	12.317	22.890	-248.2710	
90.0000	11.825	21.977	-243.1697	
100.0000	11.345	21.083	-238.7219	
110.0000	10.876	20.212	-235.0677	
120.0000	10.420	19.365	-232.3903	
130.0000	9.979	18.546	-230.9341	
140.0000	9.556	17.760	-231.0324	
150.0000	9.153	17.011	-233.1517	
160.0000	8.772	16.303	-237.9665	
170.0000	8.417	15.642	-246.4883	
180.0000	8.090	15.036	-260.3076	
190.0000	7.796	14.489	-282.0763	

200.0000	7.539	14.011	-316.5711
210.0000	7.321	13.607	-373.3540
220.0000	7.148	13.284	-474.7672
230.0000	7.021	13.049	-688.0014
240.0000	6.944	12.906	-1350.9857
250.0000	6.919	12.858	*****
260.0000	6.945	12.907	1331.7062
270.0000	7.023	13.052	683.2912
280.0000	7.150	13.288	472.7547
290.0000	7.324	13.612	372.2858
300.0000	7.542	14.017	315.9401
310.0000	7.800	14.497	281.6827
320.0000	8.095	15.044	260.0571
330.0000	8.422	15.652	246.3307
340.0000	8.778	16.313	237.8726
350.0000	9.159	17.021	233.1034
360.0000	9.562	17.771	231.0178
370.0000	9.986	18.558	230.9452
380.0000	10.426	19.377	232.4213
390.0000	10.882	20.224	235.1145
400.0000	11.352	21.096	238.7815
410.0000	11.833	21.990	243.2397
420.0000	12.324	22.904	248.3497
430.0000	12.825	23.834	254.0027
440.0000	13.333	24.780	260.1132
450.0000	13.850	25.739	266.6125
460.0000	14.236	26.457	-915.3348
470.0000	14.083	26.174	-942.2703
480.0000	13.937	25.902	-973.2449
490.0000	13.797	25.641	-1008.9595
500.0000	13.664	25.393	-1050.2869
510.0000	13.537	25.158	-1098.3286
520.0000	13.417	24.935	-1154.4946
530.0000	13.305	24.726	-1220.6183
540.0000	13.199	24.530	-1299.1311
550.0000	13.101	24.349	-1393.3252
560.0000	13.011	24.181	-1507.7732
2600.0000	65.212	121.194	2011.7308
2610.0000	65.536	121.797	2021.3475
2620.0000	65.861	122.400	2030.9683
2630.0000	66.185	123.002	2040.5929
2640.0000	66.509	123.605	2050.2212
2650.0000	66.834	124.208	2059.8533
2660.0000	67.076	124.658	-7768.5312

---- Mirror #2

2670.0000	66.990	124.498	-7763.6733	
56600.0000	748.779	1391.576	20674.1602	
56610.0000	749.141	1392.249	20684.1602	
56620.0000	749.503	1392.922	20694.1582	
56630.0000	749.865	1393.595	20704.1562	
56640.0000	750.228	1394.269	20714.1523	
56650.0000	750.590	1394.942	20724.1504	
56660.0000	750.952	1395.615	20734.1484	
56670.0000	751.314	1396.288	20744.1445	---- Sub-reflector